

SEPTEMBER 1977

LRP 131/77

NUMERICAL COMPUTATIONS OF THE IDEAL
MAGNETOHYDRODYNAMIC STABILITY OF
SMALL ASPECT RATION TOKAMAKS

Daniel Berger

Thesis presented to the Department of Physics

of

Ecole Polytechnique Federale de Lausanne

Centre de Recherches en Physique des Plasmas

ECOLE POLYTECHNIQUE FEDERALE DE LAUSANNE

CONTENTS

	page
I INTRODUCTION	3
II IDEAL MHD MODEL	8
1. Basic MHD Equations	8
2. Magnetostatic Axisymmetric Equilibria	9
3. MHD Stability - Normal Mode Analysis	13
3.1 Plasma Potential Energy	13
a) Coordinate System	13
b) Projection of the Displacement	15
c) Normalization	16
d) Fourier Analysis. Up-down Symmetry	17
3.2 Vacuum Potential Energy	17
3.3 Localized Stability Criterion	21
III NUMERICAL SCHEME. CODE STRUCTURE	23
1. Plasma Potential Energy Approximation	23
2. Vacuum Discretization	27
3. Equilibrium and Mapping	29
3.1 Numerical Equilibria	29
3.2 Solovév Equilibrium	32
4. Code Structure	35

IV	MHD SPECTRUM OF SMALL ASPECT RATIO TOKAMAK WITH "FLAT" CURRENT PROFILE	38
1.	Axisymmetric Modes ($n = 0$)	38
1.1	Wall Stabilization	41
1.2	X-point effects	42
2.	Rigid Boundary Modes ($n \neq 0$)	43
3.	Free Boundary Modes ($n \neq 0$)	50
3.1	External Kink	50
3.2	Unstable MHD Spectrum	54
3.3	Wall Stabilization of a Kink Mode	62
V	MHD STABILITY OF SMALL ASPECT RATIO EQUILIBRIUM WITH PEAKED CURRENT DISTRIBUTION	64
1.	Equilibrium	65
2.	Effect of Peaking the Current Distribution	66
2.1	Kink Limit	66
2.2	Internal Mode Limit	67
2.3	Ballooning Limit	72
3.	Influence of β_p on the Maximum Average $\bar{\beta}$	76
4.	Influence of the Elongation on the Maximum Average $\bar{\beta}$	78
5.	Optimization of $\bar{\beta}$	80
VI	CONCLUSION	83
	ACKNOWLEDGEMENTS	85
	REFERENCES	86
	APPENDIX : Table of Symbols	90

I INTRODUCTION

The knowledge of the ideal MHD spectrum is a prerequisite to a good understanding of the behaviour of actual experiments and to the design of new devices. Most of the effort is now devoted to the study of axisymmetric toroidal configurations, either Tokamaks or Belt Pinches. One of the main objectives of the present fusion program is to show the possibility of increasing the maximum $\bar{\beta}$ value, which is the ratio of the plasma pressure to the energy invested in the magnetic field. This quantity measures the efficiency of an electric power reactor based on this principle. Different methods have been proposed to reach this objective, such as additional heating, cold gas injection, decrease of the aspect ratio, elongation of the plasma cross section. The first two schemes work by increasing β_p , which is the ratio of the plasma pressure to the energy furnished to heat the plasma. The other two play on the optimization of the geometrical parameters.

In order to understand the MHD stability behaviour of a plasma, Mercier, J. Greene and J. Johnson {1,2}, as a first try, have obtained necessary stability criteria against localized modes in straight and toroidal geometry. Surface instabilities have been treated by considering non-circularity and toroidicity as perturbations {3}. These approaches are irrelevant to solve the problems linked with the maximisation of $\bar{\beta}$.

Considerable progress in the knowledge of MHD stability has been made by a numerical approach, made possible with the size of recent computers. The first successful codes were time evolutionary codes {4}. The linearized equations of motion are solved numerically by a finite difference scheme. This discretization does not respect the topology of

the magnetic surfaces and gives only information for the fastest external modes in high beta plasmas. The advantage of this method is the straightforward inclusion of non-ideal effects like resistivity or viscosity.

The second method, used here, is to minimize the potential energy associated with a perturbation of the plasma. This procedure gives the normal modes of the equilibrium and their eigenfrequency. The displacement is represented in a limited set of basis functions, following a Ritz-Galerkin method. The nature of the unstable modes makes this choice very sensitive. A first code "THALIA", based on a mixed finite element discretization {5}, has been written, to treat straight cylinder plasma. The understanding of a 1-D MHD spectrum {6,7} is a solid basis for the study of toroidal effects. For axisymmetric toroidal configurations, the equilibrium quantities are functions of two variables (radius and angle) so that the stability problem becomes two-dimensional (2-D). The Princeton group has developed a general 2-D code {8}. The discretization uses global functions in the azimuthal direction (Fourier analysis) and finite elements in the radial direction. This method has difficulties to compute ballooning modes which are localized in the poloidal direction. Also, the time required to determine an eigenvalue is rather large {9}. In the Lausanne approach an extension of the finite element method, the so called "hybrid finite element" {10} discretization, has been used. This method has been tested in straight, circular and elliptical cases {10} and shows good convergence properties. It is well adapted to the study of numerically produced equilibria and easy to implement. The time and cost for one case is lower than the other method. A general purpose 2-D code, ERATO {11}, has been written.

The first use of this program was the understanding of the MHD spectrum of a simple toroidal equilibrium. After a workshop at the 7th European

Conference on Controlled Fusion the Solovév equilibria {12} have been chosen as a test for all 2-D MHD stability codes. It is analytic and thus avoids the errors inherent to numerically determined equilibria. Also, a spectral code, specific for these equilibria, has been written {13}. In our study, a small aspect ratio of 3, close to the Joint European Tokamak device, has been used. Different problems have been investigated. The first is a study of the internal modes and their correlations with the Mercier criterion. In this case, the localized criterion is also sufficient for MHD stability. Ballooning modes at low- n have been pointed out. The destabilizing effect of ellipticity on the internal mode {14}, and the non-sensitivity of the kink to this effect, have been shown. A major point is the toroidal coupling between singular surfaces, inside or outside the plasma. This phenomenon strongly affects transport processes and Alfvén heating in a toroidal system.

The non-physical toroidal current profile of the Solovév equilibrium leads to a strong external kink which destroys the equilibrium in a micro-second time scale. Real Tokamak experiments exhibit very good stability properties with no destructive linear MHD instability. Moreover, measurement of the current density profile has shown a peaked shape. To understand the behaviour of a Tokamak, the influence of peaking the current distribution on the MHD stability is a crucial point. The safety factor at the plasma surface is controlled by MHD instabilities, therefore limiting the total current and the total $\bar{\beta}$. The effect of a peaked current distribution on the MHD stability has first been investigated in a cylindrical circular plasma {4}.

In small aspect ratio Tokamaks the coupling between modes leads to different stability limits, unknown before our study.

To understand the effect of peaking the current distribution, we have varied this factor in a series of equilibria characterized by a Gaussian current shape. The elongation of the plasma cross section E , the safety factor on axis q_0 and the poloidal beta β_p are kept fixed. The aspect ratio is chosen equal to 3. For large q_0 , the stability is given by the kink limitation. This mode disappears when q_s/q_0 reaches a minimum level. (q_s represents the safety factor at the plasma surface.) For q_0 in the vicinity of 1, new modes, namely ballooning modes, degrade the maximum $\bar{\beta}$ and fix the MHD limit. The same study has been done for elongations of 1 and 2, and different β_p .

The β_p variation is related to additional heating or cold gas injection. The results show that stability will force the current to decrease as β_p increases. For a given q_0 , $\bar{\beta}$ passes through a maximum value as β_p increases, thus limiting the effectiveness of auxiliary heating [15].

Our computation shows the effectiveness of changing the elongation to increase the maximum $\bar{\beta}$ available with stability. The kink limit is not affected by the elongation, in contrast to ballooning modes which are destabilized. Up to an elongation of 2, the increase in $\bar{\beta}$ is linear with E . The existence of an optimum of $\bar{\beta}$ with E remains open.

Our study has exhibited limitations in q_s , q_0 , $\bar{\beta}_p$ and E imposed by the MHD stability theory. The usefulness of "ERATO" for design [16] or for understanding experiments is demonstrated.

In chapter II, the basic MHD theory needed to build the ERATO code is presented. Chapter III describes the discretization scheme used to approximate the plasma and the vacuum energy contribution. A flow chart of the code is given. Chapter IV deals with the MHD spectrum of the Solovév equilibrium. In Chapter V the effect of peaking the current distribution is studied. The optimization of the maximum $\bar{\beta}$ permitted by stability is performed for different elongations and β_p .

The MHD stability fixes a forbidden range of parameters for an experimental Tokamak or an electric power reactor. The remaining functional phase can be limited by strong anomalous transport or different types of instability, like resistive modes {27}. To obtain an exact range of functional parameters, a more detailed study must be made. This is the next step for the future of the thermonuclear energy.

II IDEAL MHD MODEL

This chapter contains the basic analytical theory needed for the construction of a numerical spectral MHD code.

1. Basic MHD Equations

In the ideal MHD model the plasma is treated as an inviscid fluid with infinite conductivity and no thermal diffusion. We consider plasma phenomena with time scales smaller than characteristic diffusion time. This model is able to analyze macroscopic instabilities.

In a natural unit system [17] the ideal MHD equations can be written :

$$\frac{\partial \rho}{\partial t} + \underline{\nabla}(\rho \underline{v}) = 0 \quad (2.1) \text{ (continuity equation)}$$

$$\frac{\partial(\rho \underline{v})}{\partial t} + \underline{\nabla}(\rho \underline{v} \underline{v}) = \underline{j} \times \underline{B} - \underline{\nabla} p \quad (2.2) \text{ (Newton equations)}$$

$$\frac{\partial \underline{B}}{\partial t} = \underline{\nabla} \times (\underline{v} \times \underline{B}) \quad (2.3) \text{ (Maxwell + Ohm Law)}$$

$$\underline{\nabla} \cdot \underline{B} = 0 \quad (2.4) \quad \underline{j} = \underline{\nabla} \times \underline{B} \quad (2.5) \text{ (Maxwell equations)}$$

$$\frac{\partial}{\partial t} \left(\frac{p}{\rho^{\gamma-1}} \right) + \underline{\nabla} \left(\frac{p \underline{v}}{\rho^{\gamma-1}} \right) = 0 \quad (2.6) \text{ (Equation of state)}$$

The dependent variables are the density ρ , the velocity of the fluid \underline{v} , the current density \underline{j} , the magnetic field \underline{B} and the pressure p .

First our aim is to investigate MHD equilibria.

2. Magnetostatic Axisymmetric Equilibria

Magnetic confinement devices such as Tokamaks or Belt Pinches exhibit a toroidal topology of constant pressure surfaces. This geometry is represented in Fig. 2.1.

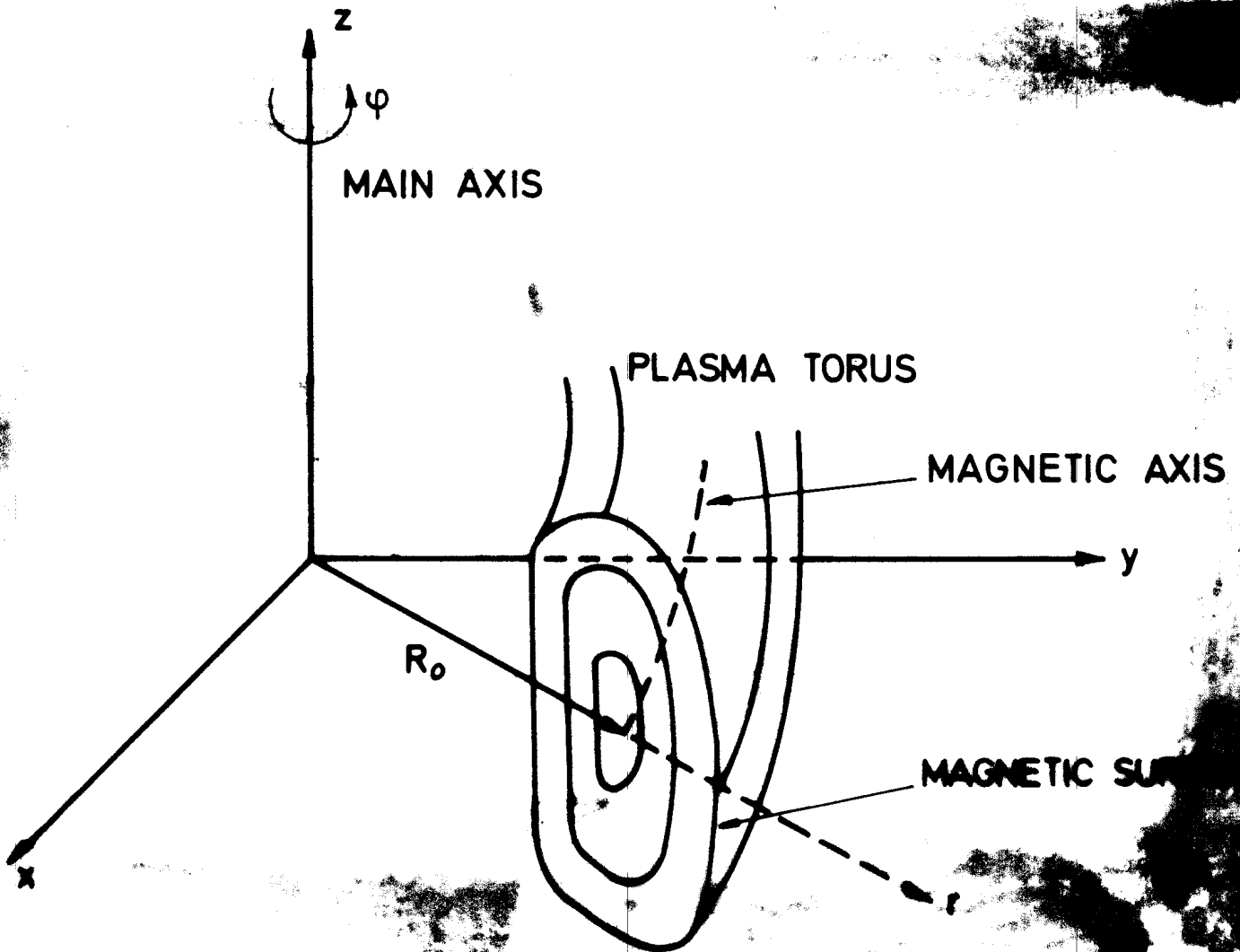


Figure 2.1

Toroidal geometry described by cylindrical coordinate system. Magnetic surfaces are plotted.

In a set of cylindrical coordinates (r, φ, z) axisymmetry eliminates any dependence on the toroidal direction φ .

The general solution of $\underline{\nabla} \cdot \underline{B} = 0$ can be written as

$$\underline{B} = T \frac{\underline{e}_\varphi}{r} + \frac{\underline{e}_\varphi}{r} \times \underline{\nabla} \Psi . \quad (2.7)$$

$\Psi(r, z)$ and T are two arbitrary functions, the flux of the poloidal field and the flux of the poloidal current respectively. Magnetic field lines lie in constant Ψ surfaces which are called magnetic surfaces.

Then {18}

$$\underline{j} = \underline{\nabla} \times \underline{B} = (\mathcal{L} \Psi) \frac{\underline{e}_\varphi}{r} - \frac{\underline{e}_\varphi}{r} \times \underline{\nabla} T \quad (2.8)$$

with

$$\mathcal{L} \equiv \frac{\partial^2}{\partial r^2} + \frac{\partial^2}{\partial z^2} - \frac{1}{r} \frac{\partial}{\partial r} .$$

The MHD equilibrium equation,

$$\underline{\nabla} p = \underline{j} \times \underline{B} , \quad (2.9)$$

implies that p and T are function of Ψ only. Getting (2.7), (2.8) and (2.9) together, we obtain the following partial differential equation for Ψ :

$$\mathcal{L} \Psi = -r^2 \frac{dp}{d\Psi} - T \frac{dT}{d\Psi} . \quad (2.10)$$

Note that the toroidal current density is

$$j_{\phi} = r \frac{dp}{d\psi} + \frac{1}{r} T \frac{dT}{d\psi} .$$

The two arbitrary functions $p(\psi)$ and $T(\psi)$ are determined by considerations linked with transport phenomena and the creation procedure of the plasma. These functions chosen, the problem is completely defined if we impose $\psi = \text{constant}$ on a given boundary surface. The choices used in our computation are specified in Chapter III and V.

2. MHD Stability. Normal Mode Analysis

The equation of motion for small displacement $\underline{\xi}(\underline{r}, t)$ of the plasma around its equilibrium position can be derived by finding the stationary points of the Lagrangian \mathcal{L} of the system.

For magnetostatic equilibria, we write

$$\underline{\xi}(\underline{r}, t) = \underline{\xi}(\underline{r}) e^{i\omega t}$$

and

$$\mathcal{L} = \omega^2 K_c(\underline{\xi}, \underline{\xi}^*) - W_p(\underline{\xi}, \underline{\xi}^*) - W_v(\underline{\xi}_s, \underline{\xi}_s^*) .$$

$\underline{\xi}_s$ are the values of $\underline{\xi}(\underline{r})$ at the plasma surface and $\omega^2 K_c$, W_p , W_v are the kinetic, plasma potential and vacuum energies, respectively.

Following Bernstein et al. [18,19] we obtain

$$\begin{aligned}
 K_c &= \frac{1}{2} \int_{\Omega_p} \rho |\underline{\xi}|^2 d\Omega_p \\
 W_p &= \frac{1}{2} \int_{\Omega_p} d\Omega_p \left\{ |\underline{Q} + (\underline{n} \cdot \underline{\xi})(\underline{j} \times \underline{n})|^2 + \right. \\
 &\quad \left. + \gamma \rho |\underline{\nabla} \underline{\xi}|^2 - 2(\underline{n} \cdot \underline{\xi})^2 (\underline{j} \times \underline{n}) \cdot (\underline{B} \cdot \underline{\nabla}) \cdot \underline{n} \right\}
 \end{aligned} \tag{2.11}$$

where $\underline{Q} = \underline{\nabla} \times (\underline{\xi} \times \underline{B})$ denotes the magnetic field perturbation in the plasma and γ the ratio of specific heats;

$$W_v = \frac{1}{2} \int_{\Omega_v} |\underline{\delta B}_v|^2 d\Omega_v \tag{2.12}$$

$\underline{\delta B}_v$ being the perturbed magnetic field in the vacuum region. The following boundary conditions {20} have to be fulfilled :

$$\underline{n} \times \underline{A} = - (\underline{n} \cdot \underline{\xi}) \underline{B} \quad (\text{at the plasma boundary}) \tag{2.13}$$

$$\underline{n} \times \underline{A} = 0 \quad (\text{at the wall limiting the vacuum region}) \tag{2.14}$$

Here \underline{n} denotes the unit vector normal to the plasma or wall surface, and \underline{A} is the vector potential from which \underline{B} is derived, with the gauge $\underline{\nabla} \cdot \underline{A} = 0$.

Solutions of this well-posed problem are called eigenmodes and the corresponding values ω^2 : eigenvalue. A negative ω^2 represents an unstable mode with a growth rate $\Gamma = \sqrt{|\omega^2|}$.

3. MHD Stability - Normal Mode Analysis

3.1 Plasma Potential Energy

a) Coordinate System

Considerable thought should be given to the choice of the coordinate system adapted for the calculation. The physical characteristics of the plasma equilibrium where currents can flow freely on magnetic surfaces, dictates the choice of Ψ as one coordinate. The second variable corresponds to the toroidal angle φ . The coordinate describing the poloidal direction is chosen, as a first try, as the orthogonal coordinate χ_{\perp} , perpendicular to the (Ψ, φ) variables.

In this curvilinear system the operator ∇ has the form

$$\nabla = r B_p \underline{e}_{\Psi} \frac{\partial}{\partial \Psi} + \frac{1}{r} \underline{e}_{\varphi} \frac{\partial}{\partial \varphi} + \frac{1}{J B_p} \underline{e}_{\chi_{\perp}} \frac{\partial}{\partial \chi_{\perp}}$$

J is the Jacobian of the system and B_p the poloidal magnetic field. The plasma potential energy W_p takes the form {1}

$$\begin{aligned} \delta W_p = & \frac{1}{2} \int_{\Omega_p} d\Psi d\varphi d\chi_{\perp} \left\{ \frac{1}{J r^2 B_p^2} \left| \frac{\partial X}{\partial \chi_{\perp}} + \frac{J T}{r^2} \frac{\partial X}{\partial \varphi} \right|^2 + \right. \\ & + \frac{r^2}{J} \left| \frac{\partial U}{\partial \chi_{\perp}} - T \frac{\partial}{\partial \Psi} \left(\frac{J X}{T^2} \right) \right|^2 + J B_p^2 \left| \frac{\partial U}{\partial \varphi} + \frac{\partial X}{\partial \Psi} + \frac{j_{\varphi}}{r B_p^2} X \right|^2 \\ & \left. + \gamma p \left| \frac{\partial}{\partial \Psi} (J X) + j_{\varphi} \frac{\partial U}{\partial \varphi} + \frac{\partial Z}{\partial \chi_{\perp}} + \frac{J T}{r^2} \frac{\partial Z}{\partial \chi_{\perp}} \right|^2 - 2 J K |X|^2 \right\} \quad (2.15) \end{aligned}$$

with

$$X = r B_p \xi_{\Psi}, \quad Y = \frac{\xi_{\varphi}}{r}, \quad Z = \frac{\xi_{\chi_{\perp}}}{B_p}, \quad U = \frac{\xi_{\varphi}}{r} - \frac{T}{r^2} Z$$

and

$$K = \frac{j_{\varphi}^2}{r^2 B_p^2} + \frac{j_{\varphi}}{r B_p} \frac{\partial B_p}{\partial \Psi} + T \frac{dT}{d\Psi} \Psi \frac{1}{r^3} \left(\frac{\partial r}{\partial \Psi} \right)_n.$$

This system has been used in a first version of ERATO {21} using a pure finite element discretization. For an elongated plasma cross section the orthogonal coordinate system has an anomalous behaviour near the magnetic axis where the χ_{\perp} -lines collapse in the direction of elongation. Moreover, the analytical stability criterion {1,2} or a continuum spectral analysis {22} shows the fundamental importance of the operator $\underline{B} \cdot \underline{\nabla}$, especially for internal modes. It appears in the first term of W_p in Eq. (2.15). It is possible by a change of variable to make this operator constant on each magnetic surface and to represent it easily {8}. Let us define

$$d\chi = \frac{\mathcal{I}T}{r^2 q} d\chi_{\perp} \quad , \quad d\Omega_p = \frac{qr^2}{T} d\Psi d\varphi d\chi. \quad (2.16)$$

$q(\Psi)$ is a normalizing factor such that $0 \leq \chi \leq 2\pi$. So

$$q(\Psi) = \frac{1}{2\pi} \oint dl \frac{T}{r^2 B_p}$$

and corresponds to the usual safety factor.

We transform the partial derivative with respect to Ψ at constant χ_{\perp} to a derivative at constant χ by the relation

$$\left. \frac{d}{d\Psi} (\mathcal{I}S) \right|_{\chi_{\perp}} = \frac{T}{r^2 q S} \left\{ \frac{\partial}{\partial \Psi} \left(\frac{qr^2 S}{T} \right)_{\chi} + \frac{\partial}{\partial \chi} \left(\frac{qr^2 \mathcal{I}S}{T} \right) \right\}. \quad (2.17)$$

$\mathcal{V}(\Psi, \chi) = \left. \frac{\partial \chi}{\partial \Psi} \right|_{\chi_{\perp}}$ measures the non-orthogonality of the system and $S(\Psi, \chi)$ is a general function. Putting (2.17) into (2.15), we obtain a new W_p form with a natural variable $V = q\sqrt{\chi} - U$. As χ is proportional to $\Psi^{\frac{1}{2}}$ around the axis, we choose the coordinate system $(\Psi^{\frac{1}{2}}, \varphi, \chi)$ {11} with the corresponding plasma energy

$$\begin{aligned}
 W_p = \int_{\Omega_p} \frac{d\sqrt{\Psi}}{\sqrt{\Psi}} d\varphi d\chi \left\{ \frac{4T^3\Psi}{qr^4B_p^2} |F(\bar{X})|^2 + \frac{T^3}{q} \left| \frac{\partial \bar{X}}{\partial \sqrt{\Psi}} + \frac{\partial \bar{V}}{\partial \chi} \right|^2 \right. \\
 + \frac{qr^2B_p^2}{T\Psi} \left| \sqrt{\Psi} \frac{\partial}{\partial \sqrt{\Psi}} \left(\frac{T\bar{X}}{q} \right) + 2vTF(\bar{X}) + \frac{2\Psi j_\varphi T\bar{X}}{qrB_p^2} + \sqrt{\Psi} T \frac{\partial \bar{V}}{\partial \varphi} \right|^2 \\
 \left. + \frac{\mu_p T}{qr^2} \left| \frac{\partial}{\partial \varphi} (r^2\bar{X}) + \frac{\partial}{\partial \chi} (r^2\bar{V}) + qF(r^2\bar{Y}) \right|^2 - \frac{8r^2T}{q} K|\bar{X}|^2 \right\}
 \end{aligned}$$

where

$$\begin{aligned}
 \bar{X} = \frac{qrB_p}{T} \xi_\psi, \quad \bar{Y} = \frac{2\sqrt{\Psi} \xi_\varphi}{rT}, \quad \bar{V} = 2vT\sqrt{\Psi}\bar{X} - \bar{Y} + \frac{2\sqrt{\Psi} \xi_x}{r^2B_p} \\
 F = \frac{1}{q} \frac{\partial}{\partial \chi} - \frac{\partial}{\partial \varphi} \tag{2.18}
 \end{aligned}$$

b) Projection of the displacement

The variables \bar{X} , \bar{Y} , \bar{V} are well defined for a numerical approach. For example, there are no singularities when the toroidal current decreases (low- β) or around the magnetic axis.

This transformation can be written in the matrix form

$$\begin{pmatrix} \xi_\psi \\ \xi_\varphi \\ \xi_{x_\perp} \end{pmatrix} = \begin{pmatrix} \frac{T}{qrB_p} & 0 & 0 \\ 0 & \frac{Tr}{q\sqrt{\Psi}\Psi_s} & 0 \\ vr^2B_p & \frac{r^3B_p}{q\sqrt{\Psi}\Psi_s} & \frac{r^2B_p}{2\sqrt{\Psi}\Psi_s} \end{pmatrix} \begin{pmatrix} \bar{X} \\ \bar{Y} \\ \bar{V} \end{pmatrix} \tag{2.19}$$

A remarkable property is that the 2nd and 3rd basis vectors are proportional to the magnetic field \underline{B} and tangent to the magnetic surface, respectively. We have basis projection vectors where acoustic and shear Alfvén modes are decoupled. This fact is important for a good representation of all the MHD spectrum {8}.

c) Normalization

To avoid problems involved with a specific unit system, we define dimensionless variables

$$\begin{aligned} \tilde{r} &= \frac{r}{R_0} , & \tilde{B} &= \frac{B}{B_0} , & \tilde{\Psi} &= \frac{\Psi}{\Psi_s} \\ \tilde{p} &= \frac{p}{B_0^2} , & \tilde{\rho} &= \frac{\rho}{\rho_0} , & \tilde{\omega}^2 &= \frac{\omega^2 R_0^2}{B_0^2 \rho_0} \end{aligned} \quad (2.20)$$

R_0 is the radius of the magnetic axis, B_0 the toroidal magnetic field at the axis, ρ_0 the density at the same point and Ψ the flux at the plasma surface. Frequencies are normalized with the inverse transit time for an Alfvén wave in the toroidal field $\omega_T^2 = T^2(R_0)/R_0^4 \rho_0$.

d) Fourier Analysis, Up-down Symmetry

Since we consider axisymmetric equilibria it is possible to decouple Fourier components in the toroidal direction. We write

$$\begin{aligned} \bar{X} &= X^R \cos n\varphi + X^I \sin n\varphi \\ \bar{Y} &= Y^R \cos n\varphi + Y^I \sin n\varphi \\ \bar{V} &= V^R \cos n\varphi + V^I \sin n\varphi , \end{aligned} \quad (2.21)$$

n is the toroidal wave number.

For equilibria which are symmetric with respect to the $z = 0$ plane, the analysis of W_p shows that x^I, v^R, y^R (x^R, v^I, y^I) can be assumed to have up-down symmetry and antisymmetry, respectively. This is an advantage of a real Fourier analysis. This property is used to perform the MHD stability study in the half-space $z \geq 0$ only.

3.2 Vacuum Potential Energy

The vacuum potential energy is given by

$$W_V = \frac{1}{2} \int_{\Omega_V} d\Omega_V \delta \underline{B}_V^2 \quad (2.22)$$

with $\delta \underline{B}_V = \underline{\nabla} \times \underline{A}$ and boundary conditions (2.13), (2.14).

For an $n \neq 0$ perturbation or for an axisymmetric mode which does not change the volume of the plasma, it is possible to write $\delta \underline{B}_V = \underline{\nabla} \phi$ {23,24} where ϕ is a single-valued scalar potential, thus avoiding Lüst and Martensen terms {25} associated with flux conservation.

$\underline{\nabla} \cdot \delta \underline{B}_V = 0$ leads to the following equation for ϕ :

$$\nabla^2 \phi = 0 \quad (2.23)$$

with the boundary conditions obtained by taking the divergence of relations (2.13) and (2.14)

$$\frac{d\phi_p}{dn} = \underline{n} \cdot \underline{Q} = \frac{T}{r^2 B_p} F(X) \quad (\text{plasma surface}) \quad (2.24)$$

$$\frac{d\phi_w}{dn} = 0. \quad (\text{wall}) \quad (2.25)$$

Using (2.22), (2.23) together with Green's theorem, we obtain

$$W_V = -\frac{1}{2} \int_{\partial\Omega} d\sigma \phi \frac{d\phi}{dn} = -\frac{q_s}{2} \int d\chi d\varphi \phi F(X). \quad (2.26)$$

Instead of solving (2.23) inside all the vacuum region, it is possible to use a Green function technique to reduce the problem to an integral-differential equation on both the plasma and shell surfaces {8, 23, 24} :

$$\begin{aligned} \phi_p(\underline{x}_p) = & -\frac{1}{2\pi} \int_{\partial\Omega_p} d\sigma' \frac{d\phi}{dn'}(\underline{x}') G(\underline{x}_p, \underline{x}') + \\ & + \frac{1}{2\pi} \int_{\partial\Omega_p} d\sigma' \underline{n}' \cdot \underline{\nabla}' G(\underline{x}_p, \underline{x}') \phi_p(\underline{x}') - \\ & - \frac{1}{2\pi} \int_{\partial\Omega_w} d\sigma' \underline{n}' \cdot \underline{\nabla}' G(\underline{x}_p, \underline{x}') \phi_w(\underline{x}') \end{aligned} \quad (2.27)$$

$$\begin{aligned} \phi_w(\underline{x}_w) = & -\frac{1}{2\pi} \int_{\partial\Omega_p} d\sigma' \frac{d\phi}{dn'}(\underline{x}') G(\underline{x}_w, \underline{x}') + \\ & + \frac{1}{2\pi} \int_{\partial\Omega_p} d\sigma' \underline{n}' \cdot \underline{\nabla}' G(\underline{x}_w, \underline{x}') \phi_p(\underline{x}') - \\ & - \frac{1}{2\pi} \int_{\partial\Omega_w} d\sigma' \underline{n}' \cdot \underline{\nabla}' G(\underline{x}_w, \underline{x}') \phi_w(\underline{x}') , \end{aligned} \quad (2.28)$$

with $G(\underline{x}, \underline{x}') = 1/|\underline{x}-\underline{x}'|$, the Green function for gravitation problem, ϕ_p the value of ϕ at the plasma surface and ϕ_w the value on the shell.

In order to avoid the integrable singularity of the $\underline{n}' \cdot \underline{\nabla}' G$ function, we use the following identity

$$\int_{d\Omega} d\sigma' \underline{n}' \cdot \underline{\nabla}' G(\underline{x}, \underline{x}') = \begin{cases} 0 & \text{if } \underline{x} \text{ is inside the} \\ & \text{volume limited by } \partial\Omega \\ -2\pi & \text{if } \underline{x} \text{ is on } \partial\Omega \\ -4\pi & \text{if } \underline{x} \text{ is outside the} \\ & \text{volume limited by } \partial\Omega \end{cases}$$

Adding this term in both sides of (2.27) and (2.28) leads to {26}

$$\begin{aligned} 2\phi_p(\underline{x}_p) - 2\phi_w(\underline{x}_w) &= -\frac{1}{2\pi} \int_{\partial\Omega_p} d\sigma' \frac{d\phi}{dn'} G(\underline{x}_p, \underline{x}_p') + \\ &+ \frac{1}{2\pi} \int_{\partial\Omega_p} d\sigma' \underline{n}' \cdot \underline{\nabla}' G(\underline{x}_p, \underline{x}_p') [\phi_p(\underline{x}_p') - \phi_p(\underline{x}_p)] - \\ &- \frac{1}{2\pi} \int_{\partial\Omega_w} d\sigma' \underline{n}' \cdot \underline{\nabla}' G(\underline{x}_p, \underline{x}_w') [\phi_w(\underline{x}_w') - \phi_w(\underline{x}_w)] \end{aligned} \quad (2.29)$$

$$\begin{aligned} 0 &= -\frac{1}{2\pi} \int_{\partial\Omega_p} d\sigma' \frac{d\phi}{dn'} G(\underline{x}_w, \underline{x}_p') + \\ &+ \frac{1}{2\pi} \int_{\partial\Omega_p} d\sigma' \underline{n}' \cdot \underline{\nabla}' G(\underline{x}_w, \underline{x}_p') [\phi_p(\underline{x}_p) - \phi_p(\underline{x}_p')] - \\ &- \frac{1}{2\pi} \int_{\partial\Omega_w} d\sigma' \underline{n}' \cdot \underline{\nabla}' G(\underline{x}_w, \underline{x}_w') [\phi_w(\underline{x}_w) - \phi_w(\underline{x}_w')]. \end{aligned} \quad (2.30)$$

\underline{x}_p^w designates the projection of \underline{x}_p on the wall (see Fig. 2.2).

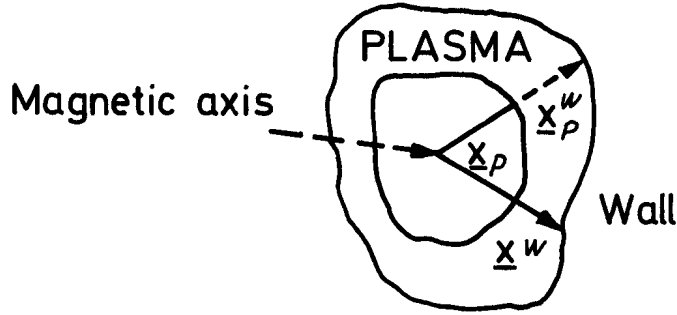


Figure 2.2 Definition of \underline{x}_p^w

Performing the Fourier analysis $\phi(\underline{x}) = \phi(\underline{x}_\perp) e^{in\varphi}$ (\underline{x}_\perp denotes the poloidal component of \underline{x}) and taking the projection of (2.29) and (2.30) on each basis function $e^{in\varphi}$ leads to the same formal equation as (2.29) and (2.30), but with $G(\underline{x}, \underline{x}')$ replaced by $G_n(x_\perp, x'_\perp)$.

$$G_n(x_\perp, x'_\perp) = \int_0^{2\pi} du \frac{\cos n u}{[r^2 + r'^2 + (z' - z)^2 - 2rr' \cos u]^{1/2}}$$

$$= \frac{4(-1)^n}{[(r'+r)^2 + (z'-z)^2]^{1/2}} K_n(\eta) \quad (2.31)$$

$$\eta = \frac{(r'-r)^2 + (z'-z)^2}{(r'+r)^2 + (z'-z)^2}$$

Note that K_n is expressed by a recurrence relation in terms of the complete elliptic integral of the first and second kind [24].

Solution of (2.29) and (2.30) furnishes the Green's function of the problem $G_F(\underline{x}, \underline{x}')$ such that

$$\phi_p(\underline{x}_p) = q_s \oint G_F(\underline{x}_p, \underline{x}'_p) F'(X) dX'. \quad (2.32)$$

Then the vacuum potential energy can be written as

$$W_V = -\frac{1}{2} q_s^2 \int dX dX' G_F(x_{-p}, x'_p) F(X) F'(X) . \quad (2.33)$$

The treatment of the remaining singularity of G_n is mentioned briefly in Chapter IV.

3.3 Localized Stability Criterion

The Mercier criterion {1,2} is a convenient diagnostic to evaluate stability of an equilibrium against localized modes. It is a necessary condition corresponding to the Suydam criterion in the cylindrical case. The connection between the Mercier criterion and real stability domains will be one of our goals. The Mercier criterion can be represented as

$$M = M_s + M_u + M_p > 0 \quad \{28\}$$

the three terms representing contribution from the shear, the magnetic well and the finite plasma pressure, respectively. These terms can be written, using surface quantities, as

$$\begin{aligned} M_s &= \frac{1}{4} \left\{ \frac{d}{d\psi} \left[\oint \frac{T}{r^2 B_p} dl \right] \right\}^2 = \frac{1}{4} S^2 \\ M_u &= -p' T S \oint \frac{dl}{r^2 B_p^3} + p' \frac{d}{d\psi} \left[\oint \frac{dl}{B_p} \right] \left\{ T^2 \oint \frac{dl}{r^4 B_p^3} + \oint \frac{dl}{r^2 B_p} \right\} \\ M_p &= -p'^2 \left\{ T^2 \oint \frac{dl}{r^4 B_p^3} \oint \frac{dl}{B_p^3} - T^2 \left[\oint \frac{dl}{r^2 B_p^3} \right]^2 + \right. \\ &\quad \left. + \oint \frac{dl}{r^2 B_p} \oint \frac{dl}{B_p^3} \right\} . \end{aligned} \quad (2.34)$$

This criterion tests if the lower limit to the continuum $\omega^2 = 0$ becomes also an accumulation point for unstable modes {27}. For common profiles, the Mercier criterion can only be violated near the magnetic axis.

We have presented the notions we need to build a numerical spectral MHD stability code. Chapter III will deal with the problem of the approximation of the MHD spectrum in a toroidal geometry.

III NUMERICAL SCHEME. CODE STRUCTURE

This chapter deals with the numerical methods used to approximate expressions given in Chapter II. All the discretization is supported by a "finite hybrid elements" scheme [10]. Let us first look at the plasma potential energy.

1. Plasma Potential Energy Approximation

Two major facts have to be taken into account. The quantity $\nabla \cdot (\underline{\xi}/r^2)$ corresponding to the 2nd square of the Lagrangian (see Chapter II) becomes very small for a kink mode. In the same way, the operator $\underline{B} \cdot \nabla$ vanishes on each singular surface. Moreover, these two terms are zero for marginal continuum spectra [22]. To correctly represent all unstable modes, it is necessary to respect these features. If the first condition can be fulfilled with a finite element discretization, it is not the case for the second one as it involves a function and its derivative. The main idea of the finite hybrid element scheme is to consider each derivative as a new variable, writing the energy principle as

$$\delta \mathcal{L} \left(\frac{\partial X^{(1)}}{\partial \chi}, X^{(2)}, \frac{\partial X^{(3)}}{\partial \psi}, \frac{\partial Y^{(1)}}{\partial \chi}, Y^{(2)}, \frac{\partial V^{(1)}}{\partial \chi}, V^{(2)} \right) = 0 \quad (3.1)$$

with the trivial conditions

$$\begin{aligned} X^{(1)} &= X^{(2)} = X^{(3)} \\ Y^{(1)} &= Y^{(2)} \\ V^{(1)} &= V^{(2)} \end{aligned} \quad (3.2)$$

We choose for each of the 7 unknowns finite element basis functions making each term of (3.1), piece-wise constant on each (Ψ, X) cell.

We write

$$X^{(1)} = \sum \sum X_{i+\frac{1}{2}j}^{(1)} e_{i+\frac{1}{2}j}$$

$$X^{(2)} = \sum \sum X_{i+\frac{1}{2}j+\frac{1}{2}}^{(2)} f_{i+\frac{1}{2}j+\frac{1}{2}}$$

$$X^{(3)} = \sum \sum X_{ij+\frac{1}{2}}^{(3)} g_{ij+\frac{1}{2}}$$

$$Y^{(1)} = \sum \sum Y_{i+\frac{1}{2}j}^{(1)} e_{i+\frac{1}{2}j} \tag{3.3}$$

$$Y^{(2)} = \sum \sum Y_{i+\frac{1}{2}j+\frac{1}{2}}^{(2)} f_{i+\frac{1}{2}j+\frac{1}{2}}$$

$$V^{(1)} = \sum \sum V_{i+\frac{1}{2}j}^{(1)} e_{i+\frac{1}{2}j}$$

$$V^{(2)} = \sum \sum V_{i+\frac{1}{2}j+\frac{1}{2}}^{(2)} f_{i+\frac{1}{2}j+\frac{1}{2}} .$$

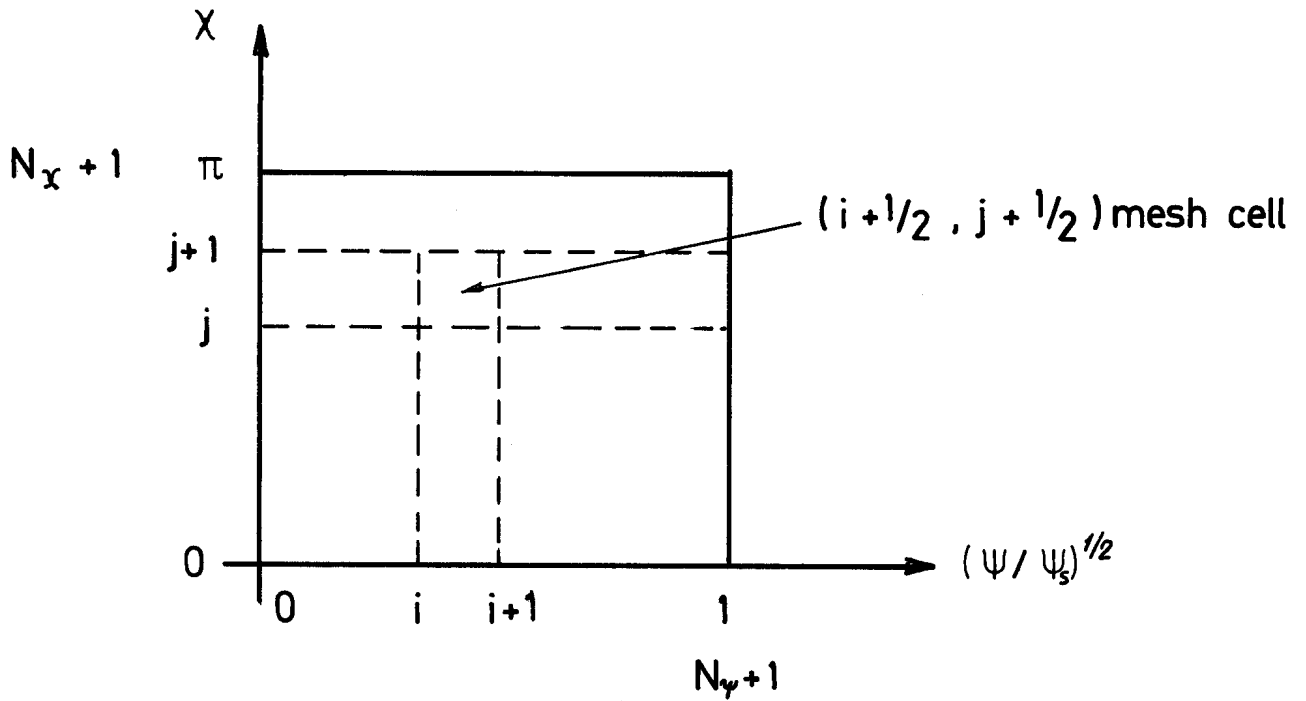


Figure 3.1
Discretization mesh (Ψ, X)

N_Ψ is the number of discretization points in the Ψ -direction and N_X in the X -direction.

Note that $e_{i+\frac{1}{2}j}$ is linear in X and piecewise constant in $\Psi^{\frac{1}{2}}$, $g_{i+\frac{1}{2}}$ is linear in $\Psi^{\frac{1}{2}}$ and piecewise constant in X and $f_{i+\frac{1}{2}j+\frac{1}{2}}$ is piecewise constant.

The condition (3.2) is imposed at the middle point $(i+\frac{1}{2}, j+\frac{1}{2})$ of each cell, leading to the relations

$$\begin{aligned}
 X_{i+\frac{1}{2}j+\frac{1}{2}}^{(2)} &= \frac{X_{i+\frac{1}{2}j}^{(1)} + X_{i+\frac{1}{2}j+1}^{(1)}}{2} \\
 X_{i+\frac{1}{2}j+\frac{1}{2}}^{(2)} &= \frac{X_{ij+\frac{1}{2}}^{(3)} + X_{i+1j+\frac{1}{2}}^{(3)}}{2} \\
 Y_{i+\frac{1}{2}j+\frac{1}{2}}^{(2)} &= \frac{Y_{i+\frac{1}{2}j}^{(1)} + Y_{i+\frac{1}{2}j+1}^{(1)}}{2} \\
 V_{i+\frac{1}{2}j+\frac{1}{2}}^{(2)} &= \frac{V_{i+\frac{1}{2}j}^{(1)} + V_{i+\frac{1}{2}j+1}^{(1)}}{2} .
 \end{aligned} \tag{3.4}$$

Putting (3.3) and (3.4) in the Lagrangian expression, we obtain in matrix form

$$\mathcal{L} = \langle x_i | A_{ij} | x_j \rangle - \omega^2 \langle x_i | K_{ij} | x_j \rangle \tag{3.5}$$

$\{A_{ij}\}$ is the matrix potential energy

$\{K_{ij}\}$ the norm matrix and

$\{x_i\}$ a vector containing the value of X,Y,V at each point $(i+\frac{1}{2}, j+\frac{1}{2})$.

Each equilibrium quantity involved in \mathcal{L} is approximated by piecewise constant functions on each cell. Integration is trivially performed.

We now want to describe the last term to discretize the vacuum contribution.

2. Vacuum Discretization

We use a numerical technique consistent with the plasma discretization, writing {24}

$$\begin{aligned}\phi_p &= \sum_i \phi_i^p e_i(\chi) \\ \phi_w &= \sum_j \phi_j^w e_j(\theta)\end{aligned}\tag{3.6}$$

$e_i(\chi)$ and $e_j(\theta)$ are piecewise constant functions and θ is the angle of the polar system centered on the magnetic axis (cf. Figure 3.2).

$$F(\chi) = \sum_i F(\chi)_i e_i(\chi) = \sum_i \left(\frac{1}{q} \frac{\chi_{i+1} - \chi_i}{\Delta\chi} - n \frac{\chi_{i+1} + \chi_i}{2} \right)$$

which is equivalent to

$$F(\chi)_i = C_{ij} X_j\tag{3.7}$$

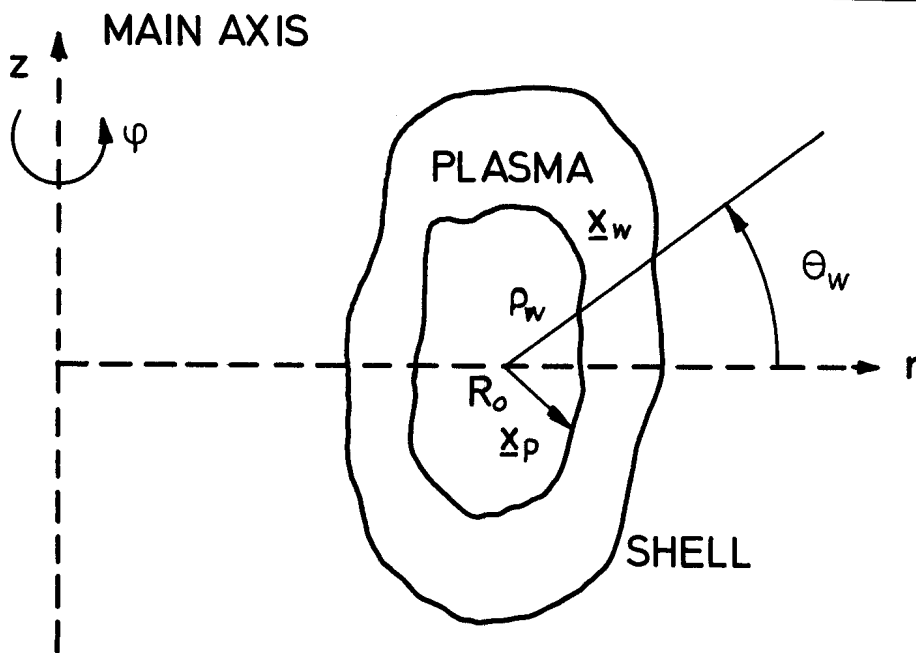


Figure 3.2

Plasma and wall definition

Inserting (3.6) into (2.29) and (2.30), we obtain a set of coupled matrix equations

$$\begin{aligned}
 2\phi_i^P - 2\phi_i^W &= \overbrace{(A_{ij} - \delta_{ij})}^{\underline{A}} \phi_j^P - \overbrace{B_{ij}}^{\underline{B}} [F(X)]_j - \overbrace{(C_{ij} - 2\delta_{ij})}^{\underline{C}} \phi_j^W \\
 0 &= \overbrace{(D_{ij} - \delta_{ij})}^{\underline{D}} \phi_j^P - \overbrace{E_{ij}}^{\underline{E}} [F(X)]_j - \overbrace{(F_{ij} - \delta_{ij})}^{\underline{F}} \phi_j^W
 \end{aligned} \tag{3.8}$$

The matrices are formally equivalent to (2.27) and (2.28) with ϕ or $\frac{d\phi}{dn}$ replaced by $e_i(X)$. The matrix elements of \underline{A} , \underline{C} and \underline{F} are regular and can be integrated numerically by a four-point integration scheme in the (X, θ_w) plane. The diagonal elements of B and E exhibit an integrable logarithmic singularity which is treated specially [24]. Around $\eta = 0$, where η is defined in (2.31), we expand η to second order in $(\theta' - \theta)$ and obtain

$$K_n \cong \ln \eta \cong \frac{(-1)^{n+1}}{2} \ln [a_1^2 + a_2(\theta' - \theta) + (\theta' - \theta)^2].$$

a_1 is the normal distance between the observation P and integration point P'. θ and θ' are the polar angles of P and P', respectively. We write K_n in the form

$$K_n = S_n + \{ K_n - S_n \}$$

$$S_n = \frac{(-1)^{n+1}}{2} \ln [a_1^2 + a_2(\theta' - \theta) + (\theta' - \theta)^2].$$

The first part is integrated analytically, the second numerically.

Eliminating Φ^W from eq. (3.8), we get

$$\phi_i^P = G_{ij}^F [F(X)]_j \quad (3.9)$$

with

$$\underline{G}^F = \left[(\underline{A} - 2\underline{I}) - (\underline{C} - 2\underline{I}) \underline{F}^{-1} \underline{D} \right]^{-1} \left[\underline{B} - (\underline{C} - 2\underline{I}) \underline{F}^{-1} \underline{E} \right]$$

Inserting (3.9) into (2.33), we get

$$W_V = -\frac{1}{2} \sum_{i,j} q_s^2 [F(X)]_i G_{ij}^F [F(X)]_j \quad (3.10)$$

and finally, by (3.7),

$$W_V = -\frac{1}{2} \sum q_s^2 C_{ik} G_{ij}^F C_{lj} X_k X_l. \quad (3.11)$$

This $\{W_{ij}\}$ matrix is added to $\{A_{ij}\}$ obtained in Chapter III.1.

3. Equilibrium and Mapping

3.1 Numerical Equilibria

We solve the partial differential equation (2.10) for $\Psi(r,z)$ by using the equilibrium code written by J.D. Callen and R.A. Dory [29]. The function $p(\Psi)$ and $T(\Psi)$ can be chosen arbitrarily. The non-linearity of the second member is treated by a two level iteration scheme with an adjustable drag parameter α :

$$\Psi^{i+1} = \Psi^i + (1-\alpha) \Psi_T^{i+1}$$

$$\nabla^* \Psi_T^{i+1} = f(\Psi_i)$$

The boundary surface $\partial\Omega$ is specified and $\Psi(\underline{x}) = 0$ for $\underline{x} \in \partial\Omega$. Note that ERATO can use any equilibrium code which furnishes $\Psi(r,z)$, $p'(\Psi)$ and $TT'(\Psi)$.

The link with the stability code requires that r and z be specified as functions of Ψ and χ . We proceed in the following manner. Given Ψ , we localize in the (r,z) mesh all points (r^k, z^k) by a linear interpolation (Fig.3.3) :

$$r^k = r_i + \frac{\Psi - \Psi_i}{\Psi_{i+1} - \Psi_i} (r_{i+1} - r_i) , \quad z^k = z_j$$

and

$$z^k = z_j + \frac{\Psi - \Psi_j}{\Psi_{j+1} - \Psi_j} (z_{j+1} - z_j) , \quad r^k = r_i .$$

Note that this approximation is compatible with our stability discretization scheme.

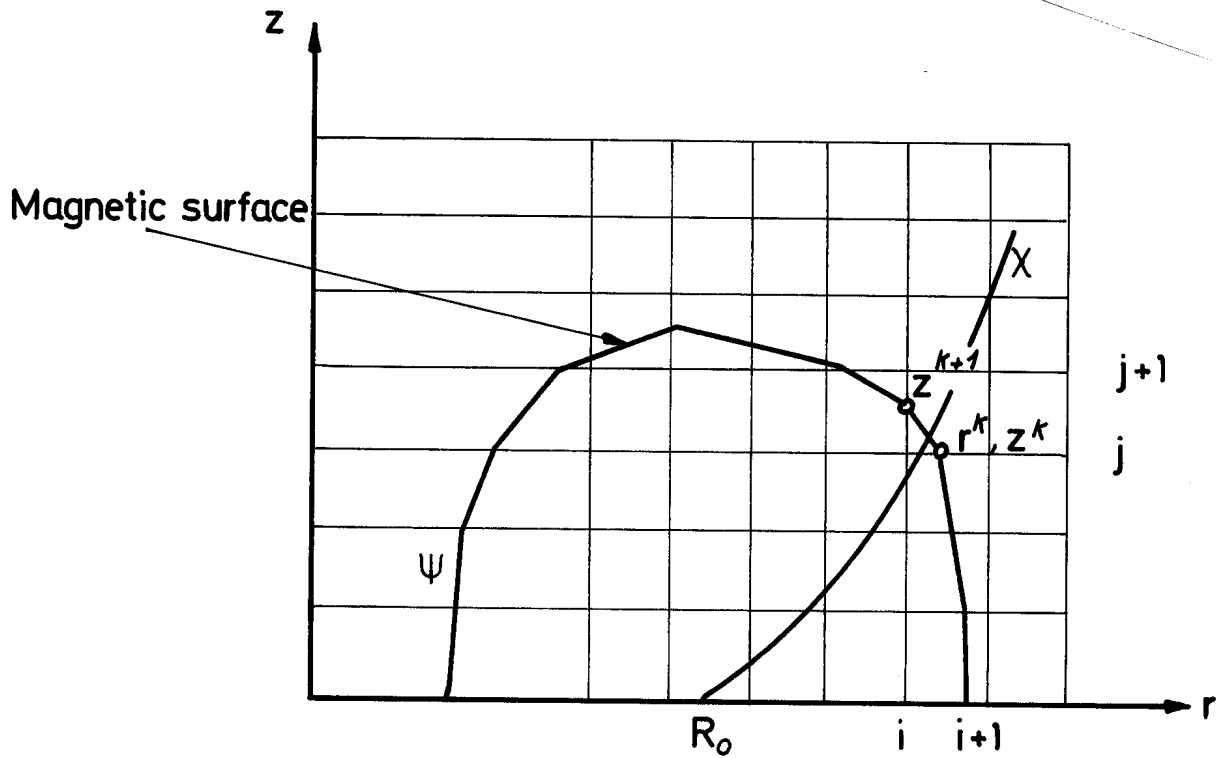


Figure 3.3

Discretization (r, z) mesh and mapping procedure

The coordinate system satisfies the relation

$$\chi = \int_0^l \frac{T}{9B_p r^2} dl \quad (2.16)$$

The integral is computed on the solid curve plotted in Fig. 3.3 and gives χ^k at each (r^k, z^k) points. For a given χ we have

$$r(\chi) = r^k + \frac{\chi - \chi^k}{\chi^{k+1} - \chi^k} (r^{k+1} - r^k)$$

$$z(\chi) = z^k + \frac{\chi - \chi^k}{\chi^{k+1} - \chi^k} (z^{k+1} - z^k).$$

The procedure is the same for $\frac{\partial \Psi}{\partial r}$, $\frac{\partial \Psi}{\partial z}$, $\frac{\partial^2 \Psi}{\partial r^2}$, $\frac{\partial^2 \Psi}{\partial z^2}$, $\frac{\partial^2 \Psi}{\partial r \partial z}$ quantities which are given at the grid mesh (r, z) by the equilibrium code and used at a (Ψ, χ) point by the stability code.

All quantities needed for stability are computed in this way. A special choice of function p , T leads to an analytical solution for Ψ ; the next section will treat this case.

3.2 Solovév Equilibrium {12}

We choose for the functions in (2.10)

$$p(\Psi) = -p_0' (\Psi_s - \Psi)$$

$$T^2(\Psi) = T_0^2 - \frac{4 \Psi_s d}{E^2 a^2} \Psi$$

Ψ_s is the poloidal flux at the plasma surface, a the length which characterizes the plasma width, E a dimensionless parameter which describes the elongation of the plasma and d a parameter related to the poloidal beta β_p and the triangularization of the plasma. The half-width of the plasma is given by $(R^2 + 2aR)^{\frac{1}{2}} - (R^2 - 2aR)^{\frac{1}{2}}$, which reduces to $2a$ when $a \ll R$. We shall refer to R_0/a as the aspect ratio. It can vary between 2 and ∞ . When it is 2, the plasma extends to $r=0$ and has a width of $\sqrt{2} R$.

A solution of (2.10) is

$$\Psi = \frac{\Psi_s}{a^2 R_0^2} \left\{ \frac{r^2(1-d) + d}{E^2} z^2 + \frac{(r^2 - R_0^2)^2}{4} \right\}, \quad (3.12)$$

In the limit of large aspect ratio, the equilibrium (3.12) reduces to the constant current equilibrium of Gajewski [30], in which the plasma is elliptical, a being the minor axis and Ea the major axis. For arbitrary aspect ratio, we shall still refer to E as the elongation. For $d=0$ the toroidal magnetic field B is a vacuum field. The equilibrium (3.12) is referred as a Solovév equilibrium [12]. The equilibrium is fully characterized by 6 parameters R_0 , a , E , d , Ψ_s and B_0 . It is convenient to replace Ψ_s by the safety factor on axis q_0

$$\Psi_s = \frac{E B_0 a^2}{2 q_0} .$$

By inspection of the various terms of the Lagrangian, one sees that two of the 6 parameters, B_0 and R_0 , appear only in the normalization $\omega_T^2 = B_0^2 / \rho_0^2 R_0^2$. The 4 remaining parameters are R_0/a , E , q_0 and d .

This equilibrium makes possible a study of the effect of geometry on the MHD spectrum. The parameters $a/R_0 = 1/3$, $E = 2$, $d = 0$ roughly correspond to the JET design [31]. Note that the peak value of β on axis is given by $\beta_{\text{axis}} = \frac{(E + 1 - d)a^2}{q_0^2 R_0^2}$.

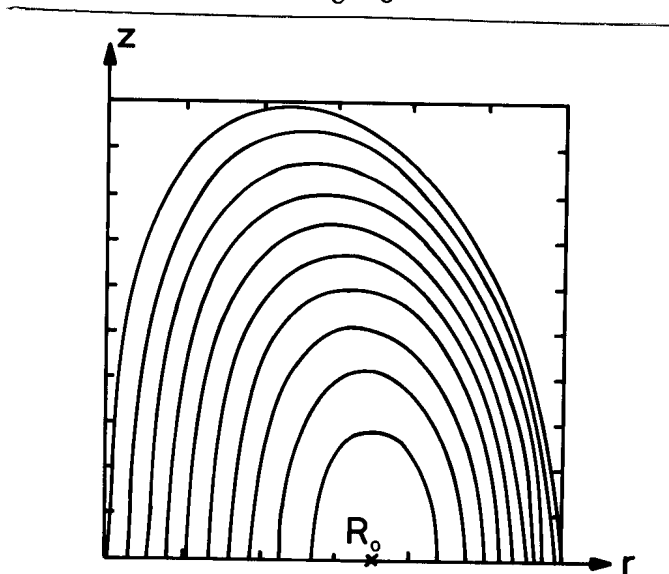


Figure 3.4

Solovév equilibrium. Plot of magnetic surfaces. Geometric parameters are $R/a \approx 3$, $E = 2$, $d = 0$.

In Fig. 3.4 we plot the magnetic surfaces corresponding to the JET parameters. The elongated D-shape form is evident. This class of equilibria has been chosen {32} as a test case {9} for stability codes {8,11,13}.

Despite this good behaviour, we must remark that the toroidal current density is

$$j_y = p' r - \frac{2 \psi_s d}{a^2 R_o^2 E^2 (1-d)} \frac{1}{r} \quad (3.13)$$

This form allows a very high beta, but is non-physical. We will keep this fact in mind in the interpretation of the results.

With such an equilibrium it is possible to make an analytical fit as precisely as we want, avoiding problems with numerical errors in the determination of the equilibrium. For this effect, we introduce a variable α defined by

$$r^2 = R_o^2 + 2 a R_o \sqrt{\frac{\psi}{\psi_s}} \cos \alpha .$$

We obtain the relation

$$\chi = \int_0^\alpha d\alpha' \frac{T a^2 E}{2 q_o \left[1 + \frac{2a}{R_o} \sqrt{\frac{\psi'}{\psi_s}} \cos \alpha' \right] \psi_s R_o \left[\frac{1}{1-d} + \frac{2a}{R_o} \sqrt{\frac{\psi'}{\psi_s}} \cos \alpha' \right]^{1/2}}$$

The integral in (3.14) is performed by a Runge-Kutta technique.

Even for cases where the equilibrium is determined numerically, a Solovév equilibrium is used as an approximation around the axis, the precision of the numerical equilibrium being too low.

We are now able to describe the structure of our code.

4. Code Structure

The ERATO code is written in the OLYMPUS form {33} and is composed of 5 programmes with specific functions. We will briefly describe each part and give a flow chart of the code.

ERATO 1 corresponds to the interface with the equilibrium code. Two options can be chosen : either the analytical Solovév equilibrium or the acquisition of $\Psi(r,z)$ stored on the disk by an equilibrium solver. The necessary quantities for stability are computed on each (Ψ, χ) cell and stored on the disk. The Mercier criterion is also plotted.

ERATO 2 computes the vacuum matrix $\{W_{ij}\}$ {24} using the information given by ERATO 1 for the equilibrium surface quantities. Here we can prescribe the shape of the shell arbitrarily. The fixed boundary case is also included. $\{W_{ij}\}$ is stocked on disk.

ERATO 3 the goal of this part is to build the matrices $\{A_{ij}\}$ and $\{K_{ij}\}$. The matrices are treated as a block, corresponding to each magnetic surface. Each block has a length of $8(N_\chi+1)$.

ERATO 4 contains the eigenvalue solver HYMNIA BLOCK {34}. The basic method is an inverse vector iteration scheme. The block structure is preserved and the eigenvalue is controlled by a Rayleigh quotient calculation.

ERATO 5 contains the output procedures and diagnostic of results. The mode can be represented either in the (Ψ, χ) plane by normalized integer arrays, or in the (r, z) space with arrows proportional to the projection of the plasma displacement in the meridian plane.

The diagnostic involves the computation on each discretization cell of the potential and kinetic energy, corresponding to the eigenmode obtained. This leads to a different evaluation of the eigenvalue, which checks all our preceding operations. Finally, a Fourier analysis of (X, Y, V) can be performed on each magnetic surface.

Fig. 3.5 gives a flow chart of ERATO. Note that a high resolution case $N_\psi = 28, N_\chi = 28$, takes 30 min on a CDC 6500 or 3 min on a CDC 7600 {9}.

The code will now be applied to study in detail small aspect-ratio tokamak equilibria. It can be considered as a numerical experiment with exploitation and interpretation problems.

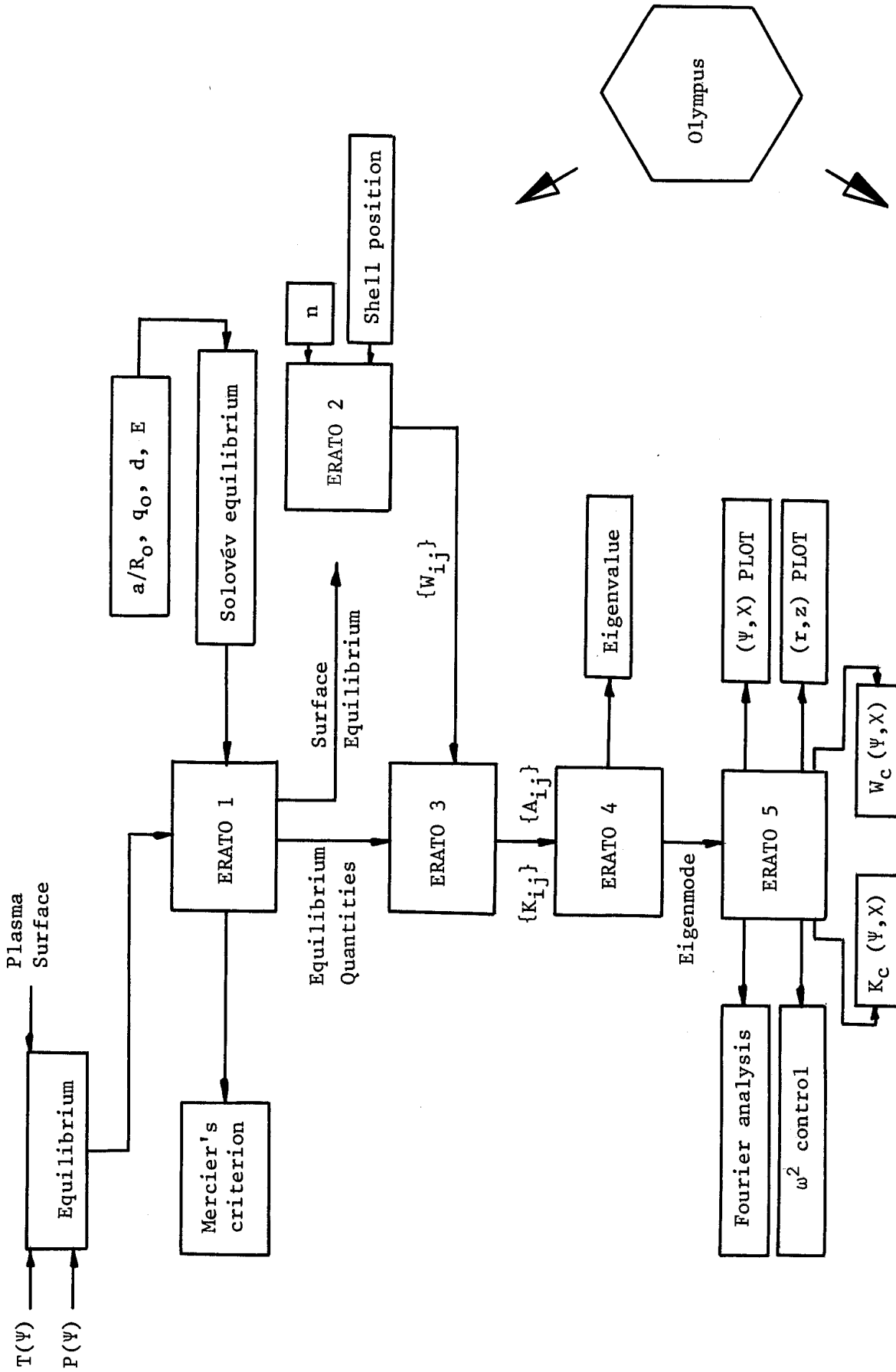


Figure 3.5. ERATO Structure

IV MHD SPECTRUM OF SMALL ASPECT RATIO TOKAMAK WITH "FLAT" CURRENT PROFILE

We now want to investigate the influence of toroidicity and non-circularity on the unstable part of an MHD spectrum. To have a solid reference basis to understand a toroidal spectrum, we choose a simple analytical equilibrium, namely the Solovév equilibrium [12]. The other justification for this choice is explained in Chapter III. In order to have a configuration which has some interest, we choose a fixed aspect ratio $R_0/a = 3$ close to the JET value. This configuration has an appreciable shear since $q(\Psi_S)/q_0 = 1.74$. Section IV.1 deals with axisymmetric modes. For $n \neq 0$: in the first part, the rigid boundary case, a conducting wall touches the plasma; in the latter case, the infinite vacuum case, we have no conducting shell. Details on the position of the shell are given in Section IV.2. The parameter d is set equal to 0, corresponding to a β_p of 1. The numerical results shown have been tested for convergence. The eigenfrequency depends on the density profile, but the marginal state does not. Since we are interested in general features of the unstable mode, we choose a constant density profile $\rho = \rho_0$.

1. Axisymmetric Modes (n=0)

It is a common knowledge that without a conducting shell, non-circular plasma cross sections can be unstable to the axisymmetric $n=0$ modes. Assuming that the most dangerous mode is a rigid vertical displacement, Rebhan [26] has examined with the δw -method, the influence of the plasma shape on its stability. In the unstable range, he has also given an estimation of the growth rate of the fastest growing mode. Solovév's equilibrium is one of the shapes which we studied and the result is that

the plasma is unstable if $E \geq 1.23$. The normalized growth rate is nearly independent of q_0 . Figure (4.1) shows some numerical results. It shows the square of the growth rate Γ^2 normalized to $\omega_A^2 = \omega_T^2 \cdot q_0^2$ versus q_0 for an elongation $E = 2$. The growth rate is a weak function of q_0 which becomes a constant for large q_0 . The mode is purely anti-symmetric with respect to the midplane which provides an a posteriori justification of the neglect of Lüst and Martensen's terms [25].

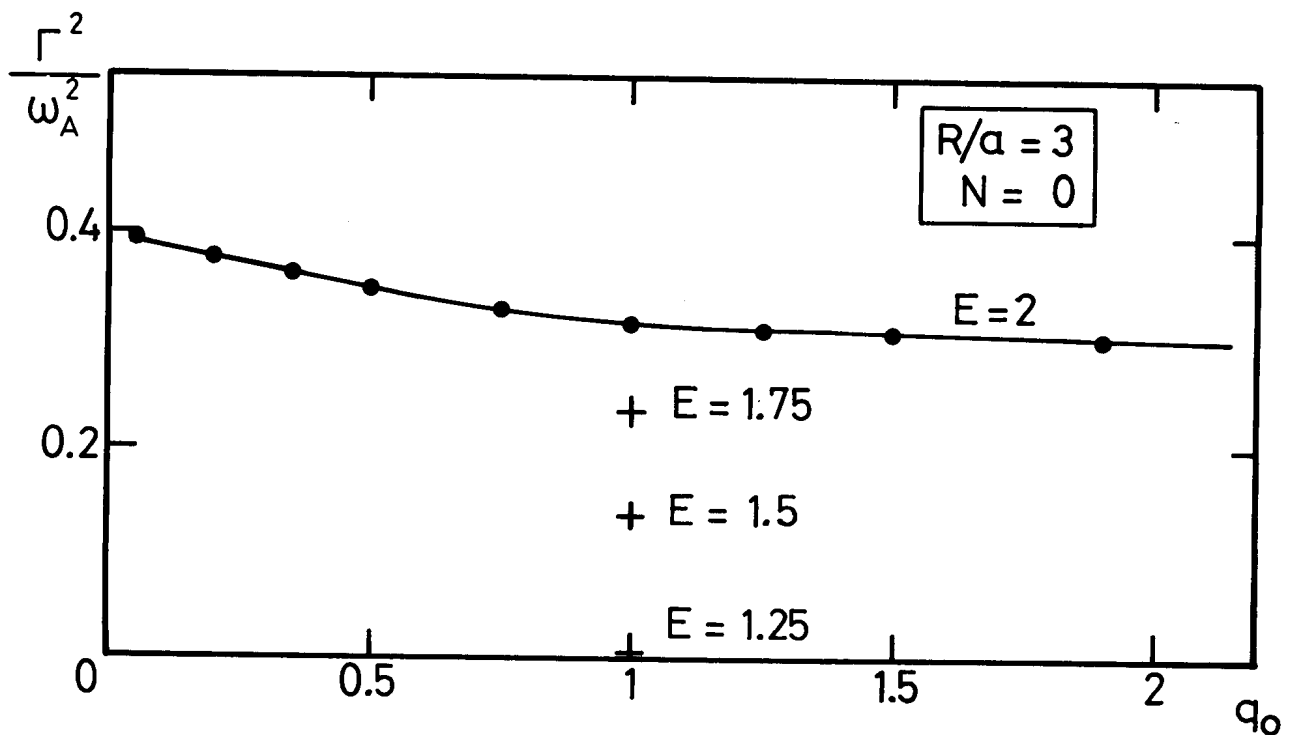


Figure 4.1

Growth rate of the axisymmetric mode as a function of q_0 ($E = 2$)
The variation of Γ^2 versus E , at fixed q_0 is given by crosses.

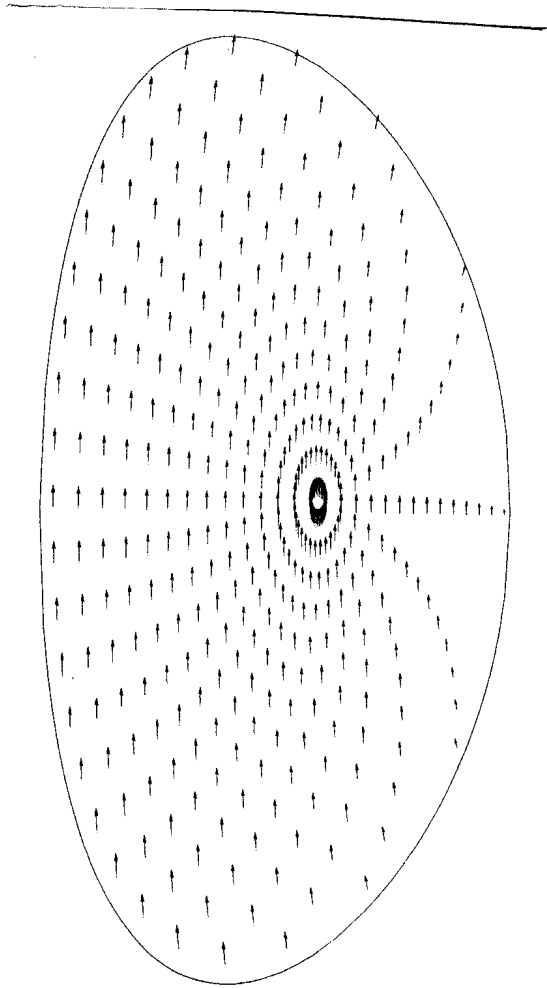


Figure 4.2

Map showing the instantaneous displacement in a meridian plane.
The mode represented corresponds to $E = 2$, $q_0 = 1$ and $d = 0$.

The value of Γ^2 is in a range typical of external kinks. For large q_0 , the motion is essentially a rigid vertical displacement as plotted in Fig. 4.2. The arrows represent $\underline{\xi}$, which has no φ component. The growth rate Γ falls off as q_0^{-1} so that the motion can be visualized as a slow rigid displacement. For small q_0 the growth rate Γ^2 is large, comparable to the toroidal Alfvén speed, so that the motion cannot remain incompressible. The crosses in Fig. 4.1 represent the growth rate, at $q_0 = 1$, for various values of E . The stability limit for $q_0 = 1$ is seen to be $E \approx 1.25$ which is in agreement with Rebhan's result.

1.1 Wall Stabilization

The only efficient way to stabilize an axisymmetric mode is to put a perfect conducting wall around the plasma. In a polar coordinate system centered on the magnetic axis, we define the shell by

$$\rho_w(\theta) = \Lambda \rho_p(\theta) ,$$

where ρ_w , ρ_p are the polar distance to the wall and the plasma respectively and θ the polar angle. In Fig. 4.3 we plot the growth rate of the most unstable mode versus the shell position Λ . The safety factor on axis q_0 is 1.

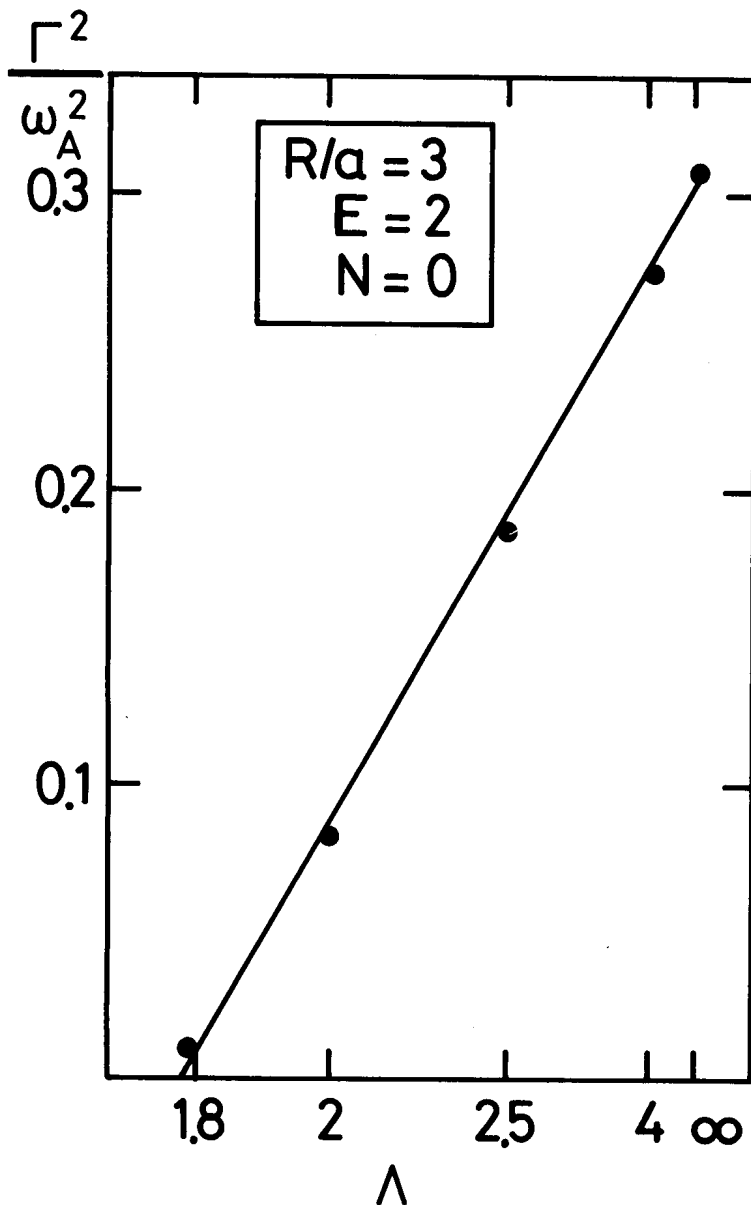


Figure 4.3

Growth rate Γ^2 of the most unstable axisymmetric mode versus the shell position Λ .

$q_0 = 1$.

We see a complete stabilization for $\Lambda = 1.8$. This demonstrates the efficiency of the wall on this global instability. The Λ -value of 1.8 is very high and imposes no technological restriction. In a real experiment the decay of image currents due to the finite resistivity of the shell can be compensated by an active feedback system acting in a time characteristic of a diffusion process.

1.2 X-Point Effects

The hypothesis of a vertical rigid displacement, which was valid in the previous case, leads to the fact that a triangularization of the plasma cross section stabilizes the axisymmetric instability {26}. For a value $d = -0.155$ we have varied the ellipticity E looking for the stability limit. An infinite vacuum surrounds the plasma. The value found of 1.1 is in contradiction with {26}, but agrees with a slip motion assumption {35}. The unstable mode is plotted on Fig. 4.4. The move of the plasma to the X-point (+) is clear. The structure of the mode, the azimuthal Fourier component for example, is directly correlated to the position of X-points {35,36}. Such a mode can be stabilized easily by a wall, for a Λ -value similar to the $d = 0$ case, but a feedback system without a shell, as planned in the divertor study experiment, may not work.

In conclusion, the improvement in $\bar{\beta}$ through the elongation of the plasma cross section leads to a strong axisymmetric instability easily stabilized by a wall at a reasonable distance from the plasma surface.

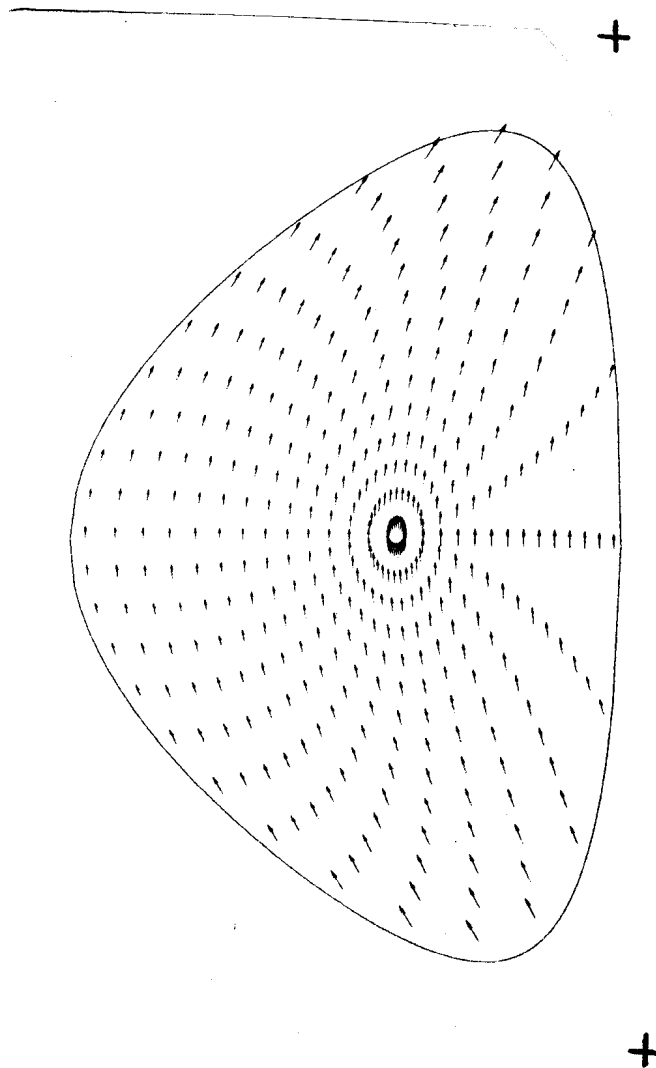


Figure 4.4

Plot of the axisymmetric mode showing the effect of
X-points (+)

2. Rigid Boundary Modes ($n \neq 0$)

Analytic calculations have shown that the MHD continuum spectrum, which is always stable, reaches the marginal point $\omega^2 = 0$ when a singular surface $nq = \ell$ ($\ell = \text{integer}$) lies inside the plasma. If the Mercier criterion

{1,2} is violated, an infinite number of unstable modes localized around a singular surface are expected with eigenfrequencies accumulating at the marginal point. If it is satisfied, there still may be unstable modes, but one expects a finite number of them, by analogy with the straight circular case {27}, and they would be global. In order to gain some insight on how the internal mode spectrum is modified by the toroidicity and non-circularity, we have made a series of runs with a rigid boundary on the plasma surface. External kinks are removed which simplifies the interpretation. The relation between the Mercier limit and the unstable region is investigated. Two cases are considered : $E = 1$ and $E = 2$.

$E = 1$

In order to analyze the results obtained, Fig. 4.5 represents the q -value q_ℓ at which the Mercier criterion is violated, versus the value of q on axis q_0 . The dashed region corresponds to the violated region. Mercier's limit on axis is $q_0 = 1$ in this case.

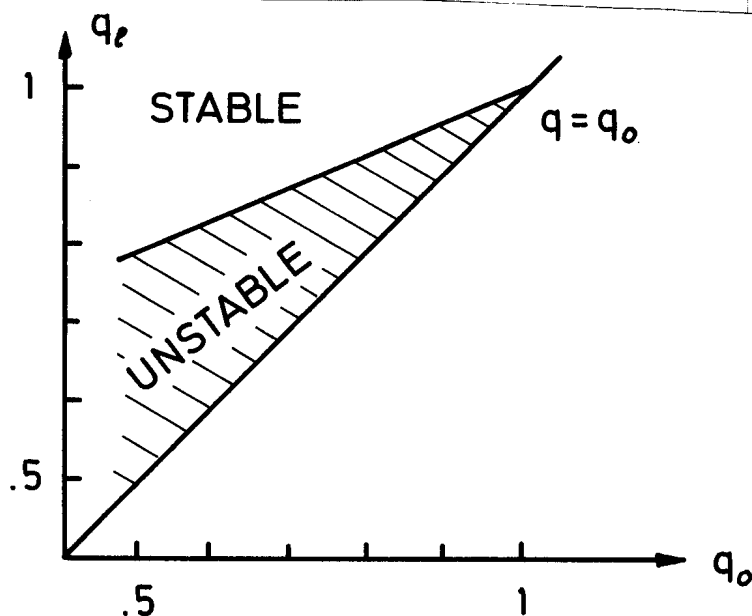


Figure 4.5

Mercier's criterion ($E=1$). The unstable region, limited by q_0 and q_ℓ is plotted versus q_0 .

The square of the normalized growth rate Γ^2 is shown in Fig. 4.6 as a function of q_0 for $n = 2, 3$ and 4 . The line segments on each figure, identified by an integer ℓ , indicate that in this range of q_0 the singular surface $nq = \ell$ lies in the plasma. Note that, because of the shear, there are already many singular surfaces within the plasma in the vicinity of $q_0 = 1$ and the number increases rapidly with n and q_0 .

For $n = 1$ we expect to find an internal kink for $0.6 \leq q_0 \leq 1$, when the singular surface $q_0 = 1$ lies in the plasma. We do not find any unstable mode in this range in agreement with Kerner's results {37, 38}. This fact can be correlated with the non-violation of the Mercier criterion around $q = 1$ for this range of parameter q_0 (Fig. 4.5). We do find unstable modes at low q_0 , just as for all the other values of n shown in Fig. 4.6, but the mode is basically an $m=0$ mode, characteristic of Z-pinch experiments.

In order to discuss the results, it is convenient to introduce an azimuthal number $m(\Psi) = |\text{Arg } X(\Psi, 2\pi) - \text{Arg } X(\Psi, 0)|/2\pi$. It is an integer which reduces to the usual azimuthal number m in straight circular geometry. For $n=2$ there are two unstable regions. The mode which peaks at $q_0 = 0.4$ is $m=1$ everywhere near the maximum, acquiring some $m=0$ or $m=2$ regions in the wings. Near the maximum it exhibits an internal kink mode structure with a step pattern for the normal displacement ξ_Ψ smoothed by high beta and aspect ratio effects. The second faster growing mode is similar, except for an oscillation of ξ_Ψ around the singular layer $nq = 1$. The stability limit in q_0 corresponds roughly to $q_s = 1$ at the plasma surface. The maximum growth rate is down one aspect ratio from the typical growth-rate of an external kink, as expected, but the second unstable mode is down one more order which is unexpected. Compared with the straight infinite cylindrical case, we see three main differences. First the unstable region $q_s \leq 1$ corresponds to the free boundary kink mode of the

straight case but with the growth rate typical of internal modes. Secondly, in the region between $q_s = 1$ and the Mercier limit $q_0 = 1$ we do not find unstable modes due to the thin band where Mercier is violated (Fig. 4.5). Finally, the toroidal component of the displacement is of the same order of magnitude as the other components. This last property is very general and applies to all internal modes. It has been noticed by Soulé et al. {39} in their calculation of the internal kink. The other cases $n=3$ and $n=4$ shown in Fig. 4.6 behave analogously to $n = 2$. The resonant structure of the curves becomes less visible as n increases, due to the increasing number of singular surfaces which lie simultaneously within the plasma. The first resonance starting from the left is purely $m=1$, the second is mostly $m=2$ with $m=3$ near the surface. The third resonance for $n=4$ is a mixture of $m=3$ and 4. The stability limit moves to the right as n increases, but remains below the Mercier limit. It appears that Mercier's limit will be recovered in the limit $n \rightarrow \infty$. A very general feature of the most unstable mode is that locally m is equal to the nearest integer value of nq . For a given value of n , as the number of singular surfaces increases, a stabilization of the mode occurs due to toroidal coupling between surfaces. Note that in the three cases shown in Fig. 4.6 there is still space between the last $m = n-1$ resonance and the Mercier limit. This region is filled with high n and m modes.

E = 2

Figure 4.7 shows in the (q, q_0) plane the region where the Mercier criterion is violated. The Mercier limit corresponds to $q_0 = 1.35$. The main point is that the $q = 1$ surface can lie in the dashed region for some value of q_0 . This feature leads to unstable $n=1, m=1$ modes, in particular, the internal kink, but its growth rate remains much smaller than the other n values.

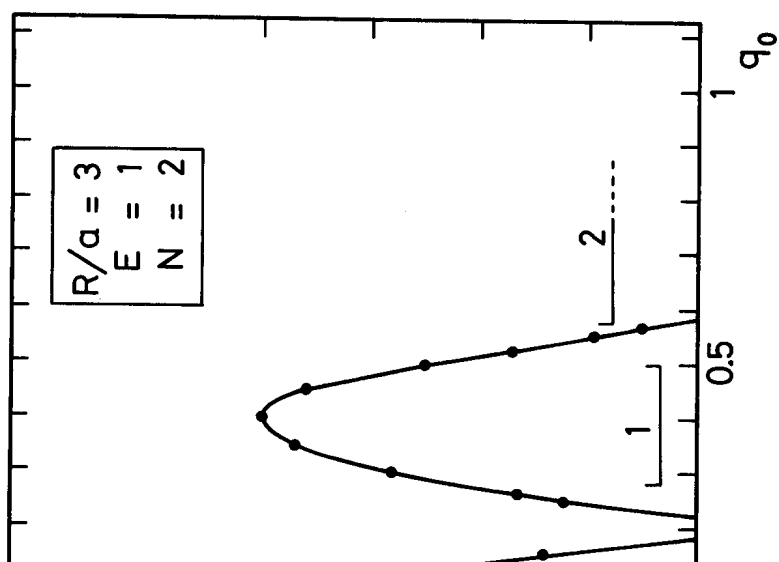
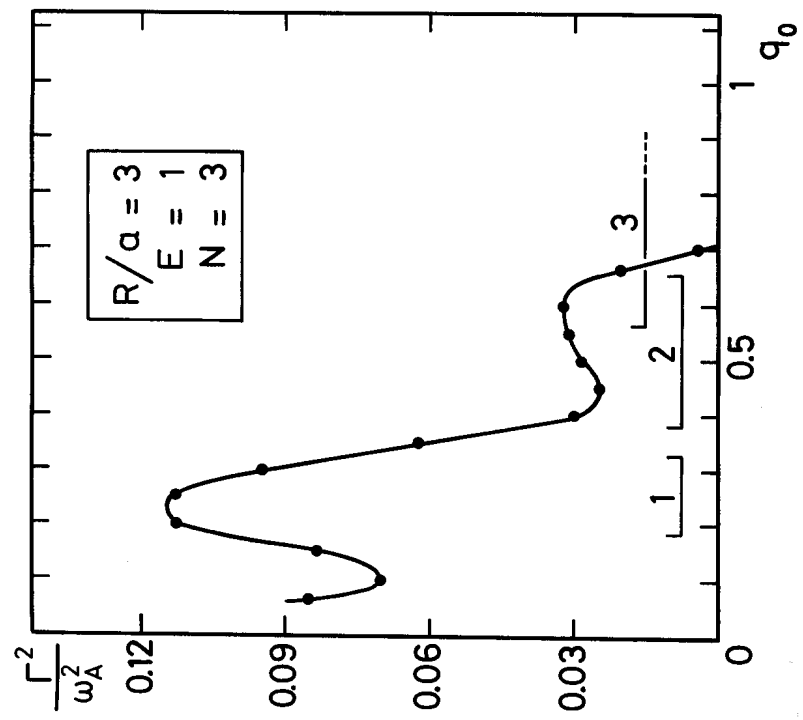
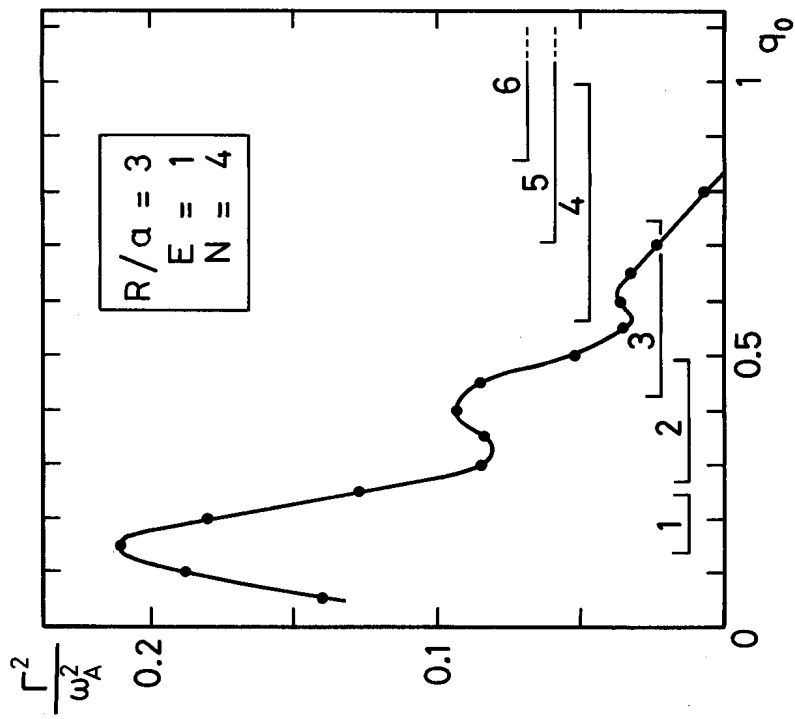


Figure 4.6

The square of the normalized growth rate Γ^2 of the most unstable modes versus the safety factor on the magnetic axis q_0 . Rigid boundary case. $E = 1$ and $n = 2, 3$ and 4 .

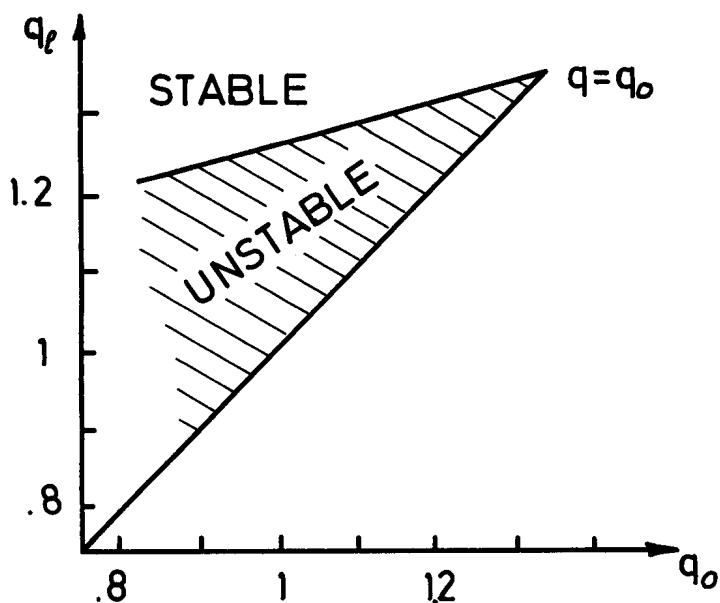


Fig. 4.7 Mercier criterion (E=2). The unstable region limited by q_0 and q_l is plotted versus q_0 .

Fig. 4.8 shows the results obtained for $n = 1, 2$ and 3 . Following the diagram (4.7) the last unstable singular surface occurs for $q_0 = 1.0$, if $n = 1$ or 2 . This limit changes for $n = 3$ where we expect a small unstable region for q_0 -value around $4/3$. For $n = 1$ and 2 , stable modes corresponding to $q_0 > 1$ are called ballooning modes. The definition is the following : unstable displacements for a q_0 -value above the Mercier limit. For $n = 1$, reintroducing the eigenvector into the potential energy W_p , we see that the destabilizing contribution comes from the region with strong unfavourable curvature and extending from the magnetic axis to the surface with a safety factor $q < 1$. For example when $q_0 = 0.8$, the region extends to $q = 0.83$ only. This is very different from the straight case. The destabilizing effect of ellipticity on the internal kink has been predicted by Laval [14]. For $n = 2$ the first peak on the left is still a pure $m=1$ mode. The second peak corresponds to a mode which is mainly $m=2$ with some $m=1$ at the center and $m=3$ near the surface. $n = 3$ modes have the same behaviour with a strong $m=1$ resonance at low q_0 . The fact that resonances become smoothed as nq_0 increases is clearly due to the increasing number of singular surfaces within the plasma. We expect very localized, high n and m modes up to the Mercier limit, so that there is here the same problem as in the E=1 case.

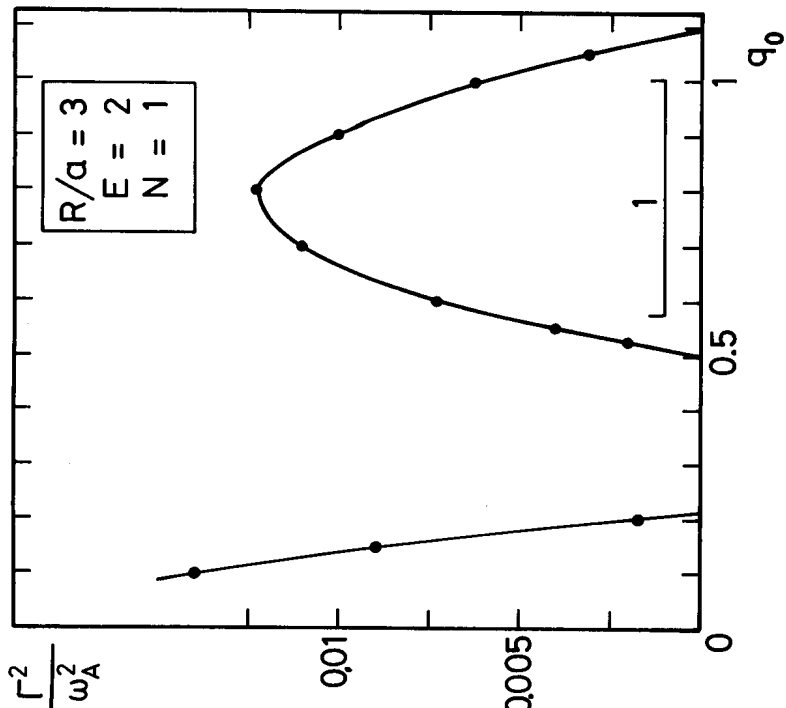
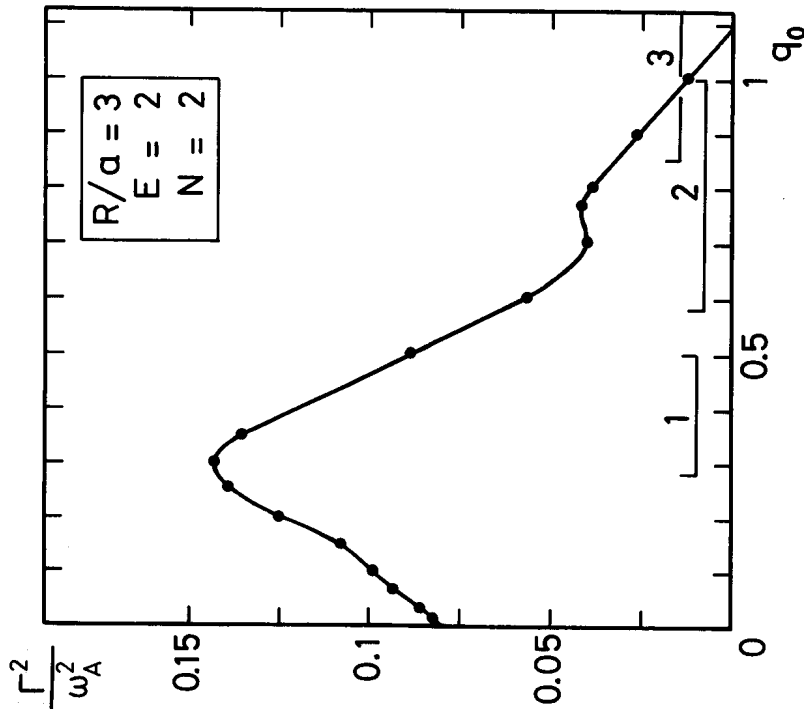
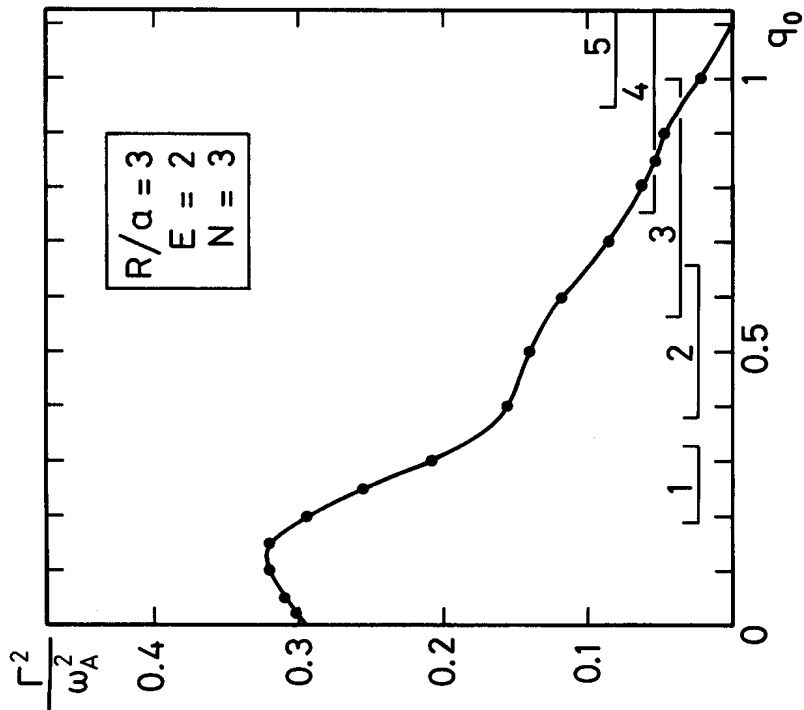


Figure 4.8. The square of the normalized growth rate Γ^2 of the most unstable modes versus q_0 . Rigid boundary case. $E = 2$ and $n = 1, 2$ and 3 .

These results are surprising since they imply that, if q_0 is lowered adiabatically, it is the localized modes with n large which become first unstable. A remarkable fact in this case is the sufficiency of the Mercier criterion for stability against internal modes.

Thus the Solovév equilibria can have very high beta, for example $\beta_{\text{axis}} = 40\%$ for $q_0 = 1.3$ and $E = 2$, with very advantageous behaviour with regard to internal stability. This is not the case for free boundary modes.

3. Free Boundary Modes ($n \neq 0$)

We consider now the case where the plasma is surrounded by an infinite vacuum region. The current density being non-vanishing at the plasma surface, we expect the plasma to be unstable to a global motion, namely the kink mode.

3.1 External Kink

In the limit of a large aspect ratio, the growth rate of the kink is only a function of nq_0 . With a small aspect ratio, we expect to see deviations from this simple dependence. Let us look successively at the two elongations.

$E = 1$

The square of the normalized growth rate of the most unstable mode for $n=1$ and $n=2$, versus q_0 , is shown in Fig. 4.9. The curve has a regular resonant pattern which seems to become periodic as q_0 increases with a period $\Delta q_0 \approx \frac{1.74}{n}$, corresponding to $n \cdot \Delta q = 1$ at the plasma surface. The minima coincide with the presence of a singular surface at the plasma surface. The differences in the nq dependence are visible, specially for the first peak which is higher for $n=2$ than for $n=1$. All the modes have

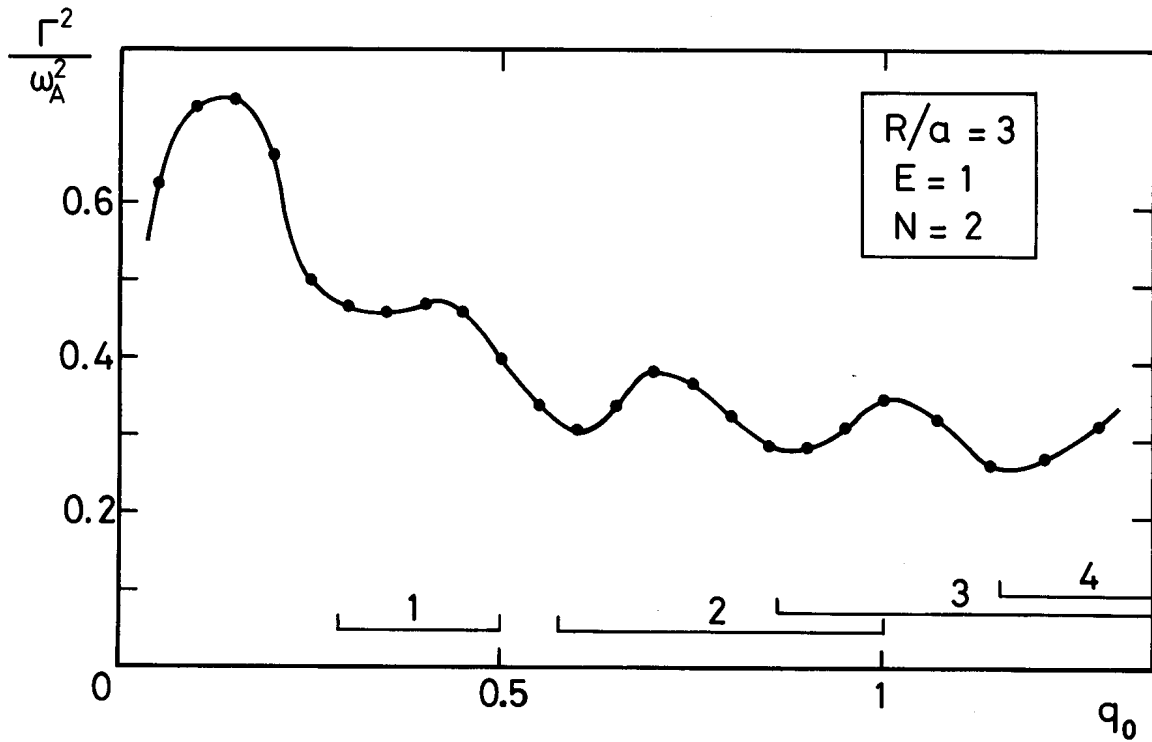
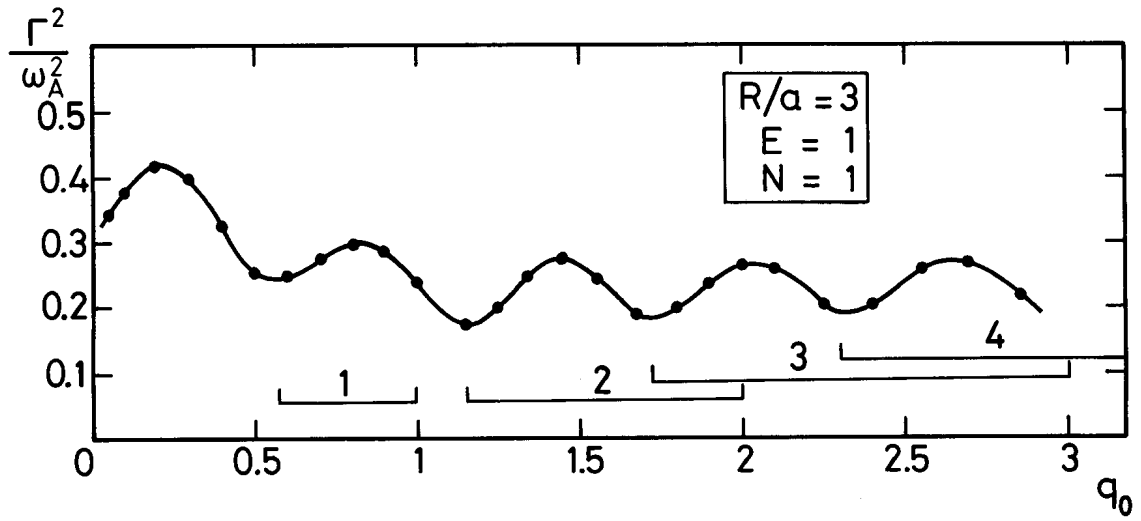


Figure 4.9.

The square of the normalized growth rate Γ^2 of kink modes versus q_0 for $n=1$ and 2. An infinite vacuum region surrounds the plasma (no shell).

a very small component of toroidal displacement in contrast to the internal modes. The first peak in the growthrate, starting from the left, corresponds to a global $m=1$ mode with no singular surface within the plasma. This is the same as in a straight circular geometry.

The second peak corresponds to a mode which is $m=1$ inside the plasma and $m=2$ on the outside. The $nq = 1$ singular surface lies within the plasma so that this mode can be considered as a coupling between an internal kink $m = 1$ and an external kink $m = 2$, both of which exist in a straight cylinder but are decoupled. This mode is presented in Fig. 4.10 for $q_0 = 0.45$ and $n = 2$. The arrows represent the displacement ξ projected on the meridian plan. Note that because of the difference between the X angular variable and the polar angle θ around the magnetic axis, the modes look as if there is $m=1$ on most of the area. Substituting the eigenvector into the potential energy, we have computed the contribution of each discretization cell to the plasma energy. These numbers are plotted on Fig. 4.11 in arbitrary units. The last column is the sum over the magnetic surface. We see that the destabilizing contribution comes from a region of bad curvature and that each magnetic surface is destabilizing, analogous to the straight system. Moving to higher q , the modes become more complicated. At the surface, m is equal to the integer value of nq at the plasma surface plus one. Inside, m decreases as one moves towards the center according to the local value of nq . The destabilization factor is always stronger near the surface.

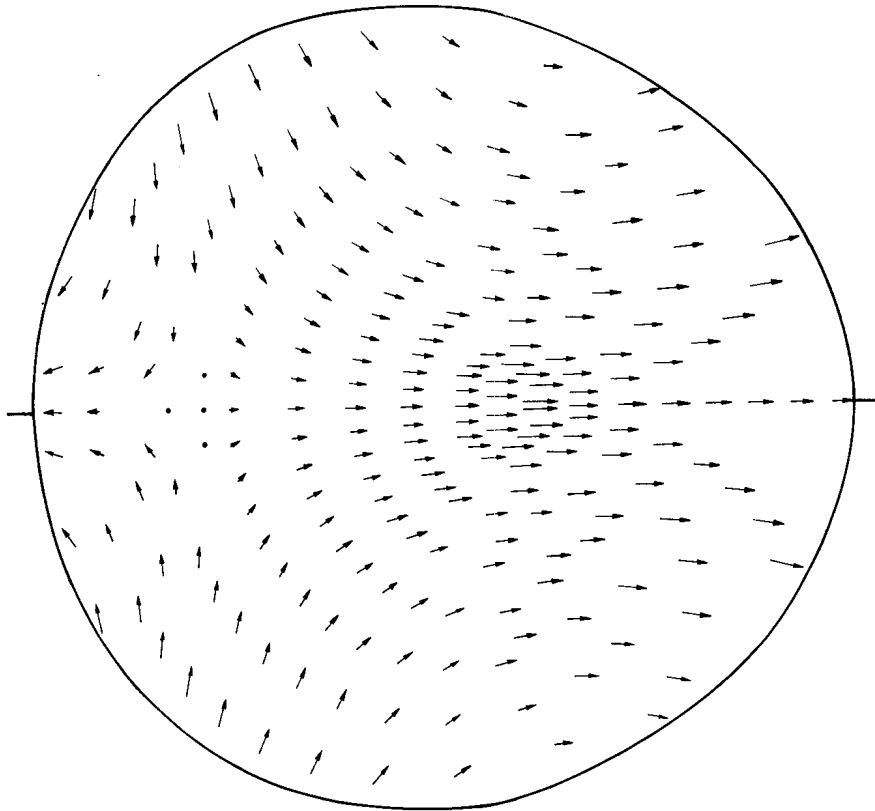


Fig. 4.10. Map showing the instantaneous displacement in a meridional plane chosen such that the mode is symmetrical about the mid-plane. The mode represented is a kink with $E = 1$, $q_0 = 0.45$ and $n = 2$.

															χ		
- 0	- 1	- 1	- 0	- 0	- 0	- 0	- 0	- 0	- 0	- 0	- 0	- 0	- 0	- 0	- 0	- 0	
- 3	- 6	- 5	- 4	- 2	- 1	- 0	- 0	- 0	- 0	- 0	- 0	- 0	- 0	- 0	- 0	- 0	
- 8	- 16	- 13	- 9	- 5	- 2	- 1	- 0	- 0	- 0	- 0	- 0	- 0	- 1	- 2	- 2	- 2	
- 16	- 30	- 23	- 15	- 9	- 4	- 2	- 0	- 0	- 0	- 0	- 0	- 1	- 2	- 4	- 6	- 7	
- 27	- 49	- 37	- 23	- 13	- 6	- 3	- 1	- 0	- 0	- 0	- 0	- 3	- 5	- 8	- 11	- 13	
- 42	- 76	- 54	- 32	- 17	- 9	- 5	- 3	- 1	- 1	- 1	- 1	- 5	- 10	- 14	- 17	- 19	
- 63	- 110	- 75	- 43	- 22	- 12	- 7	- 5	- 2	- 2	- 2	- 2	- 8	- 14	- 20	- 23	- 26	
- 90	- 153	- 99	- 54	- 29	- 16	- 11	- 8	- 3	- 3	- 3	- 3	- 11	- 19	- 25	- 29	- 32	
- 125	- 207	- 126	- 66	- 35	- 23	- 18	- 13	- 6	- 4	- 4	- 4	- 14	- 23	- 30	- 34	- 36	
- 172	- 274	- 155	- 79	- 44	- 32	- 27	- 20	- 10	- 5	- 5	- 5	- 16	- 36	- 32	- 35	- 37	
- 232	- 356	- 189	- 93	- 56	- 45	- 39	- 30	- 15	- 0	- 0	- 0	- 15	- 26	- 32	- 36	- 36	
- 310	- 453	- 223	- 109	- 72	- 62	- 56	- 43	- 26	- 4	- 4	- 4	- 12	- 23	- 29	- 31	- 32	
- 413	- 553	- 258	- 127	- 93	- 84	- 76	- 61	- 35	- 11	- 11	- 11	- 7	- 19	- 24	- 27	- 27	
- 548	- 702	- 290	- 149	- 118	- 106	- 102	- 77	- 45	- 15	- 15	- 15	- 5	- 19	- 24	- 26	- 27	
- 725	- 853	- 317	- 174	- 139	- 137	- 119	- 86	- 42	- 4	- 4	- 4	- 21	- 36	- 43	- 45	- 46	
- 969	- 998	- 342	- 185	- 155	- 144	- 115	- 62	- 1	- 1	- 1	- 1	- 43	- 92	- 101	- 111	- 114	
																	- 115

Fig. 4.11. Map showing the contribution of each discretization cell to the plasma potential energy. The displacement corresponds to the mode Fig. 4.10. The last column represents the average on each magnetic surface.

E = 2

A study of the elongation effect on the stability of a straight plasma device has been achieved recently {6,23}; modification due to toroidicity is now presented. The results for $n=1$ are shown in Figure 4.12. The curves have the same general behaviour as when $E=1$. There is a destabilization of the first peak $m=1$ and an apparent stabilization of the higher orders. Among the differences, the destabilizing contribution comes now from the region of strongest curvature, namely around the vertical axis, while it came from a wide region centered around the mid-plane on the outside of the torus for $E=1$. Figure 4.13 represents the poloidal displacement in the meridian plane $\psi = 0$ for $n=2$, $q_0 = 0.45$. The results presented show that the stability behaviour of the kink mode is not affected by elongation despite the higher $\bar{\beta}$ -value achieved. These results are a real encouragement for the design of non-circular tokamaks.

3.2 Unstable MHD Spectrum

We have up to now presented results concerning the most unstable external kink mode. In fact there are unstable modes with growth rates smaller than kink modes. We have computed next fastest modes in two cases $N=2$, $E=1$ and $N=1$, $E=2$, in order to try to correlate these modes with the rigid boundary case. The structure of these modes is important for transport phenomena and has increased interest in the presence of a conducting shell which acts specially on the most unstable surface mode. In a cylindrical discharge the free boundary spectrum is well behaved, with the fixed boundary values located between them.

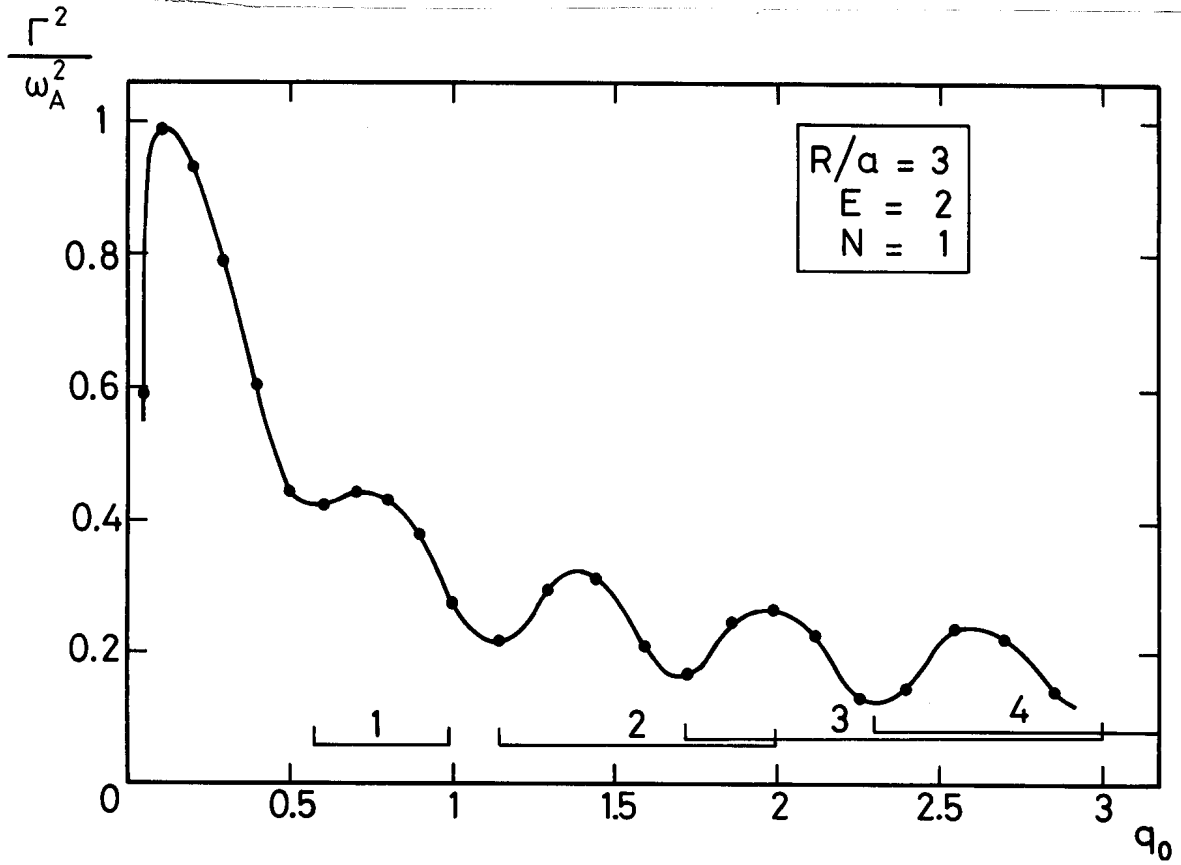


Figure 4.12. Plot of the normalized growth rate Γ^2 of the $E = 2$, $n = 1$ kink mode versus q_0 .

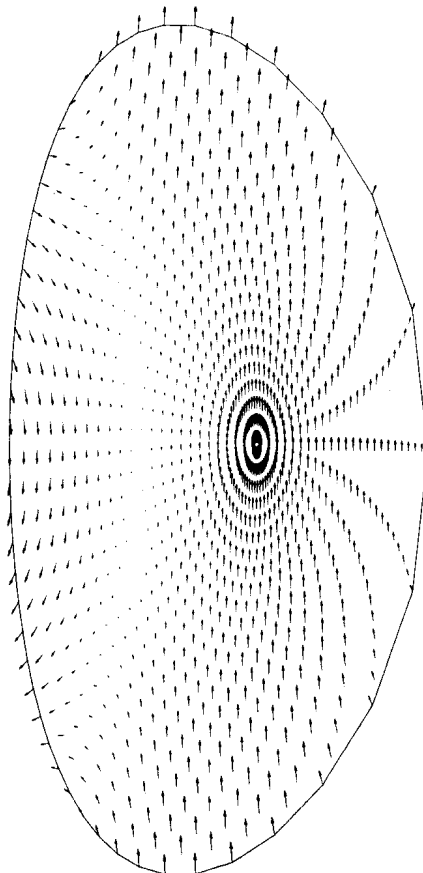
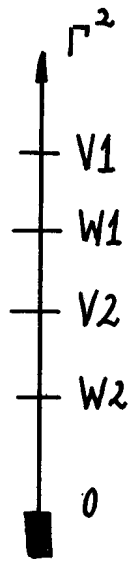


Figure 4.13. Map representing the instantaneous displacement of a kink mode with $E = 2$, $q_0 = 0.45$ and $n = 2$.



Schematically, as shown in Fig. 4.14, V1 refers to the most unstable mode in the free boundary case, V2 the second most unstable mode in the same conditions, etc. W1, W2 have the same signification for the fixed boundary calculation. This structure is completely lost in toroidal geometry.

Figure 4.14

Schematic plot of unstable modes in straight cylinder.

E = 1

Figure 4.15 represents the growth rates of V1, V2 and W1 as a function of q_0 . Segment lines have the same significance as in the previous case. Three facts have to be mentioned. If the ξ_ψ component of the second unstable mode oscillates once more in ψ than V1 does, the zero-line does not correspond to a magnetic surface. This fact destroys the usual ordering (V1, W1, ...). Secondly, the V2 curve drops when the quantity nq_s is an integer, exactly as V1. Nevertheless, the left wing of each maximum of V2 exhibits an $m+1$ component for ξ_ψ contrary to the corresponding V1 mode. In fact, this instability can be correlated to the next maxima of the V1 branch. V2 is a new branch of the kink induced by toroidicity, which splits the usual one branch kink of the cylinder case. Note that the same phenomenon occurs in a straight elliptical discharge {40}.

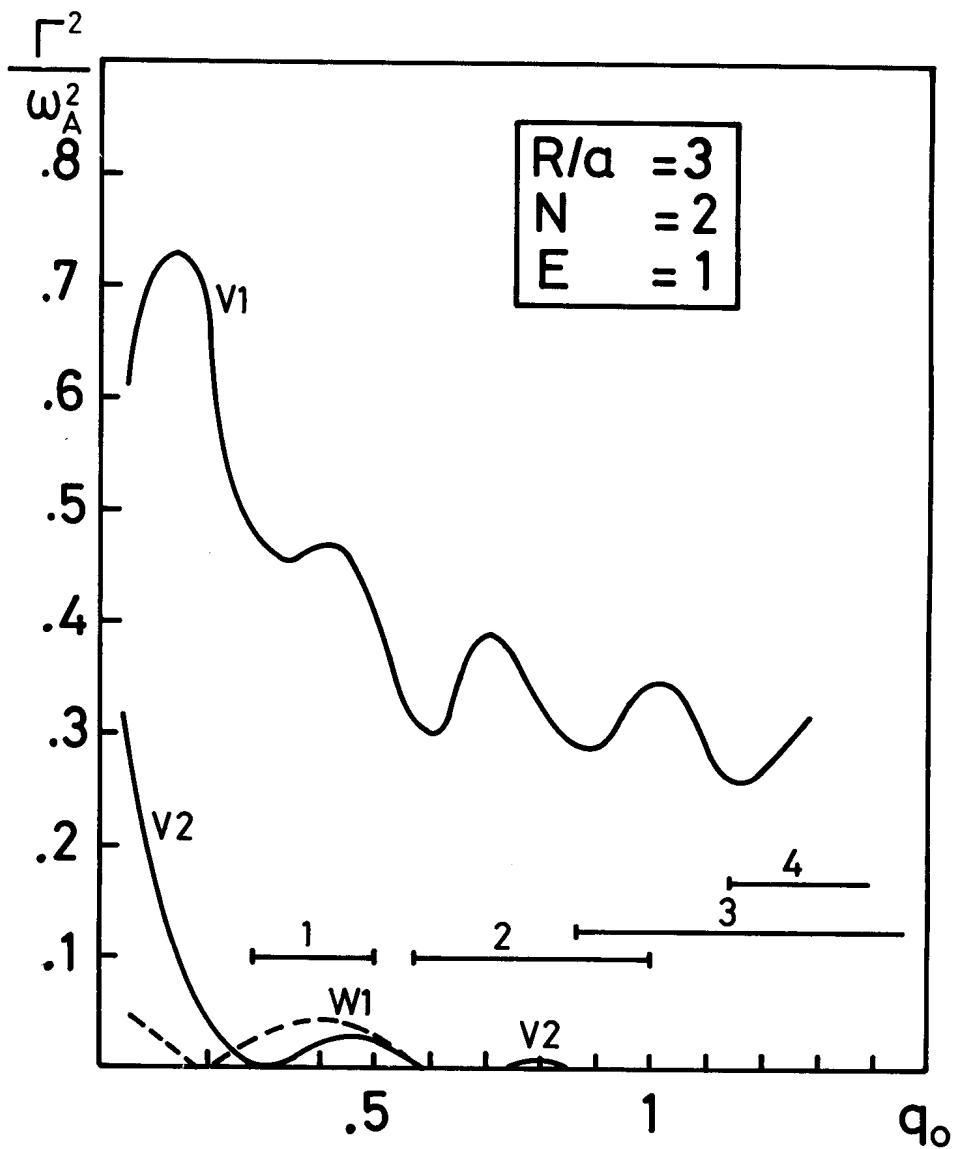


Figure 4.15

Plot of the normalized growth rate Γ^2
 for the first two unstable modes versus q_0 .
 (—) no shell, (----) fixed boundary

The second maximum of V2 for $q_0 \approx 0.8$ is due to this coupling. No unstable mode occurs for such q_0 -values in the fixed boundary case. Finally, the V2-curve disappears before the Mercier criterion limit, showing a mixed character between a kink and an internal mode. An example of such a mode is shown in Figure 4.16 for $q_0 = 0.45$. This

figure can be compared with Figure 4.10, which corresponds to the same parameters. The mode has an internal $m=1$ part which looks like an internal kink with an external $m=2$ kink-like behaviour in the outside region. The map of the potential energy shows an unstable core and an unstable region at the surface separated by a large neutral layer. This is plotted on Figure 4.17.

This coupling mode seems to be a precursor sign of a gross disruption in a Tokamak. An enlargement of the interesting part of Figure 4.16 is plotted in Figure 4.17. We note that V3 and W2 are very similar in shape and growthrate. The V3 branch is a real internal mode, the plasma surface having a small influence. The fact that only the V2 branch is affected by the coupling with surface modes is not a general feature. Let us look at Figure 4.18.

E = 2

Figure 4.19 corresponds to a toroidal wave number $n=1$. The V2-curve is similar to the previous case, disappearing for a q_0 -value less than the Mercier criterion limit. We remark that V3 is a surface mode, especially before a resonance at the plasma surface. Outside this region V3 and W2 are similar.

In this case, the ellipticity increases the splitting of the kink branch due to toroidicity and so acts at a lower level in the MHD spectrum.

These new aspects of the MHD spectrum of a small aspect ratio, non-circular Tokamak, must strongly affect its transport behaviour compared to standard Tokamaks. A theoretical and experimental study of this influence remains open.

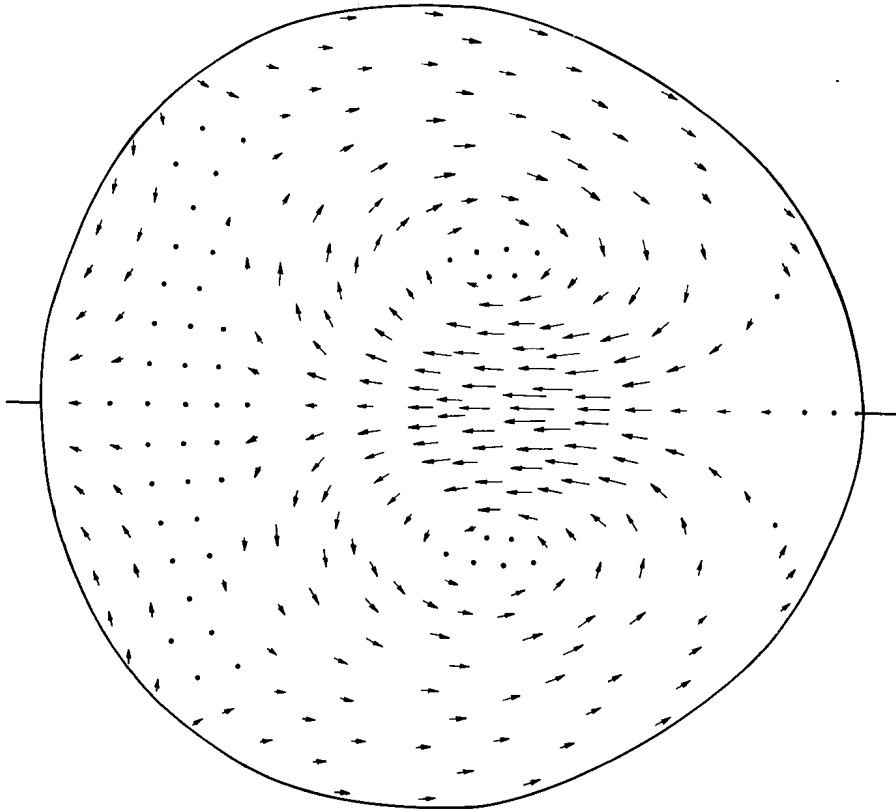


Figure 4.16. The instantaneous displacement, in a meridian plane, of the second most unstable mode for $E=1$, $q_0=0.45$ and $n=2$. The vertex in the central region corresponds to an internal kink displacement.

															x
- 48	- 94	- 86	- 76	- 66	- 59	- 56	- 57	- 59	- 61	- 63	- 63	- 61	- 60	- 29	- 62
-193	-364	-305	-232	-181	-151	-145	-155	-167	-167	-150	-120	- 88	- 63	- 27	-167
-364	-651	-501	-331	-210	-158	-163	-196	-219	-204	-145	- 60	22	80	50	-204
-514	-896	-599	-312	-133	- 76	-106	-165	-192	-146	- 33	109	236	321	175	-155
-603	-998	-561	-183	19	58	- 3	- 83	-102	- 21	134	310	459	553	292	- 48
-612	-950	-419	- 13	165	169	80	- 6	- 10	92	260	433	570	653	340	50
-547	-786	-247	103	221	186	84	5	14	112	255	389	491	551	285	74
-426	-562	-114	123	170	110	15	- 45	- 38	32	183	205	263	297	154	20
-270	-313	- 21	95	90	26	- 47	- 93	- 92	- 60	- 19	18	43	57	30	- 37
-107	- 80	52	81	53	1	- 48	- 79	- 88	- 80	- 68	- 57	- 50	- 47	- 23	- 36
15	74	90	73	39	1	- 31	- 51	- 57	- 54	- 50	- 46	- 45	- 44	- 22	- 7
60	98	60	24	- 15	- 53	- 77	- 80	- 65	- 49	- 36	- 28	- 25	- 23	- 11	- 14
- 11	- 40	- 83	-104	-166	-222	-235	-198	-139	- 87	- 53	- 31	- 20	- 15	- 6	- 92
-319	-436	-327	-374	-497	-593	-564	-426	-263	-133	- 47	4	34	48	26	-257

Figure 4.17. Map of the potential energy corresponding to the mode drawn on Figure 4.15. The two contributions of the internal kink and the surface mode ($m = 2$) are evident.

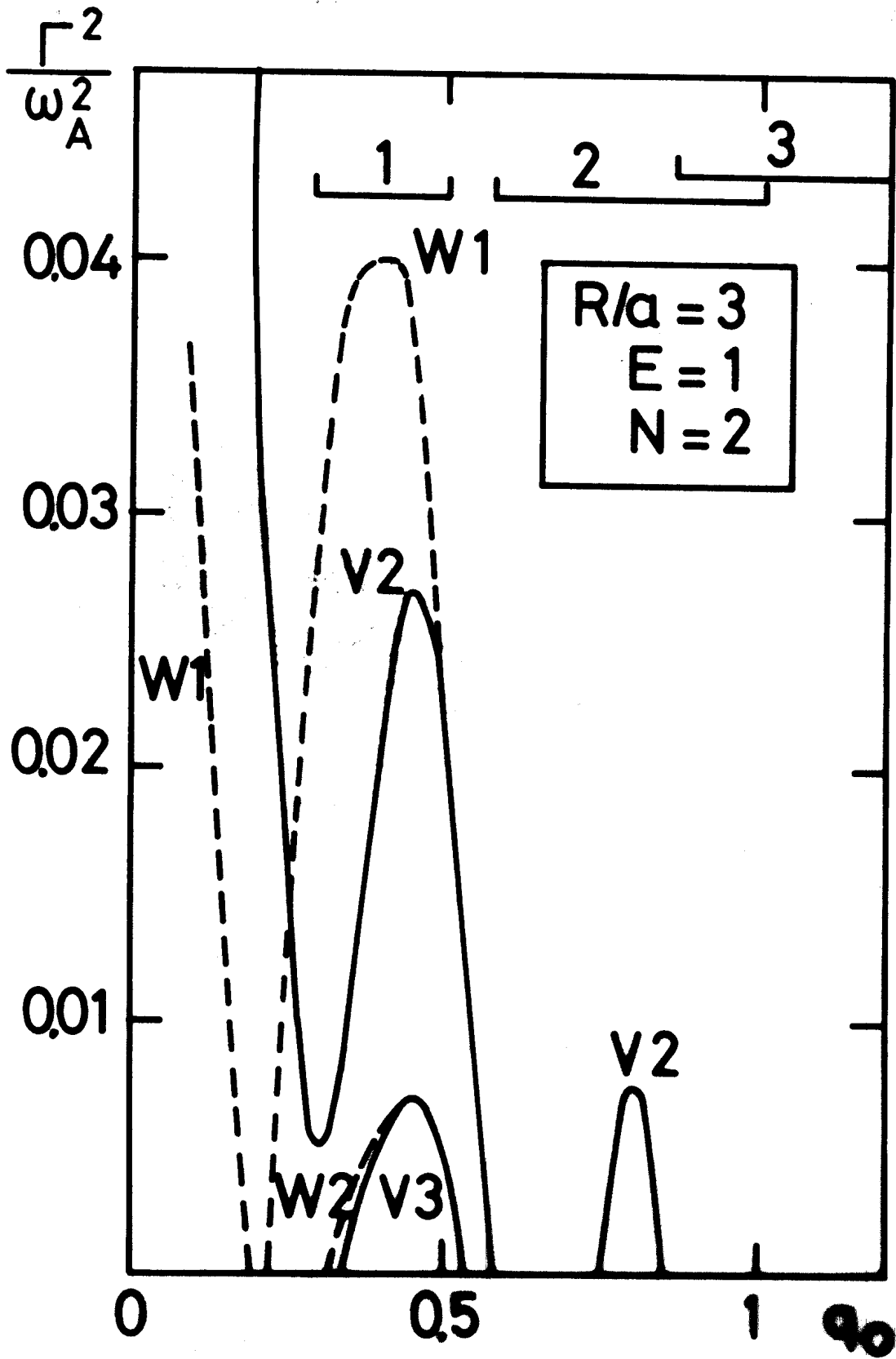


Figure 4.18

Plot of the normalized growth rate Γ^2 of the three most unstable modes versus q_0 . (—) no shell, (----) fixed boundary.

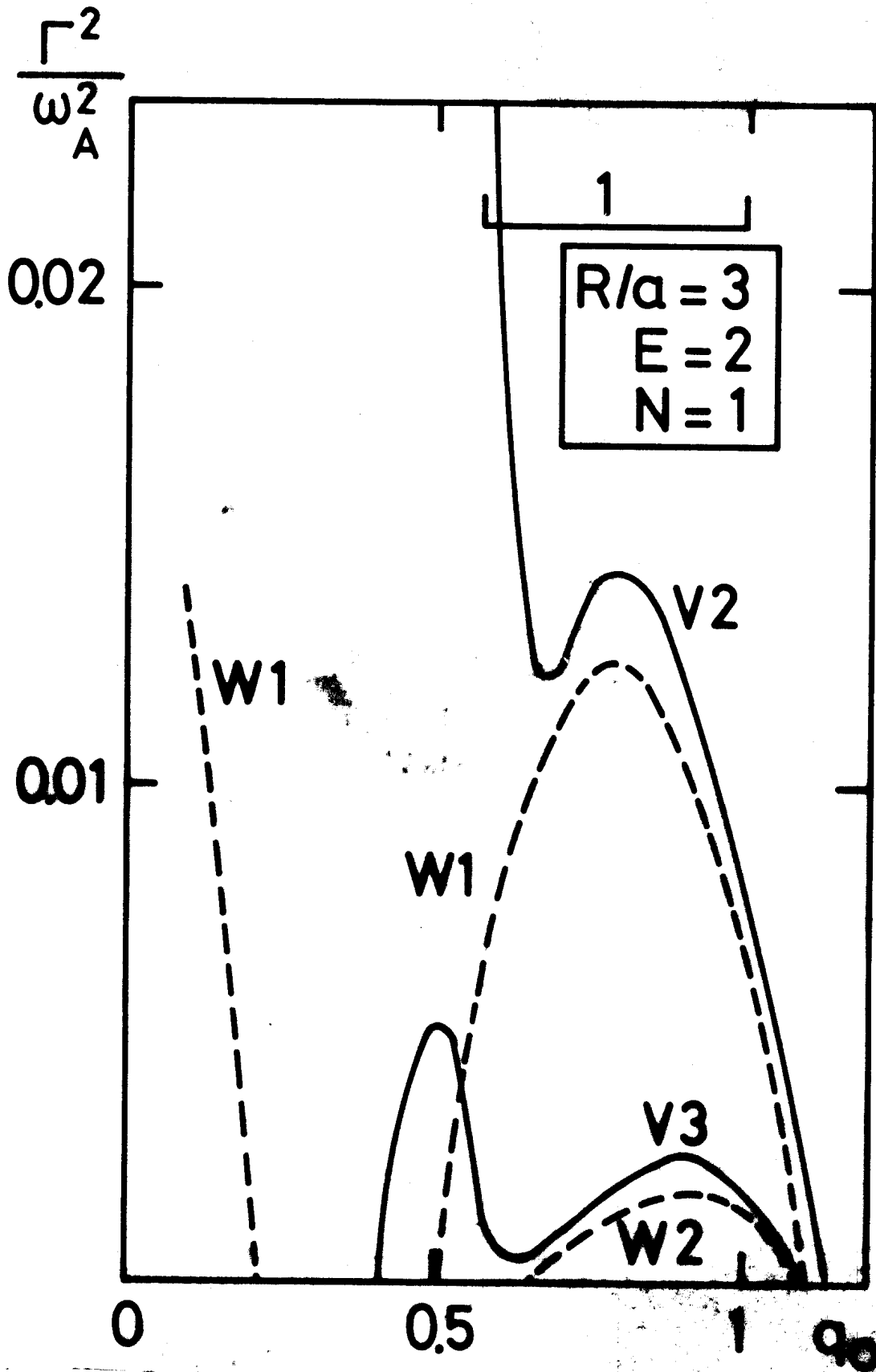


Figure 4.19. Plot of the normalized growth rate Γ^2 of the three most unstable modes versus q_0 .

(—) infinite vacuum, no shell (-----) fixed boundary

The simple Solovév equilibrium allows us to reach a very high beta value with an advantageous behaviour with respect to internal modes (Mercier limit) and to axisymmetric modes (wall stabilization).

These nice features are balanced by a strong kink instability which destroys the discharges. A possible way of stabilization is to put a conducting shell close to the plasma surface. Let us look at this effect.

3.3 Wall Stabilization of a Kink Mode

The definition of the shell is similar to that used in the axisymmetric study (IV.1). In Figure 4.20 the growth rate of the most unstable mode is plotted versus q_0 for different shell positions. The parameters are $E=1$ and $n=1$. Analytical calculations on the wall stabilization of a kink mode are given in Ref. [3]. If the $m=1$ peak is strongly affected by the shell position (Λ), the other maxima are equally affected by this stabilizing effect ($\Lambda = 1.414$). On the $\Lambda = 1.155$ curve the effect of the unstable fixed boundary mode is clearly visible for q_0 around 0.4. The internal modes fix the q_0 value close to 1; for such a value we have always a strong surface instability even for a shell very close to the plasma surface $\Lambda = 1.1$. For higher q_0 , the curves $\Lambda = \infty$ and $\Lambda = 1.414$ are parallel; the difference corresponds to the stabilization of the $m=1$ displacement, common to all modes, due to toroidal coupling. This is not so in a cylindrical case where a pure $m = 2, 3, \dots$ mode can exist.

Generally, a conducting shell, at a reasonable distance from the plasma surface, cannot stabilize kink instabilities ($n \neq 0$). Nevertheless, with an appropriate active shaping of the q -profile and a wall close to the plasma surface high beta ($\geq 10\%$) equilibria are possible.

In fact, all experimental measurements of the toroidal current density profiles [41] show a peaked shape different from the linear function in r used in the Solovév equilibria. Moreover, for $q_s > 3$, kink instability does not occur. We now want to look at the influence of the current peaking on the MHD stability. The price for peaking is a loss in $\bar{\beta}$.

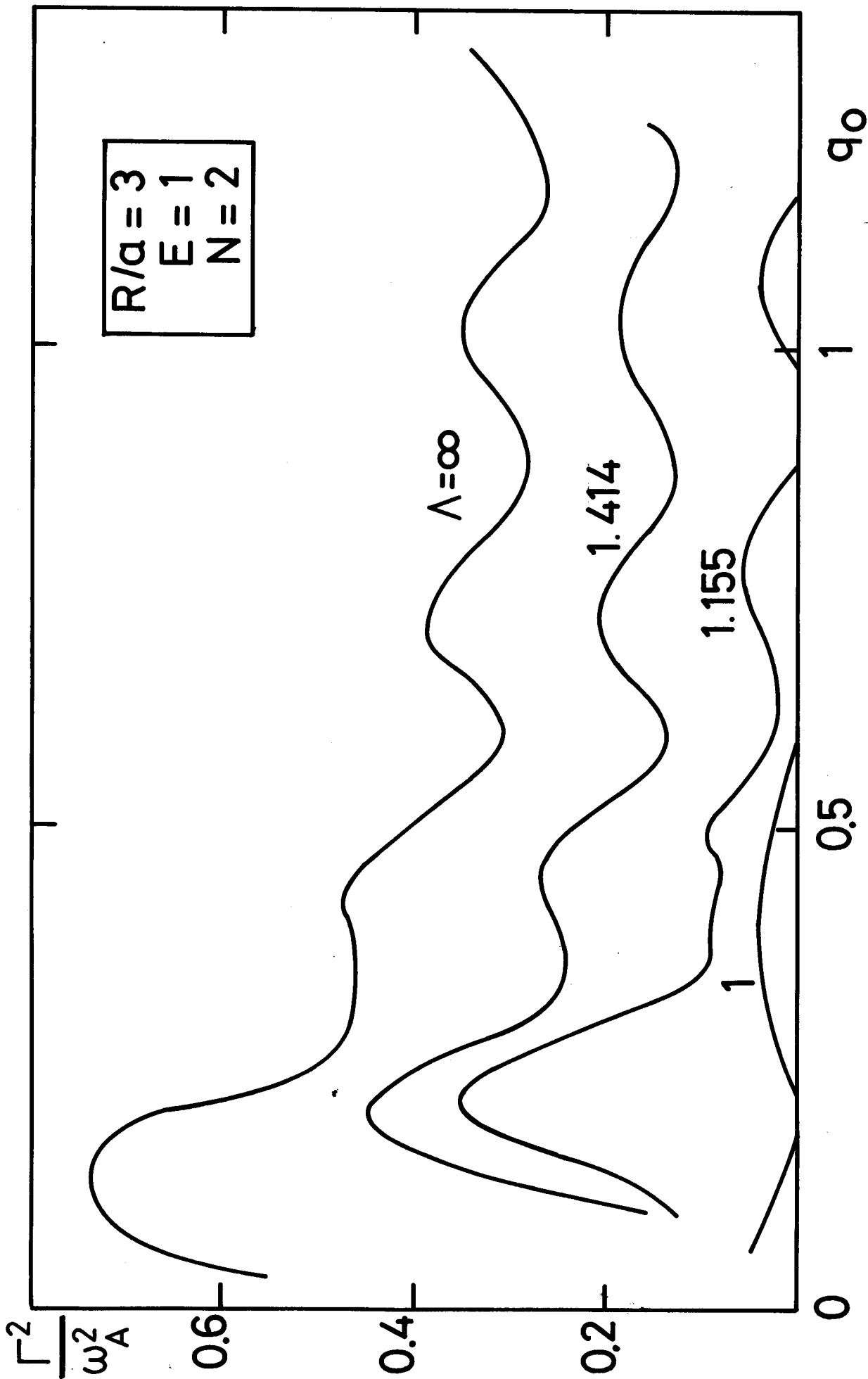


Figure 4.20. Wall Stabilization. Plot of the normalized growth rate Γ^2 of the most unstable mode versus q_0 . Four different shell positions (Λ) are represented.

V MHD STABILITY OF SMALL ASPECT RATIO EQUILIBRIUM WITH PEAKED

CURRENT DISTRIBUTION

The present Tokamak experiments show very good stability properties even when there is no conducting wall to act on the plasma. These observations violate the results presented in Chapter IV. In fact through a thermal instability the toroidal current peaks on the magnetic axis {41}. J. Wesson has shown that in a straight circular system current peaking eliminates the external kink {4}, leaving presumably the internal kink and the Mercier modes as the most dangerous. This peaking phenomenon leads to a loss of $\bar{\beta}$ with respect to the flat current profile case, or equivalently limits the toroidal current which can flow in the device.

In the first part of this chapter, we investigate numerically this problem for a class of toroidal equilibria. The evaluation of the most unstable mode is obtained as a function of q at the plasma surface, for a fixed value of q on axis. To explain the results consistently, fixed boundary modes are also investigated. We only look at the $n=1$ modes, assuming they will be the last ones to be stabilized just as in the straight case. The different modes which fix the stability limit are defined. Different values of the poloidal beta β_p and the elongation E are presented.

One of the main objectives of the present Tokamak fusion programs is to show the possibility of increasing the maximum $\bar{\beta}$ -value. The FCT {42,43} concept relies on an increase in β_p ; another possibility consists in changing the shape of the plasma. The second part of this chapter is related to these problems and presents an optimization of the average $\bar{\beta}$ with respect to the profile characteristic (q_s/q_0).

We will now define the conditions of the calculations : equilibrium choice and free parameters.

1. Equilibrium

An equilibrium is characterized by the shape of the plasma surface and by the derivatives of the pressure $p(\Psi)$ and of the poloidal current function $T(\Psi)$ {3,11}.

The surface is given by the equation

$$\frac{r^2 z^2}{E^2} + \frac{(r^2 - R_0^2)^2}{4} = \frac{R_0^4}{(a/R_0)^2}$$

where R_0 is a length which corresponds to the radius of the magnetic axis when the current is flat, E is a measure of the elongation of the plasma cross section, and the parameter R_0/a is the aspect ratio.

This shape is the same as that encountered in the Solovév equilibrium study. It corresponds to an aspect ratio of 3, and exhibits a D-shape form. For $p'(\Psi)$ and $TT'(\Psi)$ we take

$$p'(\Psi) = p'_0 \{ \exp(-\nu \Psi^2) - 1 \}$$

$$TT'(\Psi) = R_0^2 \left(\frac{1}{\beta_J} - 1 \right) p'(\Psi),$$

where ν characterizes the width of the current distribution and β_J corresponds to the poloidal beta for large aspect ratio. The choices of p'_0 and β_J fix the safety factor on axis q_0 . The flux Ψ is normalized such that it vanishes at the plasma surface. An equilibrium is completely defined by the safety factor on axis q_0 , its value on the surface q_s , β_p and E . R_0 acts only as a normalizing factor for the eigenfrequency ω . The density current has zero value and slope at

the limiter according to Wesson's prescription {4}. The equilibrium for each case is computed with the ORNL code {29} with a 140x70 mesh in the r and z direction, respectively. The usual Oak Ridge scaling {44} is applied such that one equilibrium calculation can be used for many values of q_0 . If the numbers (Ψ , p, TT') correspond to an equilibrium, ($s\Psi$, s p, s TT') correspond to a new one, where s is the scaling factor.

The stability analysis is performed by the spectral code ERATO {11}. We shall now present a detailed study of the case with $E=1$ and $\beta_p = 1$.

2. Effect of Peaking the Current Distribution

$$\underline{E = 1, \beta_p = 1}$$

The results for this case are shown on Fig. (5.1). The square of the growth rate Γ^2 of the most unstable mode is plotted versus the safety factor at the surface q_s , for two values of q_0 . The normalizing frequency ω_T is given by $\omega_T = T^2(\Psi_0)/R_0\rho_0$. The solid lines are results obtained with an infinite vacuum region surrounding the plasma. The dashed lines are obtained with a conducting shell tight against the plasma surface.

2.1 Kink Limit

For $q_s/q_0 < 2.5$ the mode is an external kink. Each magnetic surface gives a negative contribution to the potential energy, except near the plasma surface where the toroidal current and its derivative vanish. In Fig. 5.2, we have plotted the instantaneous displacement of the plasma, projected in the meridian plan. Parameters are $q_0 = 0.9$ and $q_s = 1.84$. As in the flat current case, we see clearly that the mode is mainly $m=1$

around the center, becoming $m=2$ at the edge, always according to the integer part of nq . The toroidal component ξ_φ is ten times smaller than the poloidal displacement. Moreover, the mode exhibits no azimuthal or radial localization. Maps of the potential and kinetic energies corresponding to this mode are given in Fig. 5.3. The negative contributions come from regions of bad curvature, but the average on each magnetic surface is always destabilizing, except near the surface. The kinetic energy increases monotonically from the center to the surface. All these features characterize a kink mode. Extrapolating the sharp drop in growth rate of the kink (dotted line) we can define the point where it cuts the q axis as the stability limit for the kink (q_k). It corresponds to $q_s/q_0 = 2.8$. In the straight case it is $q_s/q_0 = 2.0$ [4]. We can note that our value of $q_s/q_0 = 2.8$ corresponds to the straight calculation $q_s/q_0 = 2.0$ shifted by the toroidal shear associated with the Solovév equilibrium, $q_s/q_0 = 1.74$. We see that this shift degrades the increase in $\bar{\beta}$ obtained by a smaller aspect ratio. The question of an optimized aspect ratio is still open. In Fig. 5.4, we have plotted the growth rate Γ^2 of the most unstable mode versus q_0 for a fixed value of $q_s/q_0 = 2.6$. This value is smaller than the kink limit. The equilibrium is unstable for all values of q_0 , independent of the value of $\bar{\beta}$. The curve exhibits a resonant pattern with minima corresponding to the presence of a singular surface at the plasma boundary, a feature characteristic of a kink behaviour. For an equilibrium with a value q_s/q_0 greater than q_k , there is a q_0 value which corresponds to a limit for MHD stability. Such a case, with $q_s/q_0 = 3.6$, is plotted in Fig. 5.5. As the peaking increases, the mode changes its character, becoming progressively internal.

2.2 Internal Mode Limit

As q_0 decreases towards 1, the stability limit moves up from the kink limit, and for $q_0 < 1$ the instability remains for all q_s . The deviation from the kink limit is explained by looking at the fixed boundary

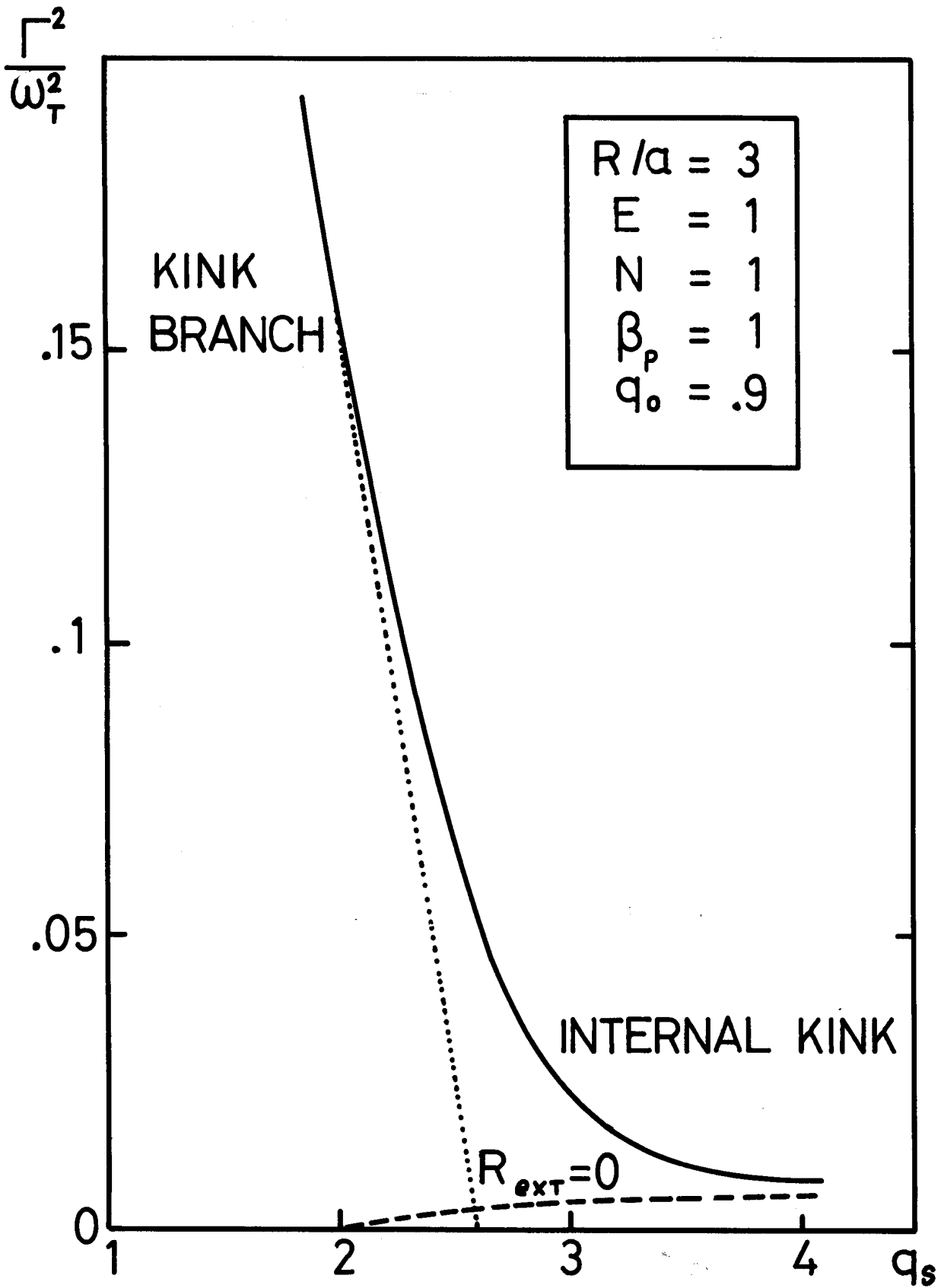


Figure 5.1. Dependence of the normalized growth rate Γ^2/ω_T^2 of the most unstable $n=1$ mode on q_s for two values of q_0 . No shell (—). Shell against the plasma (-----).

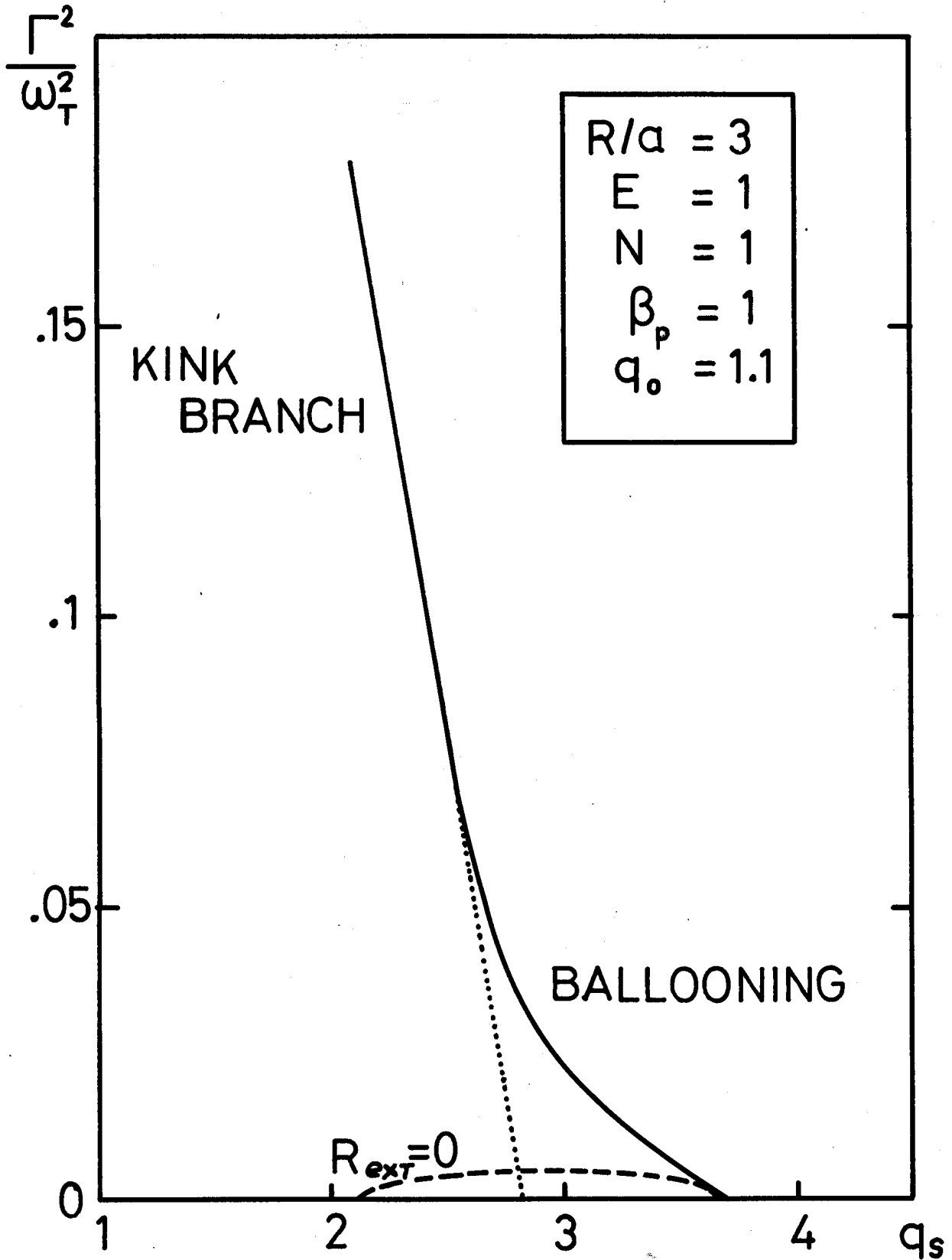


Figure 5.1. Dependence of the normalized growth rate Γ^2/ω_T^2 of the most unstable $n=1$ mode on q_s for two values of q_0 . No shell (—). Shell against the plasma (-----).

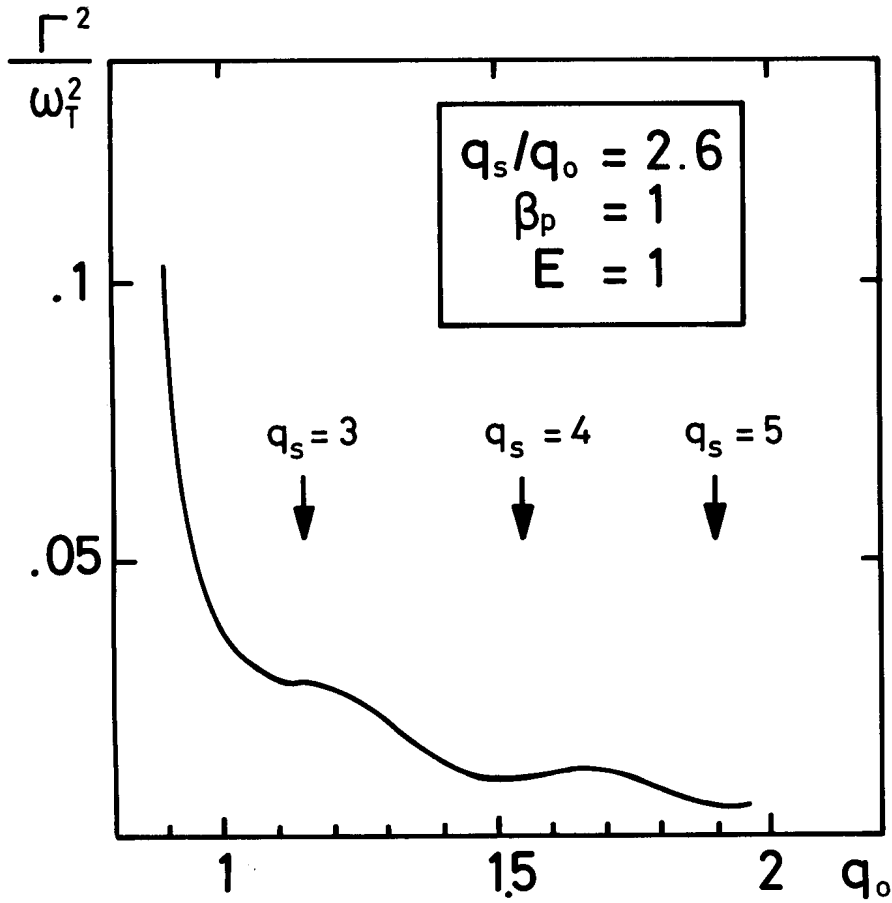


Fig. 5.4. Plot of the normalized growth rate Γ^2/ω_T^2 of the most unstable $n = 1$ mode versus q_0 . The peaking is insufficient to stabilize the kink. $R/a = 3$.

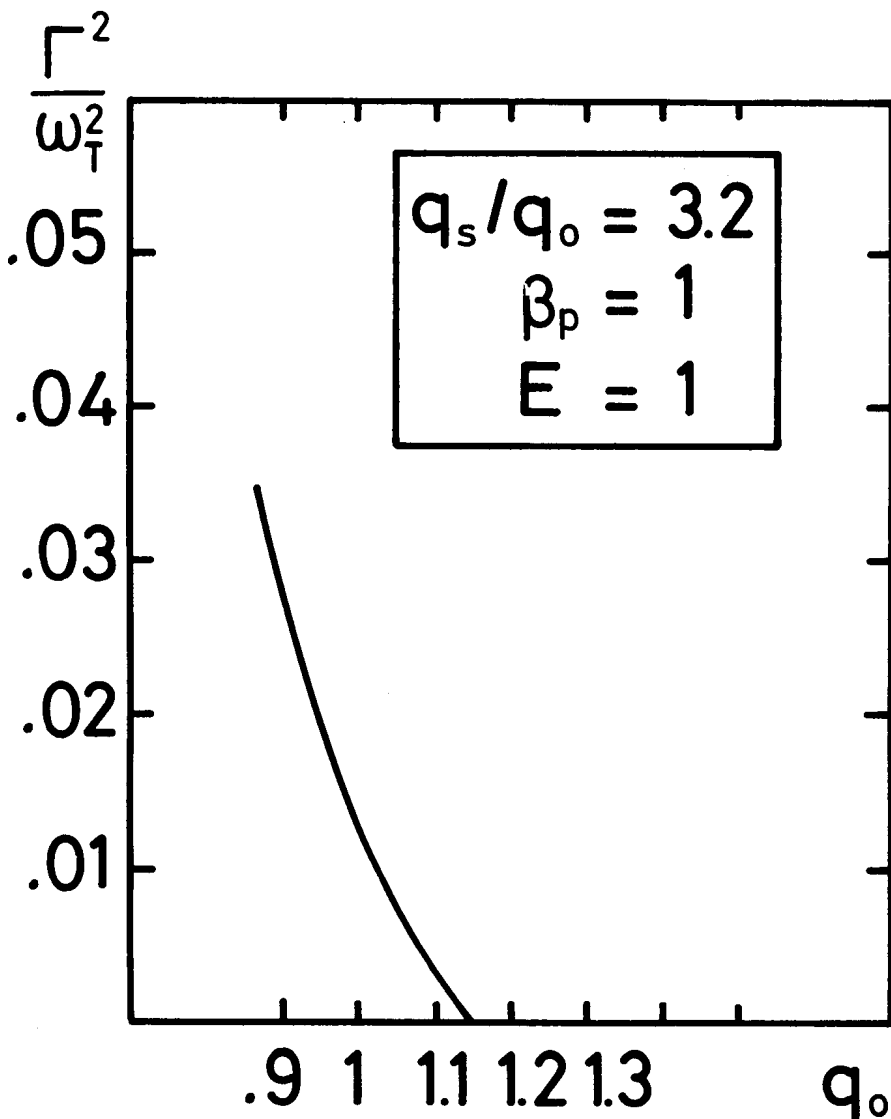


Fig. 5.5. Plot of the normalized growth rate Γ^2/ω_T^2 of the most unstable $n = 1$ mode versus q_0 . $q_s/q_0 = 3.2$ is sufficient to avoid the kink instability. $R/a = 3$.

calculations. It is surprising that peaking destabilizes first the internal mode. This fact can be attributed to the loss of triangularization around the magnetic axis through peaking [45]. As a remark, the Solovév equilibrium has no $n=1$ internal instabilities. For $q_0 < 1$ the residual mode is an internal kink. Such a mode structure is represented in Figure 5.6 and the corresponding map of the potential energy in Figure 5.7. Parameters are $q_0 = 0.9$ and $q_s/q_0 = 3.8$. The destabilizing part of the potential energy comes from the region inside the $q=1$ surface and from plasma volume near the $q=2$ surface. This mode can be construed as a coupling between an $m=1$ internal mode and an $m=2$ mode. Comparison with the V2 mode of Figure 4.6 shows evident analogy. The kinetic energy is concentrated inside the $q=1$ surface. Note that the toroidal component ξ_ψ of this mode is comparable with the poloidal component, characteristic of internal modes. The internal mode is another limitation for MHD stability.

2.3 Ballooning Limit

For $q_0 \approx 1$ and $q_s/q_0 > 2.8$ the remaining unstable modes are called ballooning, because they correspond to q_0 larger than the Mercier limit. In Figure 5.8 we show such a mode, projected in the poloidal plane. The parameters are $q_0 = 1.1$ and $q_s = 3.6$. Figure 5.9 represents the corresponding map of the potential energy. The negative contribution comes from the region between the $q=1$ and $q=2$ surfaces, contrary to the $q_0 < 1$ situation. As they correspond to q_0 greater than the Mercier limit, these displacements are called "ballooning modes". The toroidal component is comparable to the poloidal one, the normal displacement being the smallest. Ballooning modes strongly depend on β_p and $\bar{\beta}$ and are a major factor in determining the MHD stability domain.

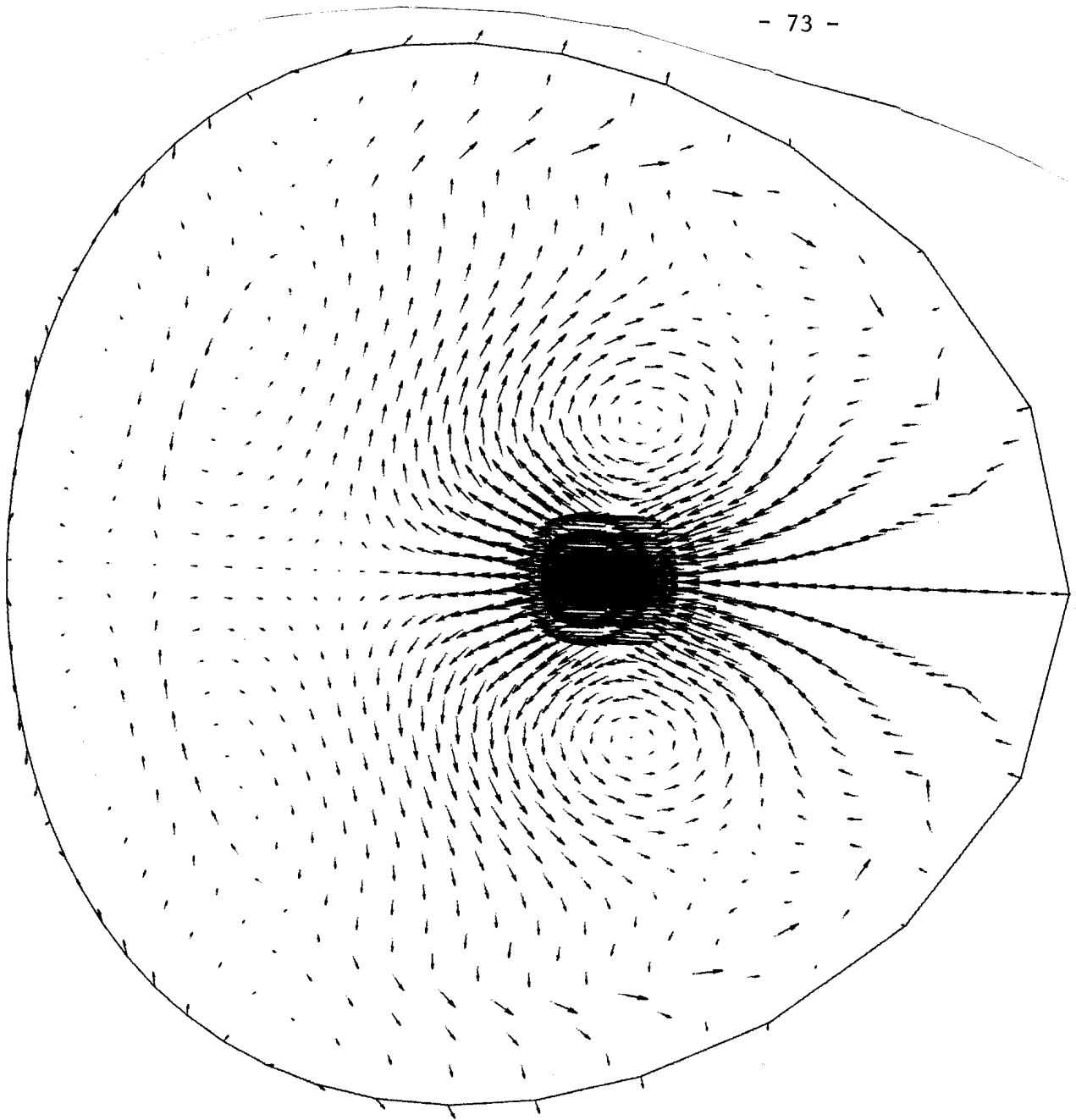


Fig. 5.6 Internal mode. Most unstable mode for $q_0=0.9$ and $q_s=3.8$. $R/a=3$, $E=1$, $\beta_p=1$, $n=1$.

- 83	-163	-150	-135	-123	-114	-108	-100	- 88	- 71	- 53	- 40	- 18	- 99
-181	-335	-297	-250	-212	-190	-172	-152	-117	- 78	- 34	- 4	5	-161
-360	-489	-315	-189	-106	- 37	39	39	128	219	319	360	171	- 53
-318	-796	-520	-287	-158	- 46	43	142	236	348	417	483	248	- 15
-497	-791	-537	-286	- 98	18	117	220	329	407	475	501	273	11
-507	-861	-520	-246	- 80	23	111	196	272	326	355	372	186	30
-518	-830	-472	-224	- 98	- 24	38	91	128	149	157	158	75	-109
-475	-722	-363	-160	- 73	- 21	22	54	70	73	69	63	31	-114
-404	-546	-200	- 46	7	45	75	95	99	94	84	76	37	- 46
-281	-266	20	106	133	159	178	181	170	151	135	123	59	69
-172	- 60	154	195	217	237	244	235	213	187	165	150	71	147
- 17	171	210	175	154	138	116	89	63	45	35	31	15	98
104	327	257	212	193	178	154	124	97	79	72	70	34	154
134	316	214	163	127	98	72	53	44	42	41	41	20	110

Fig. 5.7 Potential energy per cell associated with the mode plotted in Fig. 5.6.

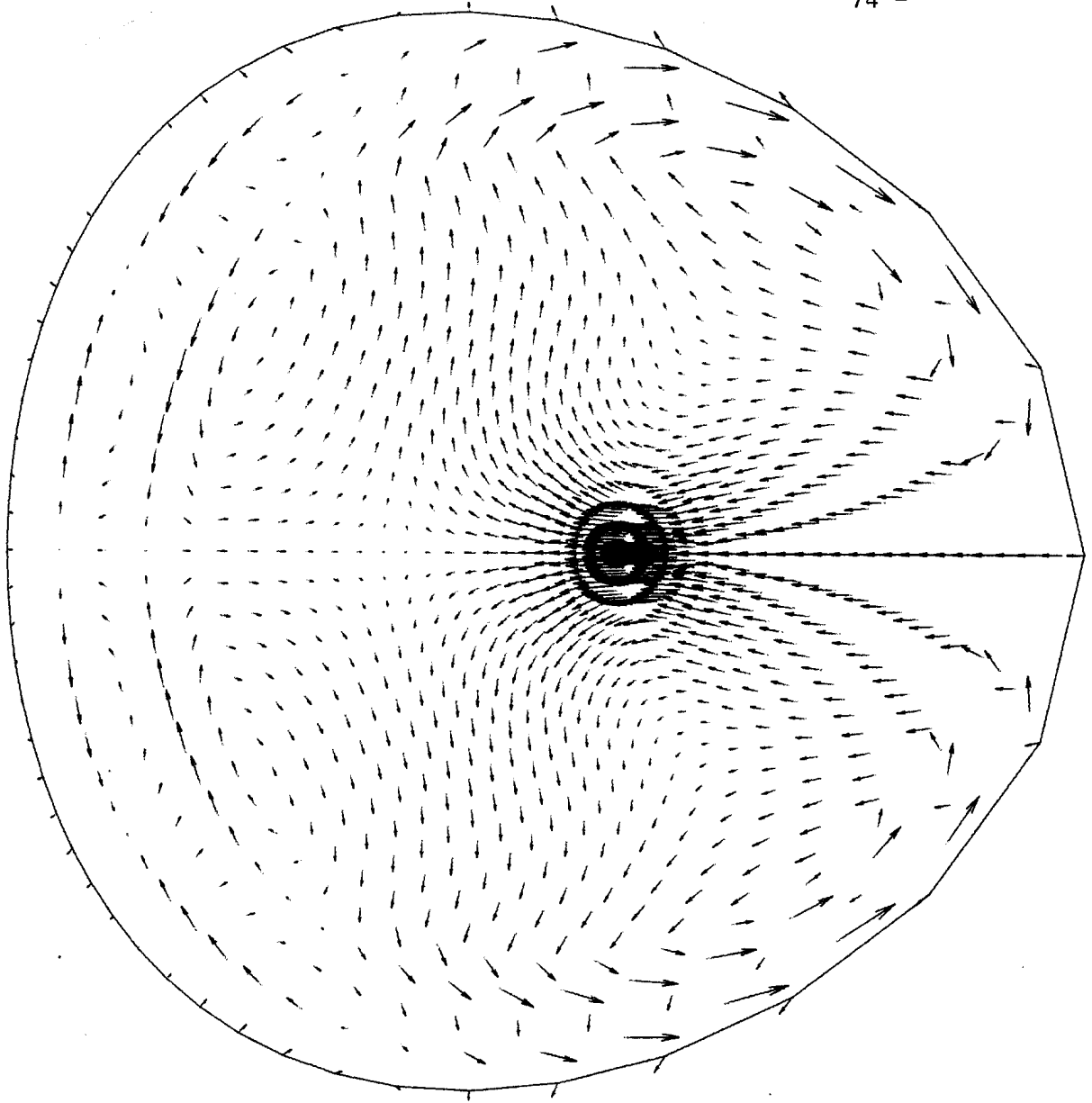


Fig. 5.8 Ballooning. Most unstable mode for $q_0=1.1$, $q_s=3.6$. $R/a=3$, $E=1$, $\beta_p=1$, $n=1$.

1	12	12	19	26	30	34	38	42	47	52	53	29	31
- 55	- 87	- 62	- 37	- 5	14	33	52	72	91	106	107	72	23
- 93	-225	-144	- 78	- 33	1	30	59	89	115	130	150	66	4
-210	-326	-234	-136	- 71	- 25	12	49	84	110	124	136	66	- 33
-273	-484	-317	-187	-107	- 56	- 12	29	62	82	93	98	47	- 82
-370	-605	-381	-219	-132	- 76	- 29	12	40	54	59	58	29	-124
-450	-716	-409	-223	-133	- 76	- 27	12	36	44	44	41	19	-146
-528	-771	-378	-183	- 96	- 38	10	48	65	67	61	56	27	-132
-552	-697	-243	- 62	15	76	124	149	155	145	131	120	58	- 46
-509	-560	-108	49	124	188	232	248	241	222	202	188	91	48
-348	-251	99	194	253	297	317	308	281	249	222	204	98	153
-268	-145	90	118	127	128	116	92	65	44	31	23	10	34
-102	98	204	194	184	174	153	126	101	83	74	70	35	111
114	345	265	217	193	170	138	101	71	52	44	42	19	144
187	391	261	201	161	127	98	77	69	66	63	58	28	144

Fig. 5.9 Potential energy associated with the mode plots on Figure 5.8.

For each case characterized by a fixed value of q_0 , the stability limit in q_s corresponds to a maximum value for $\bar{\beta}$. For example, if $q_0 = 1.1$, the marginal point at $q_s = 3.8$ gives an average $\bar{\beta}$ limit of $\bar{\beta}_{\max} = 1.1\%$. In Figure 5.10, we have plotted the stability frontier in the $(q_s/q_0, q_0)$ plane. The three types of limiting modes are clearly represented. We shall now investigate the influence of β_p and E on these modes.

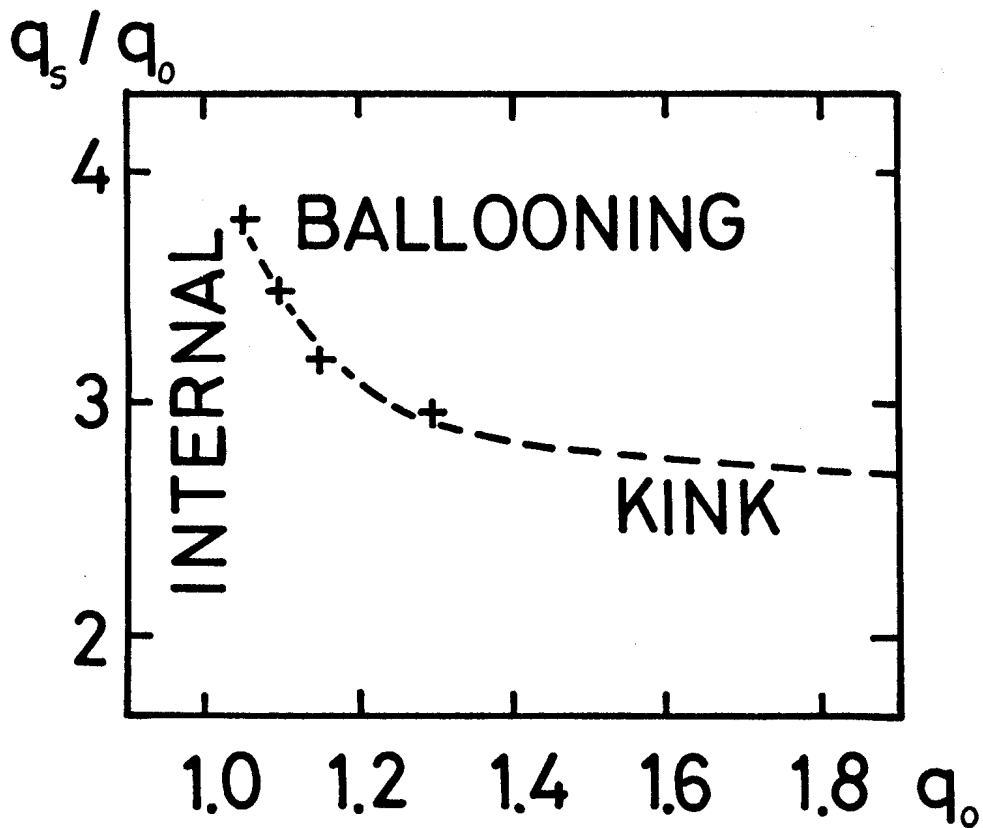


Figure 5.10

Plots of the minimum q_s/q_0 value for stability versus q_0 . The upper region corresponds to MHD stability.

3. Influence of β_p on the Maximum Average

The question of a critical equilibrium β_p , essential for progress in Tokamak research, is somewhat intricate. In particular, Mercier {19} found that β_p had to be limited by R/a in order to avoid the entrance of the separatrix within the plasma, i.e., the appearance of a second magnetic axis. Dory and Callen {29} have obtained higher β_p equilibria but they are characterized by a reverse current at the inner edge of the torus. Recent calculations {42, 43} have shown it to be possible to avoid this limit by the creation of a series of equilibria with a fixed q -profile (FCT) and arbitrary β_p . The problem of the stability of such equilibria has been investigated preliminarily. This shows a limiting value of β_p or $\bar{\beta}$ for a given q_s/q_0 value {15}. We can also obtain information on such FCT "transitions" by studying our "Maxwellian" equilibria for different values of β_p .

$$\beta_p = 2$$

Figure 5.11 represents the growth rate Γ^2 of the most unstable mode as a function of q_s for three different values of q_0 . We note a shift of the whole curve to higher q_s values compared to the $\beta_p = 1$ case. This fact corresponds to a loss in $\bar{\beta}$ with regard to the simple linear scaling $\bar{\beta} = \beta_p \cdot \bar{\beta}(\beta_p=1)$. The saturated behaviour of the dependance is clearer in Figure 5.14. The results shown can be interpreted with the same scheme as the preceding one ($\beta_p=1$). The difference between the kink limit and the ballooning one is enhanced. Ballooning modes are destabilized by an increase of β_p . For a given q_s/q_0 , an FCT transition can lead to a destabilization of the plasma (Figure 5.11). Nevertheless, stability is achieved for $q_0 = 1.25$ and $q_s = 5.7$ with a $\bar{\beta} = 1.3\%$, greater than $\bar{\beta} = 1.1\%$ corresponding to $\beta_p = 1$. We have shown that an optimization of $\bar{\beta}$ with respect to q_s/q_0 is a crucial point for the relevance of the FCT concept. The shift of stability to higher q_s values can be a crucial

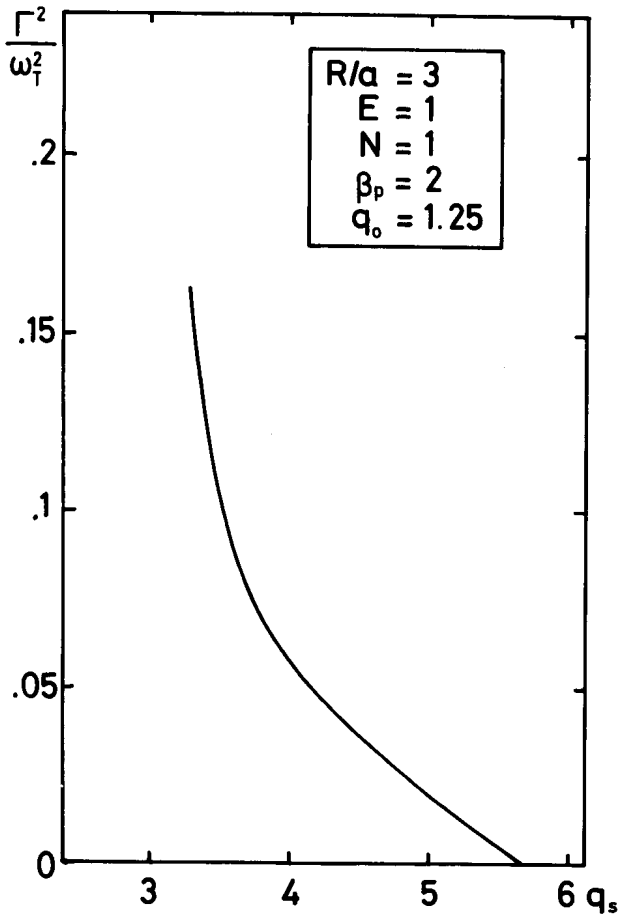
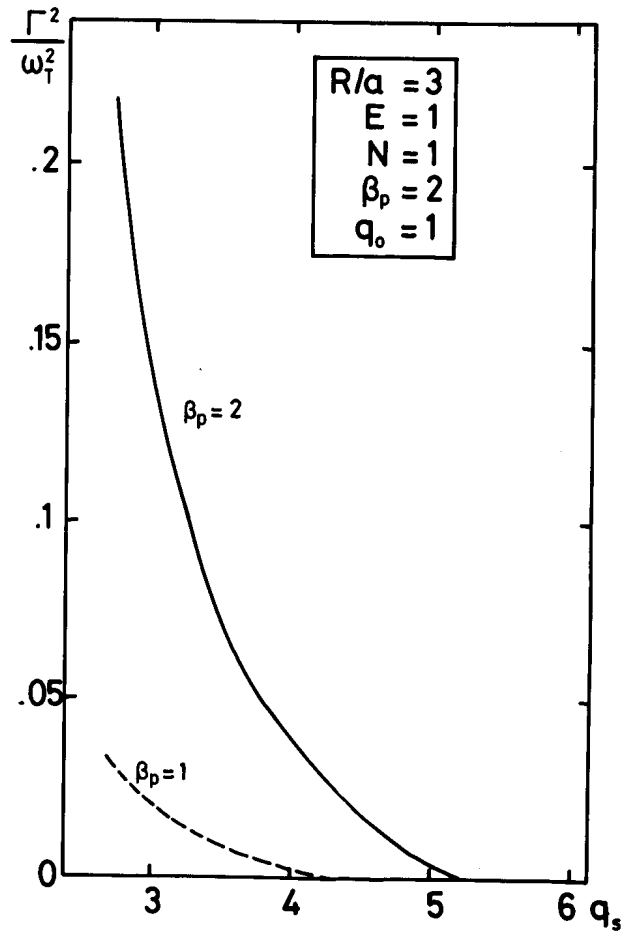
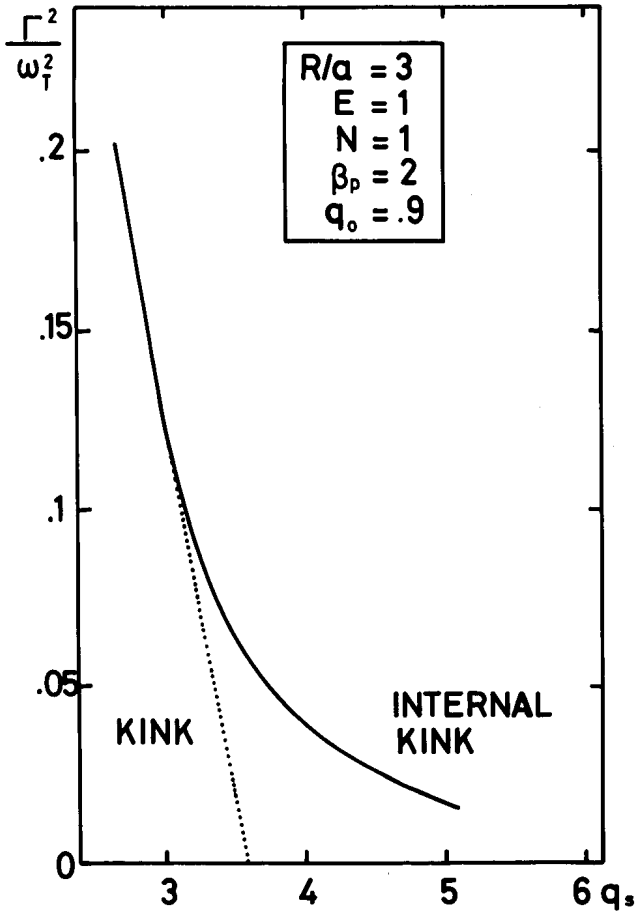


Figure 5.11. $\beta = 2$.

Plots of the normalized growth rate Γ^2/ω_T^2 of the most unstable $n = 1$ mode versus q_s , for three values of q_0 .

advantage for the design of a Tokamak. Stability, with a sufficient high $\bar{\beta}$ value, is achieved with smaller toroidal current, inducing a decrease of the E-coil current and less ohmic losses in its circuitry. The problem of a β_p limit has shifted from equilibrium to stability considerations.

4. Influence of the Elongation on the Maximum Average $\bar{\beta}$

Elongation is proposed as an efficient way to increase the total $\bar{\beta}$. Experiments performed in the Doublet II experiment [46] have shown this trend. We have computed the MHD stability of equilibria corresponding to $E=2$ and $\beta_p = 1$.

With peaking, the ellipticity around the magnetic axis decreases and the Mercier criterion limit remains close to 1 for peaked equilibria [16] as shown in Fig. 5.12.

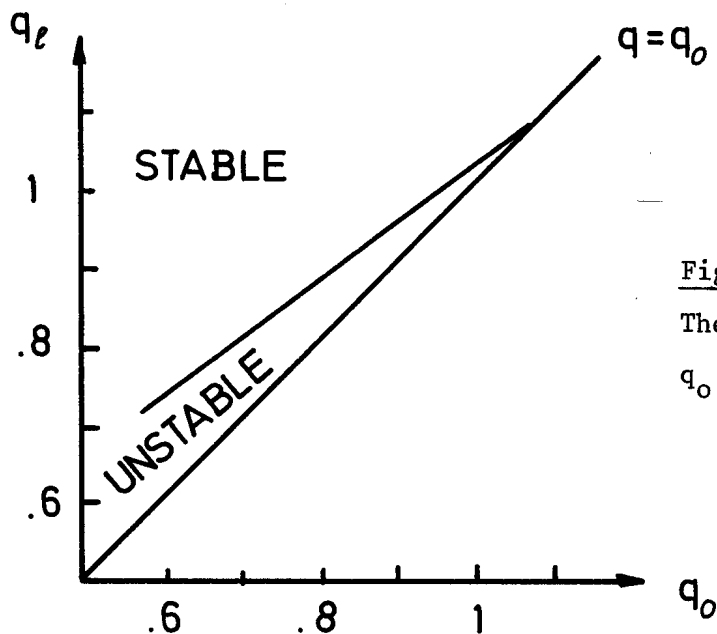


Figure 5.12. Mercier's criterion
The unstable region, limited by q_0 and q_l is plotted versus q_0 .

The internal mode limit is close to that obtained for $E=1$. We do not loose $\bar{\beta}$ with this limitation mechanism. In Figure 5.13, we have plotted the growth rate Γ^2 of the most unstable mode versus q_s for three different

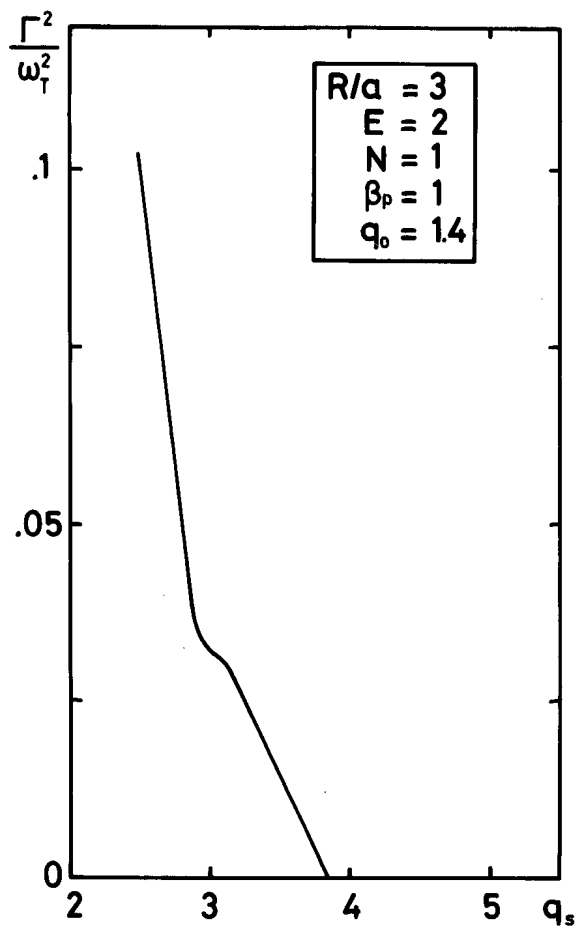
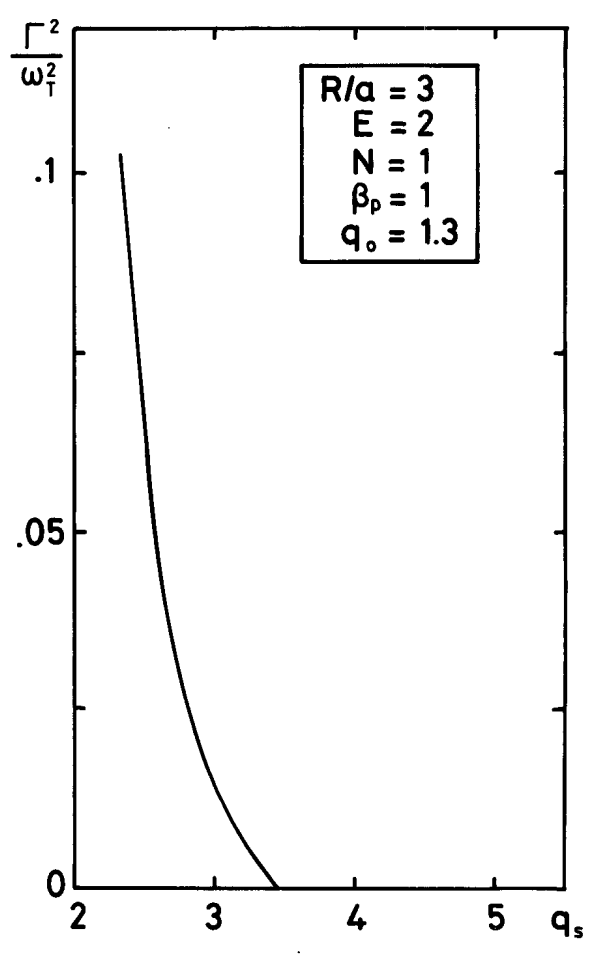
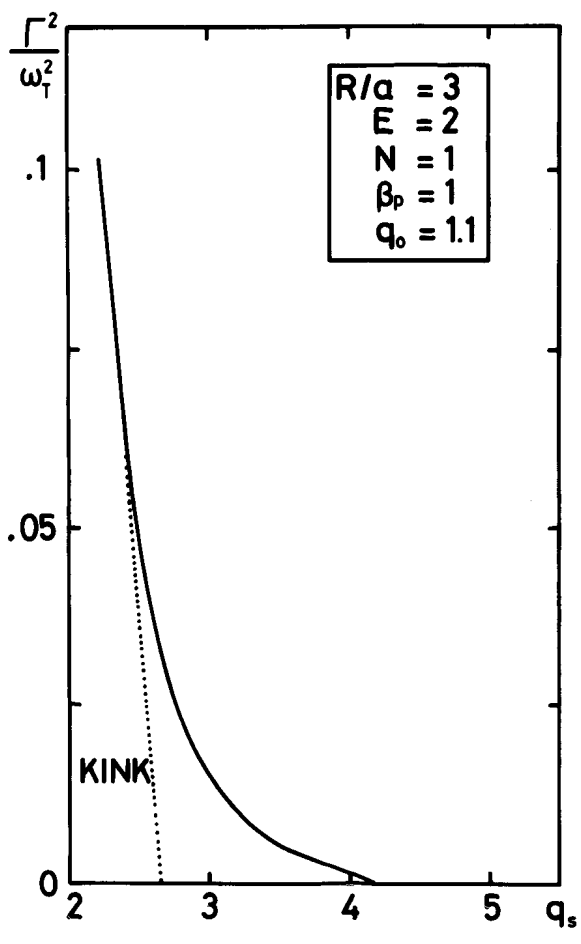


Figure 5.13. $E = 2$.
Plots of the normalized growth rate Γ^2/ω_T^2 of the most unstable $n = 1$ mode versus q_s , for three values of q_0 .

values of q_0 . The dotted line corresponds to the kink limit. We see that this value $q_s/q_0 \approx 2.8$ is not affected by the ellipticity. The kink mode is not perturbed by E and depends only on q_s , as seen in the Solovév study. For $q_0 = 1.1$ comparison with Figure 5.1 shows that ballooning modes are affected by the elongation of the plasma cross section. The stability limit in q_s , $q_s = 4.2$, is higher than $q_s = 3.8$ obtained for $E = 1$. The maximum $\bar{\beta}$ achieved is 2.1%. For an elongation up to 2, the gain in $\bar{\beta}$ is proportional to E , instead of E^2 as obtained in a simple flat current model (Chapter III, 3.2). The problem of an optimum in E remains open, but the trends obtained show its existence. The three curves show different structures. For $q_0 = 1.1$ the kink limit is smaller than the ballooning limit. For $q_0 = 1.3$ the two limits coincide and for $q_0 = 1.4$ the kink limit is active. We see the resonance of the curve around $q_s = 3$, characteristic of a kink behaviour.

In conclusion, as long as E is less than 2, elongating the plasma cross-section is a very efficient way to increase its $\bar{\beta}$.

5. Optimization of $\bar{\beta}$

Sections 3) and 4) have shown the existence of an optimum for $\bar{\beta}$ as a function of q_0 , due to the competition between the ballooning and kink limits. Moreover, the different behaviour of these frontiers with β_p and E make the existence of an optimum as function of β_p and E possible.

We have represented in Figure 5.14 the optimized average beta value $\bar{\beta}$, determined by MHD stability, for different values of β_p (0.5, 1, 2) and E (1, 2). Optimization is performed with respect to the current profile parameter q_s/q_0 .

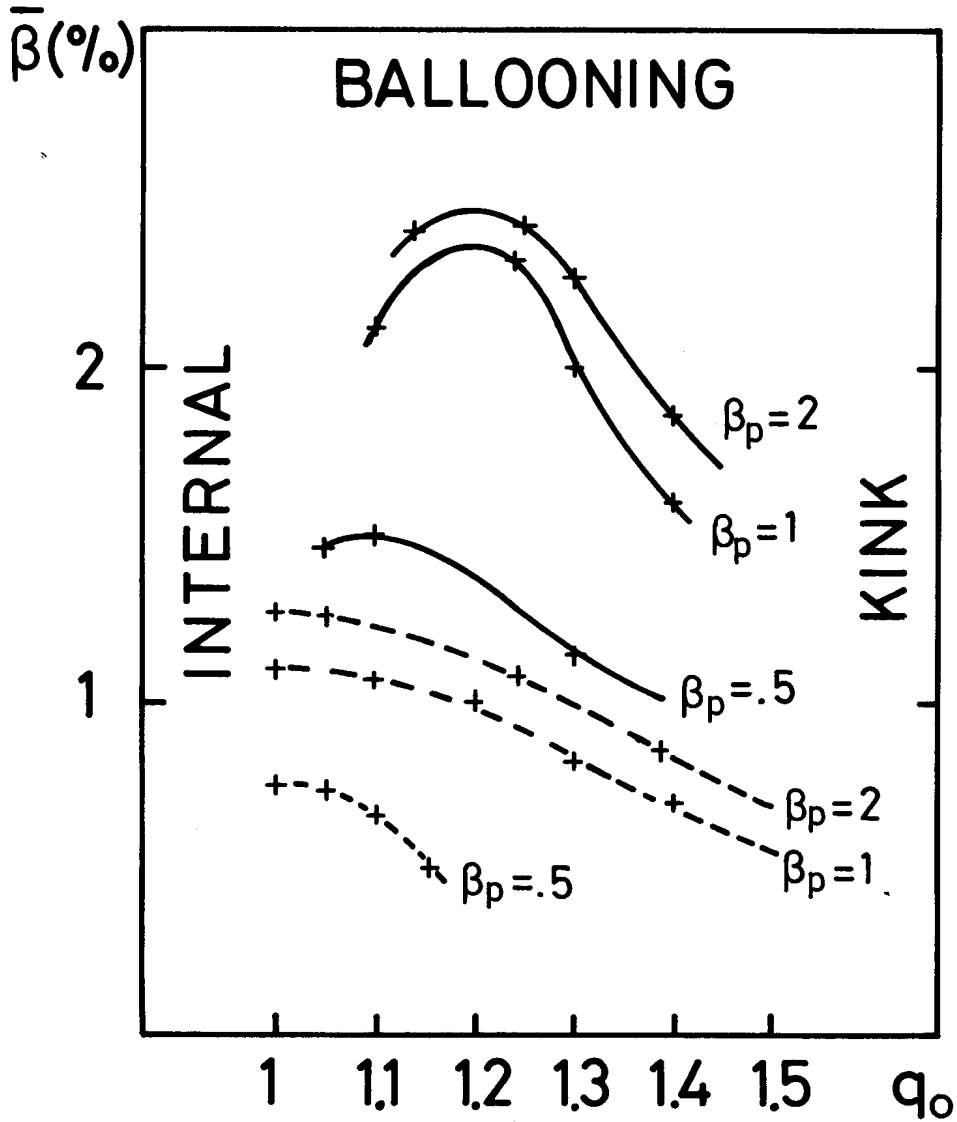


Figure 5.14

Representation of the optimized average beta value $\bar{\beta}$ versus q_0 for different values of β_p and E . $R/a = 3$. $E = 1$ (-----). $E = 2$ (———);

We see first that the $(1/q_0)^2$ dependence of $\bar{\beta}$ at large q_0 is stopped by the appearance of the ballooning modes. The optimum in q_0 lies around $q_0 = 1$ for $E = 1$ and shifts with the elongation E . In our range of parameters the dependence of $\bar{\beta}$ with E is roughly linear. The relation between $\bar{\beta}$ and β_p is more complicated. The function is linear for small β_p ($\beta_p < 1$), and saturates at high β_p ($\beta_p > 1$). These results show the limitation of the achievement of high β_p . Nevertheless, cold gas injection and supplementary heating are necessary to push a device

to its maximum $\bar{\beta}$ value. The value of β_p reached in a pure ohmically heated Tokamak ($\beta_p \approx 0.7$) gives a $\bar{\beta}$ less than the maximum value possible in a given geometry. We see that in a circular case this value lies around 1.5% and for an elongated D-shape ($E = 2$) 3%.

The study presented refers to Maxwellian current profiles, an optimization with other functional forms is necessary to obtain a whole view of the MHD stability of peaked current equilibria.

High $\bar{\beta}$ achievement is a subtle play between peaking, shaping and poloidal beta. The geometric parameters have a determining influence.

VI CONCLUSION

A finite "hybrid element" scheme has been used to generate a general purpose 2-D toroidal ideal MHD stability code : "ERATO". This method is easy to implement and well suited to treat numerically determined equilibria {10,11}.

The first application concerns the analytically tractable Solovév equilibrium {12}. A device with a small aspect ratio of 3 has been chosen. Non-localized modes couple different singular surfaces, which leads to a stabilization of the displacement. The toroidal coupling can also act between an external kink and an internal mode {47}. Strong kink instabilities destroy the plasma discharge, in contrast to experimental results.

The effect of peaking the current distribution in a small aspect ratio Tokamak is investigated. The safety factor on axis q_0 is kept fixed, its value at the surface q_s being progressively increased. Above a minimum level of q_s/q_0 , the kink instability does not occur. At large q_0 the kink limit is the stability limit. For q_0 in the vicinity of 1, another type of mode, induced by the toroidal coupling, determines the stability frontier.

The negative contribution to the potential energy comes from the plasma region lying between the $q=1$ and $q=2$ surfaces. As they correspond to q_0 greater than the Mercier limit these displacements are called "ballooning modes". In contrast to other calculations {48}, they correspond to small n and m numbers. For $q_0 < 1$, internal modes become unstable.

We have obtained the optimal $\bar{\beta}$, dictated by MHD stability considerations, versus q_0 , for different values of β_p and elongation of the plasma cross section E . Up to an elongation of 2, $\bar{\beta}$ varies proportionally with E . This is not the case for the β_p dependence where a saturation occurs for $\beta_p > 1$.

The work presented here does not complete the study of linear MHD stability in axisymmetric devices. An analysis of field profiles obtained by a transport code is necessary in order to be sure that our pessimistic results ($\bar{\beta} \sim 3\%$) are not linked to the Gaussian shape. A simple analytical model which computes the toroidal coupling between two singular layers is an important point to support our numerical results. It is also essential to remember that one can tolerate linear instabilities which are removed by a minor change in the configuration or whose non linear consequences are benign. A full understanding of the ideal MHD stability of Tokamaks requires non linear theory as well. Moreover, the influence of finite resistivity on the linear and non linear development of MHD instability must be investigated, in particular the island formation and evolution in presence of toroidal coupling. The MHD behaviour of a Tokamak is still an open field.

The theoretical predictions presented in this work have not yet been tested in present and short range projected Tokamaks; nevertheless they can strongly affect the efficiency of a Test Fusion Reactor. An experimental Tokamak with a variable elongation and an auxiliary heating source, which can push β_p up to 6, is an important step towards the achievement of a thermonuclear reactor.

ACKNOWLEDGEMENTS

The author is gratefully indebted to Professor F. Troyon and Dr. R. Gruber for their efficient collaboration and support throughout the whole work. Dr. L.C. Bernard joined our group and contributed significantly to the vacuum calculations. I would like to thank Dr. R.A. Dory, Dr. J.M. Greene, and Dr. D. Nelson for stimulating discussions as well as Professor E.S. Weibel, who made it possible for me to obtain a PhD grade in his institute.

I am gratefully indebted to Dr. J. Johnson for reading and commenting on this text.

Miss B. Schwab has typewritten the text and Messrs. P. Gorgerat and J.M. Mayor have drawn the figures; for this I am very grateful.

I would also like to mention the programming support of Messrs. R. Schreiber and T. Nguyen. I thank the staff of the Computer Center, especially the operators, who have allocated me all the computer power during numerous evenings and week-ends.

REFERENCES

- {1} C. Mercier, Nucl.Fusion 1 (1960), 47
- {2} J.M. Greene, J.L. Johnson, Phys.Fluids 5 (1962), 510
- {3} V.D. Shafranov, Zh.Tekh.Fiz. 40 (1970), 241
{Sov.Phys.-Tech.Phys. 15 (1970), 175}

E.A. Frieman, J.M. Greene, J.L. Johnson, K.E. Weimer,
Phys.Fluids 16 (1973), 1108
- {4} J. Wesson, VIIth Europ.Conf. on Contr. Fusion and Plasma Physics,
Vol 2, p. 102
- {5} K. Appert, D. Berger, R. Gruber, J. Rappaz
Journal of Computational Physics 18 (1975), 284

K. Appert, D. Berger, R. Gruber, F. Troyon, K.V. Roberts
Computer Phys. Commun. 10 (1975), 11
- {6} M.S. Chance, J.M. Greene, R.C. Grimm, J.L. Johnson
Nuclear Fusion 17 (1977), 65
- {7} D. Borel, K. Appert, D. Berger, R. Gruber, F. Troyon
ZAMP 26 (1975), 656
- {8} R.C. Grimm, J.M. Greene, J.L. Johnson, in 'Methods in Computational
Physics', Vol. 16, Academic Press, New York 1976, 253
- {9} M.S. Chance et al. (PPL), W. Kerner (IPP), D. Berger et al. (CRPP)
to be published in J.Comp.Phys.

- {10} R. Gruber, Journal of Comp.Physics (1977), to appear
- {11} D. Berger, R. Gruber, F. Troyon, 2nd Europ.Conf.on Computational Physics (1976), C3
- {12} L.S. Solovév, Zh.Eksp.Teor.Fiz. 53 (1967), 626
Sov.Phys.-JETP 26 (1968), 400
- {13} W. Kerner, J. Steuerwald, Comp.Phys.Comm. 9 (1975), 337
- {14} G. Laval, Phys.Rev.Letters 34 (1974), 1316
- {15} R.A. Dory, D.B. Nelson, Y.-K. M Peng (ORNL), D. Berger,
L.C. Bernard, R. Gruber, F. Troyon (CRPP), VIIIth Europ.Conf.
on Contr.Fusion and Plasma Physics (Prague, 1977)
- {16} D. Berger, L.C. Bernard, R. Gruber, F. Troyon, VIIIth European
Conf. on Contr. Fusion and Plasma Physics (Prague, 1977)
- {17} E.S. Weibel, Am.Phys. 36, No. 12 (1968)
- {18} C. Mercier 'Lectures in Plasma Physics'
EUR 5127e (1974) Commission of the European Communities
- {19} I.B. Bernstein, E.A. Frieman, M.D. Kruskal, R.M. Kulsrud,
Proc.Roy.Soc. (London) A244 (1958), 17
- {20} G. Schmidt, 'Physics of High Temperature Plasmas',
Academic Press, N.Y. (1966)
- {21} D. Berger, R. Gruber, F. Troyon, Comp.Phys.Comm. 11
(1976), 313

- {22} R. Gruber, Internal CRPP report
- {23} J.P. Freidberg, W. Grossman, Phys.Fluids 18 (1975), 1494
- {24} L.C. Bernard, D. Berger, R. Gruber, F. Troyon, ZAMP 28 (1977) 353
- {25} R. Lüst, E. Martensen, Z.Naturforschung 15a (1960), 706
- {26} E. Rebhan, Nucl.Fusion 15 (1975), 277
- {27} J.M. Greene, LRP 114/76 (CRPP)
- {28} Y.-K. M. Peng, R.A. Dory, D.G. Nelson, R.O. Sayer, ORNL/TM-5267 (1976)
- {29} J.D. Callen, R.A. Dory, Phys.Fluids 15 (1972), 1523
- {30} R. Gajewski, Phys.Fluids 15 (1972), 70
- {31} J.E.T. Project Comm.Europ.Comm. EUR JET R5 (1975)
- {32} Workshop on MHD Stability at the 7th Europ Conf. on Contr. Fusion and Plasma Phys., Lausanne (1975)
- {33} K.V. Roberts, Comp.Phys.Comm. 7 (1974), 237
- {34} R. Gruber, 2nd Europ.Conf. on Computational Physics (1976), F2
- {35} E. Rebhan, A. Salat, Nucl. Fusion 17 (1977), 2
- {36} M. Okabayashi, G. Sheffield, Nucl.Fusion 14 (1974), 263

- {37} W. Kerner, Nucl.Fusion 16 (1976), 643

- {38} D. Berger, L.C. Bernard, R. Gruber, F. Troyon
6th IAEA-CN, Berchtesgaden, 1976

- {39} M.N. Bussac, R. Pellat, D. Edery, J.L. Soulé
Physical Review Letters 35 (1975), 1638

- {40} R.L. Dewar, R.C. Grimm, J.L. Johnson, E.A. Frieman, J.M. Greene,
P.H. Rutherford, Phys.Fluids 17 (1974), 930

- {41} T.F.R. Group, 7th Europ. Conf. on Contr. Fusion and Plasma
Physics, Lausanne (1975), Vol. 2, p. 1

- {42} J.F. Clarke, Bull.Am.Phys.Soc. 20 (1975), 1228

- {43} R.A. Dory, Y-K. M. Peng, Nuclear Fusion 17 (1977), 21

- {44} R.G. Bateman, Y-K. M. Peng, Phys.Rev.Letters 38 (1977), 829

- {45} J.L. Soulé, Private communication

- {46} E. Freeman et al., 6th IAEA-CN 35, Berchtesgaden (1976)

- {47} M.N. Bussac, D. Edery, R. Pellat, J.L. Soulé, 6th IAEA-CN,
Berchtesgaden (1976)

- {48} A.M. Todd, M.S. Chance, J.M. Greene, R.C. Grimm, J.L. Johnson,
J. Manickam , Phys.Rev.Letters 38 (1977), 826

APPENDIX

Table of Symbols

\underline{A}	vector potential
$\{A_{ij}\}$	plasma potential energy matrix
\underline{B}	total magnetic field
\underline{B}_v	vacuum magnetic field
B_p	poloidal magnetic field
$\bar{\beta}$	average beta = $(\int p d\Omega) / (\frac{1}{2} \int \underline{B}^2 d\Omega)$
β_p	poloidal beta = $(\int p d\Omega) / (\frac{1}{2} \int B_p^2 d\Omega)$
Γ	growth rate
γ	ratio of specific heat
d	triangularization factor (Solovév equilibrium)
$d\Omega$	volume element
$d\sigma$	surface element
$d\ell$	line element
δ	perturbation
∂	partial derivative
$\partial\Omega$	plasma surface
∂W	wall

E	elongation of plasma cross section
$e_{i+\frac{1}{2}j}$	basis function for derivative Ψ with respect to point $(\Psi_{i+\frac{1}{2}}, \chi_j)$
e_i	basis function for single variable quantity at point χ_i
F	operator $\frac{1}{q} \frac{\partial}{\partial \chi} + n$
$f_{i+\frac{1}{2} j+\frac{1}{2}}$	basis function for function value at point $(\Psi_{i+\frac{1}{2}}, \chi_{j+\frac{1}{2}})$
ϕ	vacuum scalar potential
ϕ^P	vacuum scalar potential at plasma surface
ϕ^W	vacuum scalar potential at the wall
φ	toroidal direction angle
$G(\underline{x}, \underline{x}')$	$1 / \underline{x}-\underline{x}' $
$G_F(x, x')$	Green's function projected on the toroidal direction φ .
$\{G_{ij}\}^F$	Green's matrix
$g_{ij+\frac{1}{2}}$	basis function for derivative with respect to point $(\Psi_i, \chi_{i+\frac{1}{2}})$
i	Ψ mesh counter
\underline{j}	total current density
j_φ	toroidal current density
J	Jacobian

j	χ mesh counter
K	destabilizing factor
K_n	elliptic integral (vacuum treatment)
$\{K_{ij}\}$	kinetic energy matrix
χ	poloidal coordinate
χ_\perp	poloidal coordinate (orthogonal system)
\mathcal{L}	Lagrangian
Λ	ratio of shell to plasma radius
m	dominant poloidal Fourier component
\underline{n}	unity vector normal to flux surface
ν	peaking parameter
N_ψ	number of ψ intervals
N_χ	number of χ intervals
n	toroidal wave number
p	total pressure
p'	derivative of p with regard to ψ
ψ	poloidal magnetic flux
ψ_s	ψ at plasma surface
ψ_0	normalization factor for ψ
\underline{Q}	perturbed magnetic field $\underline{Q} = \underline{\nabla} \times (\underline{\xi} \times \underline{B})$

q	safety factor
q_0	safety factor at axis
q_s	safety factor at the plasma surface
q_ℓ	upper limit of Mercier's violated region
R_0	position of magnetic axis
R/a	aspect ratio
r	distance from the main axis of the torus
ρ	total mass density
ρ_0	normalization factor for denisty
ρ_p	polar distance of a plasma surface's point
ρ_w	polar distance of a wall point
s	$\sqrt{\Psi/\Psi_s}$
T/r	toroidal equilibrium magnetic field
t	time
\mathcal{V}	non orthogonal factor = $\frac{\partial X}{\partial \Psi} \Big _n$
θ	polar angle in poloidal plane
θ_w	polar angle of a wall point
V	component of ξ $V = qvrB_p \xi_\psi - \xi_\varphi / r - T\xi_i / r^2 B_p$
V^R	up-down symmetric component
V^I	up-down anti-symmetric component

$V^{(1)}$	V component for χ derivative
$V^{(2)}$	V component for function value
\underline{v}	fluid velocity
W	vacuum region
$\{W_{ij}\}$	vacuum energy matrix
W_V	perturbed vacuum energy
Ω	plasma region
ω	eigenfrequency
ω_T^2	normalization factor for $\omega^2 = \frac{T^2(\Psi_0)}{R_0^4 \rho}$
ω_A^2	ω_T^2/q_0^2
$\omega^2 K_C$	perturbed kinetic energy
X	component of $\underline{\xi}$, $X = rB_p \xi_\psi$
X^R	up-down anti-symmetric component
X^I	up-down symmetric component
$X^{(1)}$	X component for χ derivative
$X^{(2)}$	X component for function value
$X^{(3)}$	X component for ψ derivative
$\underline{\xi}$	displacement vector
ξ_ψ	normal displacement component
ξ_{χ_\perp}	poloidal displacement component

ξ	toroidal displacement component
Y	component of $\underline{\xi}$, $Y = \frac{\xi_{\varphi}}{r}$
Y^R	up-down symmetric component
Y^I	up-down anti-symmetric component
$Y^{(1)}$	Y component for χ derivative
$Y^{(2)}$	Y component for function value
z	distance along the main axis of the torus

CURRICULUM VITAE

Born on May 26th, 1950, in Lausanne, I obtained a "Maturité Scientifique" in 1968. At this time, I registered with the Swiss Federal Institute of Technology (EPF-L), where I obtained the grade of Engineering Physicist in 1973. The topics of the final examination concerned a study on "Laser Diffusion by Liquid Crystals" (Experimental Physics, Prof. R. Mercier). At the same time, I received a diploma in mathematical sciences at the University of Lausanne. Since 1973, I have been engaged as a research assistant at the Swiss Institute for Plasma Physics (CRPP).